Hydrolysis of Ti-containing alkoxides: Preparation, stabilization and characterization of TiO_2 nanostructures

Dissertation
zur Erlangung des Doktorgrades
des Fachbereichs Mathematik und Naturwissenschaften
Fachgruppe Physik

der Bergischen Universität Wuppertal

vorgelegt von
Dipl. Phys. Stefanie Pfleiderer
aus Düsseldorf

Die Dissertation kann wie folgt zitiert werden:

urn:nbn:de:hbz:468-20150519-114621-2
[http://nbn-resolving.de/urn/resolver.pl?urn=urn%3Anbn%3Ade%3Ahbz%3A468-20150519-114621-2]

Contents

Abstract

Titanium dioxide (TiO_2, titania) nanoparticles got great attention during the last decades due to a great field of possible applications. Under this directive, there had been intensive research in the past to learn about the factors which influence the effectiveness in these applications. In addition, there is a necessity to find preparation routes for optimal-structured nanoparticles. A possibility for the synthesis of nanostructures with tailored characteristics is the sol-gel process. The materials structure can be influenced by the chemical reaction environment (pH of reaction solution, the type of used electrolyte, dilution, water concentration, ect.).

In this work, a combination of different methods using x-rays is used to investigate the structure of sol-gel derived TiO_2 and TiO_2-ZrO_2 nanostructured powders. The particle size of the crystallites is determined with x-ray diffraction (XRD), which also allows the determination of the type of crystalline phases. Unfortunately, XRD is not sensitive to amorphous fractions of the powders or small clusters of only a few nanometers size. X-ray absorption fine structure (XAFS) is sensitive to the amorphous as well as crystalline sample fractions and allows qualitative determination of the structure of the first small crystallites build in the powders during the synthesis as well as the structure of the samples after the crystallization process. Additionally, x-ray photoelectron spectroscopy (XPS) is applied to investigate the chemical composition of the prepared structures with respect to contaminations from additives in the synthesis step.

The following investigations will focus on the preparation of titania materials suitable for applications in photocatalysis. In this context, it would be interesting to be able to stabilize the size and the crystalline phase of the nanostructures during the annealing process. An already common way to do this is the preparation of TiO_2 with additional oxides. In this thesis, TiO_2-ZrO_2 materials are prepared, which are good photocatalysts. If only small amounts of zirconia (ZrO_2) are included in these materials, the titania fractions will crystallize selectively, while zirconia fractions will stay amorphous.

The first step of this work will be the preparation of samples with the same reaction environment but different TiO_2:ZrO_2 ratios. Measurements of pure titania and zirconia samples will be presented for comparison with the mixed oxide powders. Limit TiO_2:ZrO_2 ratios will be determined for the crystallization of the titania fractions as well as for the stabilization of crystallite size and phase. With a ratio determined to be suitable for the preparation of optimal structures for photocatalytic materials, different chemical reaction environments are tested with respect to the nanocrystalline structure of the resulting powders. Pure titania powders will also be prepared and investigated in the same reaction environments. Thus, the impact of the reaction conditions can be compared between pure titania, which is investigated in many publications, and the mixed oxides, which is less intensively studied up to now.

Next to the bulk structure investigations with XRD and XANES, information about agglomerate structures can be collected by grazing-incidence small angle x-ray scattering (GISAXS). Photocatalytic tests with some of the samples were made by investigations of the decomposition of methylene blue under ultraviolet irradiation.

1 Introduction

Titanium dioxide based photocatalysts are a very interesting class of catalytic materials. They have a comparably high catalytic activity and are able to decompose organic contaminants in water and air. Thus, they provide a possibility to solve environmental problems. Next to this important field, they are also applicable, for example, in cancer treatment. Other possible uses of nanostructured TiO_2 materials are coatings for self-cleaning surfaces and applications in the field of energy storage like the splitting of water in oxygen and hydrogen and the use as electrode materials for lithium-ion batteries.

This work focuses on TiO_2 based nanomaterials. There are some desired characteristics which lead to materials with high efficiency, especially in catalysis. Namely, these are a large surface area, a small particle size, a high degree of crystallinity and the anatase crystalline phase instead of brookite or rutile, which are two other possible polymorphs of TiO_2 under ambient conditions. Next to these factors, a narrow particle size distribution is also eligible. From this point it is obvious that a synthesis method for the material has to provide the possibility to tailor these material characteristics. A method which is suitable for the nanomaterial synthesis is the sol-gel process. It usually contains the hydrolysis and condensation of metal alkoxide precursors under certain reaction conditions. After a short time period of a few fractions of seconds, white precipitates are observable in sol-gel processes of unmodified transition metal oxides. The reaction products of these processes are amorphous in most cases. To prepare crystalline particles, a further treatment of the materials is necessary. Crystallization can occur after annealing at temperatures of a few hundred degrees or after hydrothermal treatment. Also after storage of the amorphous powders in ambient air at room temperature, crystallization is observable. The structure of materials resulting from these crystallization processes is dependent on the chemical reaction environment of the powder synthesis. To prepare materials with the desired characteristics and thus a high photocatalytic activity, it is important to know and understand the reaction parameters leading to a certain crystalline structure.

In the synthesis steps, there are significant problems. The amorphous powder precursors for the crystallization processes, which are derived from the sol-gel process usually need heat treatments at high annealing temperatures or long annealing times to show high crystallinity. During these treatments, the crystallites in the powders start growing, decreasing the surface area by coarsening. Also crystalline phase transitions become more possible if the crystallite size increases, especially that one from the anatase to the rutile phase in case of TiO_2. It would thus be eligible to be able to stabilize the crystallites during the heat treatment process. Such a possibility is indeed known, it was proven, for example, in a study by Elder et al. [1] that the addition of zirconium alkoxides to the titanium alkoxides in the reaction step leads to stabilized crystallization of anatase particles in an amorphous zirconia matrix during hydrothermal treatment and calcination. Also other oxides can be added to stabilize anatase TiO_2 crystallites during the heat treatment. Next to the stabilizing effect, it can be found in the literature that TiO_2-ZrO_2 catalysts have an enhanced photocatalytic activity. In contrast to pure tita-

nia synthesis, no systematic study of the influence of the chemical reaction environment in the synthesis step on the resulting materials structure, comparable to that one of Rossmanith et al. [2] for example, is available for titania-zirconia composite materials up to now.

The presented work deals with the preparation of TiO_2-ZrO_2 composite oxides and pure TiO_2 nanostructured materials. The preparation is performed in different reaction environments, including 1 M hydrochloric acid (HCl), 1 M sodium hydroxide (NaOH) and 1 M potassium hydroxide (KOH), addition of propanol alcohol to the reaction environment, the addition of different amounts of water in the hydrolysis step and the application of different reaction temperatures.

To investigate the crystalline structure, different x-ray characterization methods are combined to get as much information on the relevant material properties as possible. X-ray absorption spectroscopy (XAS) is a very powerful tool for the investigation of nanostructures, due to its sensitivity to the coordination environment, which is a very important factor especially at the large surfaces of the structures. XAS is also able to provide information about the amorphous contributions of the samples, which are difficult to investigate with other characterization methods. Linear combination fits of the x-ray absorption near edge structure (XANES) region can be made with reference spectra resulting in quantitative information about the concentrations of crystalline and amorphous phases. By a qualitative determination of the cluster structures built in the reaction step with the aid of the XANES structures, it is possible to investigate their influence on the crystallization processes. The average crystallite sizes can be determined from the peak broadening of the diffraction patterns measured in x-ray diffraction (XRD). Next to the crystallite size investigations, XRD allows the quantitative determination of the crystalline phases included in a sample, but does not allow detailed investigations of the amorphous sample fractions. In contrast to x-ray absorption spectroscopy, XRD measurements can be performed with laboratory x-ray tubes, but also at synchrotron radiation sources. To get information about the particle sizes of agglomerated structures and their distribution, grazing-incidence small angle x-ray scattering (GISAXS) can be applied. Another important factor for materials prepared in sol-gel processes is the chemical composition of the samples. Additives from the sol-gel synthesis like electrolytes can contaminate the reaction products. For a quantitative determination of the included chemical species, x-ray photoelectron spectroscopy (XPS) is applied in this work.

In nanoscience, microscopic techniques are a common tool for structure determinations. In this work, additional information about the structure of the samples is derived from scanning electron microscopy (SEM).

In the presented work, the above stated characterization methods are combined in this way for the first time for the investigation of titania based nanomaterials. In this way, the missing systematic study of the influence of the reaction path on the preparation of TiO_2:ZrO_2 nanostructured materials and pure titania materials is delivered.

As a test application for the prepared nanomaterials, methylene blue decomposition over the nanopowders was investigated with optical absorption spectroscopy.

2 Theoretical fundamentals

In the following section, a brief introduction to the specifics of nanostructured materials will be given first. This part is mainly written according to 'Concepts of nanochemistry' by Cademartiri and Ozin [3]. Possible applications of nano-TiO_2 materials are presented next in dependence on their structure to motivate the necessity for detailed structural investigations. The preparation method itself will be described in section 2.2, where an overview of sol-gel chemistry is given. This process usually leads to amorphous powders in the case of titania synthesis, thus crystallization has to be achieved by a further treatment. In section 2.3, the crystallization mechanisms of TiO_2 nanocrystallites will be explained in detail. The characterization of the resulting structures is performed by x-ray absorption spectroscopy (XAS), x-ray diffraction (XRD), x-ray photoelectron spectroscopy (XPS), grazing-incidence small angle x-ray scattering (GISAXS) and scanning electron microscopy (SEM). A short introduction to synchrotron radiation is presented in section 2.6.

2.1 General properties of nanostructures

The prefix 'nano-' is usually used for structures with size scales between 1 and 100 nm (1 nm=10^{-9} m), although this definition is criticized by some authors [3]. The size dimensions nanoscience deals with are already present in nature and different branches of physics, chemistry and biology. In nature, bacteria, viruses, cells and other structures usually have sizes in the nanoscale. Especially in chemistry, nanoscale structures are present in macromolecules, polymers or colloidal particles. This leads to the high degree of multidisciplinarity in today's nanoscience. Nanostructured materials are interesting because they exhibit properties which are different from materials with structures in the macro range. They have properties tunable by the materials size, morphology and crystalline structure. A well known example of the size dependence of optical characteristics is the color of thin gold films. The size of nanostructures is the first very critical parameter influencing the material properties.

Another property of the materials structure, which is directly related to the structure size, is the particle surface area. To describe the surface area in the nanoregime, a value called specific surface area is introduced, which means the surface area per volume, A_{spec}=A/V. It is obvious that with decreasing structure size, the specific surface area increases. The surface atoms cannot fully coordinate like in the material volume, where they are surrounded by binding partners. This is very important for the chemistry of nanostructures, because incompletely coordinated atoms at the surface are anxious to complete their coordination shell and are thus more reactive than atoms with saturated coordination shells. The shape of the particles is important because the corners and edges also are occupied with atoms with missing binding partners and are important reaction sites.

Grain-boundaries occur between small nanocrystallites, especially if they are agglomerated to larger structures. These grain-boundaries have a strong influence on the dif-

fusion characteristics of the material and also on crystallization processes, as will be discussed in the next section.

A very important property of nanomaterials is their energy level structure. With respect to the atomic model of Bohr, atoms have discrete energy levels. Each energy level belongs to the energy differences between specific electron orbitals, on which the electrons surround the atomic nucleus. In molecules, there are more degrees of freedom due to possible movements (like rotations) of atoms in a chemical bond. Thus, there are more possible energy levels. If structures become even larger in solid states, there are more energy levels very close to each other, building energy bands. In nanostructures, there are more and closer energy levels than in a molecule, but less than in a macroscopic solid if the particle size is small enough. There is also a blue-shift of absorption lines with decreasing particle size [4]. Thus, also electrical properties of nanomaterials are strongly dependent on the particle sizes at small size scales. This point will not be discussed in detail in this work. A detailed description can be found in [5].

Historically, the beginning of nanoscience was when people had the knowledge and especially the experimental tools to investigate the nanosized materials structure. For todays large bandwidth of applications, it is necessary to be able to tune the material characteristics not randomly, but with knowledge of the preparation possibilities and the dependencies of characteristics on the process conditions. In this context, it is important to have or find possibilities for the materials production as well for their characterization.

2.2 Applications of TiO_2 and their dependence on the materials structure

2.2.1 Titania nanostructures for heterogeneous photocatalysis

The treatment of wastewater and exhaust fumes in environmental science is and will be of great importance. Catalysis is a very important tool in this context. If the electron-hole pairs created in a semiconducting catalyst due to the absorption of UV radiation are used for the chemical reaction, the method is called photocatalysis [6, 7]. A good photocatalyst should have the following characteristics: high photoactivity, high optical activity in the visible and ultraviolet radiation range, stability in a biochemical environment, high photostability and low production costs [8]. For the generation of electron-hole pairs, it is important to use semiconducting materials. To find the best material for the photocatalysis of a certain chemical reaction, it must also be chosen with respect to the used reactants of the reaction [7]. If the reactants absorb the photons with the energy of the catalysts band gap, another catalyst with another band gap energy has to be chosen.

In heterogeneous catalysis, the catalyst and the reactants are of different aggregate state. Usually, the catalyst is a solid and the reactants are liquids or gases. In the case of photocatalysis, a solid state semiconductor is irradiated by radiation fitting to the materials band gap. Due to the absorption of the radiation, electron-hole pairs are created. In case of titania catalysts, this step is described by [9]

$$TiO_2 \xrightarrow{h\nu} e^-_{cb}(TiO_2) + h^+_{vb}(TiO_2), \tag{2.1}$$

where hν is the energy of the impinging photon, e^-_{cb} the generated electron from the conduction band and h^+_{vb} the hole created together with the electron from the valence band.

Titania is a semiconductor with a band-gap energy of 3.2 eV in the anatase polymorph and 3.0 eV in the rutile polymorph [10]. It is photoresistant, commercially available, cheap and has a good catalytic activity [11]. Compared to other pure metal oxides, titania is one of those with the highest catalytic activity [12]. A disadvantage of titania is that it has comparably high electron-hole recombination rates [13]. The generated electron-hole pairs (compare Eq. 2.1) can migrate to the particle surface and react with adsorbed species. Redox reactions will take place, where the electron will reduce and holes will oxidize the reactants. It is also possible that the electrons and holes first react with surface species, especially with surface OH-groups. At the surface, there will be a quasi-bimolecular reaction between the adsorbed molecule and the photogenerated charges [14]. The reactions which are usually occurring are as follows [15]

$$\mathrm{TiO_2}+\mathrm{h}\nu \rightarrow \mathrm{TiO_2^*}(\mathrm{e_{cb}^-}+\mathrm{h_{vb}^+})$$

$$\mathrm{TiO_2}(\mathrm{e_{cb}^-}+\mathrm{h_{vb}^+})\rightarrow \mathrm{TiO_2}+\text{ heat}$$

$$\mathrm{H_2O}_{ads} \rightarrow \mathrm{OH}_{ads}^- + \mathrm{H}_{ads}^+$$

$$\mathrm{h_{vb}^+} + \mathrm{OH}_{ads}^- \rightarrow \mathrm{OH}^{\cdot}$$

$$\mathrm{e_{cb}^-}+\mathrm{O_2} \rightarrow \mathrm{O_2^{\cdot -}}.$$

In these equations, 'ads' in the subscript denotes adsorbed species and a dot in the superscript denotes a radical species, a minus or a plus an ionized species and a star an excited species.

Examples of oxidation and reduction reactions on titania surfaces are the decomposition of organic compounds (oxidation) and the removal of heavy metal ions from wastewaters (reduction) [16]. Next to these catalytic applications, catalysis of condensation, polymerization, geometrical and valence isomerization and substitution reactions is possible with titania catalysts [17].

From the above stated mechanisms, it is clear that the recombination of electron-hole pairs must be suppressed in a highly efficient catalyst. The recombination rate can for example be reduced by a small number of surface defects, which work as charge traps. If the number of traps (number of defect sites) becomes too large, the trapped charges are close to each other and thus recombination again becomes more possible [13].

An important environmental application of titania photocatalysis is the treatment of wastewaters. In this context, decomposition of methylene blue from aqueous solutions will be investigated in this work. For organic pollutants in water, the general decomposition reaction is given by [7]

$$organic\ pollutant + O_2 \xrightarrow[ultra\ \ bandgap\ light]{sc} CO_2 + H_2O + mineral\ acids, \qquad (2.2)$$

where 'sc' is an abbreviation for semiconductor.

It is obvious that the surface of the nanostructures should be as large as possible in a catalyst to allow as much reactant to be absorbed on its surface as possible. A large surface area also allows a large area to be irradiated with light and thus a high amount of photons to be absorbed. For nanostructures, a quantity called specific surface is usually introduced as explained in section 2.1. To achieve a large specific surface area, the particle size should be as small as possible. Another way is to prepare porous materials.

At the surface, there are 5-fold coordinated titanium atoms and 2-fold coordinated oxygen atoms, which are more reactive than their 6-fold, respectively 3-fold counterparts in the TiO_2 bulk [18]. Nevertheless, it is not helpful to decrease the particles to sizes smaller than about 10 nm in order to increase the surface area. Zhang et al. found that particle sizes between 10 and 15 nm should be most suitable for TiO_2 photocatalysts [19]. If the particles are larger, the recombination of electron-hole pairs in their volume will increase and lower the catalytic activity of the material. For smaller particle sizes, the amount of electrons and holes lost by surface recombinations will increase. The migration time of electrons and holes from the particle volume to the surface is also a function of the particle size. Serpone et al. reported migration times of $\sim$0.05 ps for particles with diameters d of d=2.1 nm, $\sim$1.8 ps for d=13.3 nm and $\sim$9.9 ps for d=26.7 nm [4]. The longer the migration time, the larger the possibility for undesired electron-hole recombination, and thus the lower the catalytic activity.

Not only the surface, but also the surface structure is very important for catalytic applications of TiO_2. The surface structure can provide acid or base sites [20]. In this work, information about the surface to volume ratio of the particles is available from the Ti K-edge XANES pre-edge.

In different investigations, the anatase crystalline phase was found to have a higher catalytic activity than the other possible polymorphs, which are brookite, rutile and next to these crystalline phases the amorphous TiO_2. Although anatase TiO_2 is generally named as the polymorph with the highest catalytic activity, it should be mentioned that there are some known exceptions, for example the decomposition of H_2S, where the rutile phase seems to be the more suitable catalyst, or reactions like the oxidation of some organic compounds in the wastewater treatment, where a mixture of anatase and rutile leads to the best catalytic results [21]. Even the third TiO_2 polymorph brookite was found to be a potential catalyst if the particle size is between 11 and 15 nm [22]. The thermodynamic stability of different TiO_2 polymorphs is dependent on the particle size due to its dependence on the surface enthalpy of the particles, as was shown by Zhang and Banfield [23]. Anatase particles are stable for small particle sizes, below 11 nm. With increasing particle sizes, the rutile polymorph becomes more stable. Thus, a stabilization of the particle size is not only favorable for the catalytic activity by the particle size parameter, but also because of the corresponding stabilization of the anatase phase.

In the literature, it can often be found that it is required to have a high degree of crystallinity and the anatase phase instead of the other polymorphs of TiO_2. Kominami et al. [24] found that the crystallinity has a higher influence on the catalytic activity than the surface area. Indeed, the necessity to have a high crystallinity and the anatase polymorph leads to two different kinds of problems. If an amorphous material is provided from the chemical synthesis step as it is the case in sol-gel processes, a phase transformation to the anatase phase is required, which is usually done by a thermal treatment, see for example [25, 26]. To achieve a high degree of crystallinity, high annealing temperatures or prolonged annealing times are necessary. During the heat treatment process, anatase nuclei are formed and anatase crystallites start growing from these nuclei. With increasing particle size and coarsening of the anatase structures, the crystallinity increases, but the surface area is reduced. To avoid brookite and rutile to be formed in the material, phase transformations have to be suppressed, which can be achieved by e.g. the addition of other metal oxides, such as ZrO_2, which is used here to stabilize the particle size and thus also the anatase phase [1]. Other oxides used as additives to

titania, which can be found in the literature are SiO_2 [27], SnO_2, MoO_3, WO_3, In_2O_3 and Nb_2O_5 [6]. In the catalytic decomposition of formaldehyde, especially the titania catalysts with zirconia and silica addition showed enhanced activities [27]. The authors of [27] found that the specific activity (activity/surface area), was highest for the pure titania catalyst, but the surface area of the composites with zirconia and silica were so much higher that they had a higher total activity.

All the subjects mentioned above show that it is important to investigate the influence of the preparation conditions on the structure of the nanomaterials. Additionally, the preparation of TiO_2-ZrO_2 mixed oxides is a very important point, because it influences many of the desired characteristics of crystalline titania nanocatalysts in a positive way and leads to materials with high photocatalytic activities. The material characteristics of mixed oxides are not only a superposition of the characteristics of the single oxides due to strong interactions between the surfaces of the two oxides [28]. The higher catalytic activity of these mixed oxides should not be due to the formation of Ti-O-Zr in crystalline modifications, because it is known that zirconium titanate phases ($ZrTiO_4$) are catalytically less active than pure TiO_2 or pure ZrO_2 for example from a work of Navio et al. [12]. They wrote that the catalytic activities behave like $TiO_2 \gg ZrO_2 > ZrTiO_4$. The large difference between the photocatalytic activity of TiO_2 and $ZrTiO_4$ was explained by Navio et al. as a result of a large difference in the photoconductivity of the two materials. Under the same UV intensity, TiO_2 was able to build more electron-hole pairs than zirconium titanate [12], which means that more holes can react with surface species. Zirconia can also be used as a catalyst, for example for mild oxidation reactions [12].

In many chemical reactions, acids and bases like H_2SO_4, HF, HCl or $Ca(OH)_2$ are used as catalysts [29]. A problem of these catalysts is that they are environmentally toxic and that the disposal of these substances can be very expensive. TiO_2-ZrO_2 mixed oxide catalysts have acidic as well as alkaline sites on their surface, making them hopeful candidates to replace the above mentioned substances [29]. An increase in the surface acidity of the mixed oxides of titania and zirconia might be the reason for their higher catalytic activity [6]. Small amounts of zirconia are able to suppress the electron-hole recombination and in this way increase the catalytic activity [17].

Although many literature sources state that the catalytic activities of TiO_2-ZrO_2 mixed oxides are higher than those of pure titania, there are also some exceptions, where a decrease in the catalytic activity is stated, for example in a work investigating the decomposition of 2-chlorophenol [30]. A reason for the reduction of catalytic activity by zirconia addition may be the shielding of the titania catalyst from the UV radiation by the zirconia [13].

Shchukin and Caruso found that especially in the case of titania-zirconia mixed oxide samples, the history of catalyst preparation is of great importance for the catalytic activity [30].

Due to the high impact of the material structure on the catalytic activity, it is important to have possibilities to prepare materials with tailored characteristics and to examine the important structural parameters of the materials.

2.2.2 TiO_2 electrode materials in energy storage devices

Lithium ion batteries consist of cells with two metal plates for the abstraction of the current, anode, cathode, a separator to shield the anode from the cathode and a non-aqueous electrolyte. The electrodes can be made of porous transition metal oxides or graphite. In the charging process, the lithium, which is intercalated in the transition metal oxide leaves the electrode and travels to the graphite electrode, where it is intercalated into the graphite, to balance the charging from the external link between the electrodes. The small Li ions are able to pass the separator material. In the discharging process, the lithium ions travel from the graphite electrode to the transition metal and are intercalated there. Thus, both electrodes must be able to intercalate lithium ions reversibly [31].

If transition metal oxides should be used for electrode materials in Li-ion batteries, they should have the following characteristics: high insertion capacity for Li, high intercalation and de- intercalation rates, high volume energy density and low costs [32].

Also for the intercalation of Li into TiO_2, the anatase phase is more desirable in comparison with brookite or rutile, because anatase is able to incorporate more lithium than brookite or rutile [33]. This is explained by the structure of anatase, which is more open than the structures of the other two polymorphs [33]. Also in electrode applications, a high degree of crystallinity is helpful. Defects in amorphous or partially amorphous structures work as trapping sites for charge carriers and thus would reduce the conductance of the electrodes [34].

Wagemaker et al. [35] showed that the intercalation capacity of titania is strongly dependent on the particle size. The intercalation capacity decreased with increasing particle size.

2.2.3 Other applications

Titanium dioxide is also used in context with energy conversion. Grätzel et al. used nanocrystalline TiO_2 together with dye and electrolyte for the building of solar cells, the so called Grätzel cells [36]. In these cells, the photogenerated electron from the dye is transported into the semiconductor conduction band (dye sensitizes solar cell, DSSC). The electron-hole pairs are generated by photoelectric effect and the electron is then transported through the oxide. Due to the fact that the electron migrates in the semiconductor in the same manner as in the case of photocatalysts, it is also important here to suppress too much trapping. This leads to the same desired characteristics which are used in photocatalysis to achieve recombination suppression (small particle size, high degree of crystallinity, anatase phase [20]). To extend the light absorption to larger ranges, large anatase particles are mixed with smaller ones [36]. After the electron is injected to the semiconductor, the dye is regenerated by the electrolyte.

Another application of titania nanomaterials in energy conversion is closely related to the use of TiO_2 as a photocatalyst. Titania can be used for the dehydration of methanol to dimethylether (DME) [37]. DME should be used as an environmentally friendly and clean fuel. If it is burned, it produces a lower amount of nitrite oxides NO_x species, a lower number of carbon particles, produces less noise and nearly no fume with respect to common fuels [37]. Titania as well as zirconia catalysts could be used in this reaction, but both have the disadvantage that phase transitions and decrease of surface area might occur with respect to the reaction conditions. This is the reason why TiO_2-ZrO_2 materials might be a solution for this application [37].

In connection with the splitting of water into hydrogen and oxygen over TiO_2, energy storage devices based on H_2 also benefit from TiO_2 based nanomaterials. A very important point in the history of titania application was the splitting of water by Fujishima and Honda in 1972 [18]. The hydrogen extracted from this process can be used as a fuel. The splitting reaction is comparable to the decomposition of chemical compounds in photocatalysis. The water splitting is nothing but a catalyzed chemical reaction. Thus, the material requirements are the same as in catalysis [38].

For gas sensor applications, it is obvious that the surface of the used materials should be as large as possible. It was found that metal oxide materials are suitable for sensor applications, because they take effect very fast [39]. The stability of TiO_2 makes it useful for gas-sensor applications like as lambda probes [40].

Another important application of TiO_2 is the use as a pigment. About 400 different titania white pigments have been available on the world market in 2011 [41]. They differ in their properties and structure. The catalytic activity of the titania has to be as low as possible to avoid the decomposition of color compounds like organic solvents. For this reason, anatase is often not desired as a paint compound due to its high catalytic activity. Rutile has a high dielectric constant and a low catalytic activity, which makes it very desirable for the use as a pigment in colors [41].

Inorganic membranes are very interesting field in separation science, where metal oxides should replace organic membranes due to their higher stability. For the use of TiO_2 in separation science and applications, especially the pore sizes of the oxide membranes are of high importance. The membranes must be able to work under high temperatures. Thus, it is important that the characteristics of the membrane materials (particle size, crystalline phase, ect.) do not change in the duration of application. Additions of other oxides can help to constrain the crystallite size and phase of TiO_2 during heating processes.

In electronic applications, rutile is used due to its very high dielectric constant and high electronic resistivity [42, 43].

2.3 Sol-gel chemistry

The sol-gel process is known from colloid chemistry, which is a kind of progenitor of nanochemistry. From a 'nanoscientific' point of view, the sol-gel process is a bottom-up technique, which means that the nanostructures are built up from the atomic level to larger structures. The opposite is the top-down approach, which means that nanostructures are achieved by dividing larger structures until the nanoscale is reached. The fundamental aspects in the following section about sol-gel chemistry are written based on the book of Brinker and Scherrer [44].

In the sol-gel process, a precursor species, usually an organometallic compound or an alkoxide like in this work, is hydrolyzed to create a metal hydroxide compound, which turns to an oxide by polycondensation. A pioneer work was performed in the 1930s, when Geffcken found that alkoxides can be used to prepare thin oxide layers. Alkoxides itself were discovered in 1846 by Ebelmen, who prepared the first silicon alkoxide from a reaction of alcohol and $SiCl_4$. They are no organometallic compounds, as sometimes stated in the literature, because the organic ligands are not bound to the cation by a metal-carbon bond. The hydrolysis reaction of alkoxides, which has in case of fourfold coordinated metals the general structure $Me(OR)_4$, where Me stands for the metal cation and R for an organic rest, is as follows

$$Me(OR)_4 + 4H_2O \rightarrow Me(OH)_4 + 4ROH\ (Hydrolysis) \tag{2.3}$$

$$Me(OH)_4 \rightarrow MeO_2 + 2H_2O\ (Polycondensation). \tag{2.4}$$

In the polycondensation process, a metal oxide network is built. The hydrolysis process starts after the precursor is exposed to water. In this work, titanium dioxide and zirconium dioxide are prepared from sol-gel processes as pure oxides or as mixtures. The most important oxide in this work is titanium dioxide. From now on, the presentation of the sol-gel process will concentrate on this oxide. The sol-gel processes for zirconia preparations are analogous. The oxide network can be built up in two reactions, the alcoholation and the oxolation reaction, which are in the case of titania synthesis:

$$Ti - OH + OR - Ti \rightleftharpoons Ti - O - Ti + ROH\ (Alcoholation) \tag{2.5}$$

$$Ti - OH + OH - Ti \rightleftharpoons Ti - O - Ti + HOH\ (Oxolation). \tag{2.6}$$

The precipitates from the sol-gel process may include titanium hydroxide, oxyhydroxide $TiO(OH)_2$ or hydrated TiO_2 ($TiO_2 \cdot 2H_2O$ and $TiO_2 \cdot H_2O$) [45].

Some great advantages of the sol-gel process are the possibility to prepare large amounts of powders with high chemical purity [46], and the possibility to influence the reaction products by process parameters [47]. Next to this, it allows the preparation of powders, wires, coatings and bulk materials [48]. The sol-gel process offers the synthesis of materials at low temperatures and simple coating of large surfaces [49].

After $Ti(OR)_3(OH)$ molecules are built, one of the two possible condensation reactions, alcoholation or oxolation, start immediately. Further hydrolysis of the remaining OR-groups is not necessary [50]. Thus, if only small amounts of water are added in the hydrolysis step, the metal alkoxide might be hydrolyzed only partially with remaining organic groups. In a first step of particle growth in the polycondensation process, small nuclei of about 2-10 nm are generated. These nuclei later grow to larger crystallites. The primary particles built in the first step may then aggregate to larger secondary particles of about 300-1000 nm [51].

The reaction conditions of the sol-gel process influences the particle size and the crystalline phases built in the reaction products during heat treatment [2]. Also the degree of crystallinity depends on the reaction parameters. Next to these characteristics, the morphology of the particles is also influenced by the synthesis conditions [52]. In how far the reaction conditions influence the particle characteristics is not fully understood and thus most preparation methods are based on empirical knowledge [53].

In sol-gel processes, not only powders can be prepared, but also gels. When the $Ti(OH)_4$ monomers form the titania network, it can grow to any size. If the network reaches through the entire solution medium, the reaction product is called a gel [44]. By addition of large amounts of hydrochloric acid to the titanium tetraisopropoxide precursor used in this work, titania gels can be synthesized, compare e.g. ref. [54]. In this work, all prepared samples are made of titania powder particles, thus gels should not be discussed in detail here. More about gels can be found in [44].

The sol-gel process is especially interesting for the preparation of catalysts, because the derived materials usually have high specific surface areas and show high porosities [55]. Especially for the preparation of transition metal oxides, sol-gel techniques are often used [56].

The structure of the built clusters is primarily dependent on the relative reaction rates of hydrolysis and condensation reactions [47]. These reaction rates are influenced by the reaction temperature, the dilution of the reactants (grade of dilution and solution medium), the relative amounts of the reactants and by the addition of catalysts in the form of electrolytes, which change the pH of the reaction environment, etc [2].

Other parameters are the electrophilicity of the metal and the partial charge of the splitted group [44]. Also the oligomerization of the alkoxide plays a role, TTIP is known to have a monomer structure [44]. The length of the organic ligand chain has an influence on the size of the primary particles built in the solution and on the crystallization behavior of the resulting product [44]. A description of other alkoxide characteristic effects on the reaction rate can be found in [44]. Many of these parameters are investigated for the preparation of silica colloids from the sol-gel process. However, the results obtained for the preparation of silica should be transferred to transition metal oxides carefully, because experimental results of transition metal alkoxide hydrolysis show that sometimes development trends with a certain parameter are inverse of those obtained for silica. Silicon composites are maybe the best investigated compounds in sol-gel chemistry. Transition metal oxides distinguish from silicon alkoxides mainly in two points [44]: Transition metal alkoxides are much more reactive with respect to hydrolysis and condensation due to the lower electronegativity of the transition metals and the occurrence of more than one stable possible metal coordination. Due to the rapid hydrolysis and condensation of transition metal alkoxides, the reaction chemistry is very difficult to investigate and there is much less work done about it in contrast to the work and knowledge available for silicon compounds. Secondly, an important parameter of the metal alkoxide influencing the precursor reactivity is its possibility to increase the coordination number of the metal cation. If N is the highest possible coordination number for a certain alkoxide and Z is its oxidation state in the precursor molecules, then the reactivity of the precursor increases with an increase of N-Z [57]. Silicon has four bonds in the alkoxides and four ones are the highest possible coordination number. Transition metal alkoxides have four bonds in the alkoxides but six is the highest possible coordination number.

The precipitates of the sol-gel process are amorphous in most cases. In general, there has to be further treatment of the powders to allow them to crystallize. This can be achieved by annealing [26] or by hydrothermal treatment [25, 58]. A detailed description of the crystallization occurring during the annealing step and the problems resulting from it will be described in the following section.

In a hydrothermal treatment, the pH value and the composition of the liquid in which the particles are treated has an influence on the growing processes of the particles [58], as will be explained in the next section. It can be assumed that the first small crystallites built in the sol-gel process undergo the same effects. Being in the reaction solution, the material is kind of hydrothermally treated at room temperature. In the drying process, taking place at room temperature in this work, the material is moistened with the reaction medium and thus again hydrothermally treated at room temperature. The effect of the reaction medium and the hydrothermal treatment medium on the TiO_2 structure are similar to each other, which agrees with this assumption.

Next to pure titania samples, TiO_2-ZrO_2 composite samples are prepared from sol-gel processes in this work. In the case of these samples, the reaction steps for the preparation from metal alkoxides are given by Reddy and Khan [59]:

$$Ti(OR)_4 \cdot Zr(OR)_4 + 8H_2O \rightarrow Ti(OH)_4 \cdot Zr(OH)_4 + 8ROH \tag{2.7}$$

$$nTi(OH)_4 \cdot Zr(OH)_4 + nTi(OH)_4 Zr(OH)_4 \rightarrow (Ti-O-Zr-O-Ti-O-Zr)_n + nH_2O. \tag{2.8}$$

The Ti-O-Zr bindings may lead to the formation of crystalline species of $ZrTiO_4$, as will be explained in the next section. With sol-gel chemistry, it is possible to prepare mixed composite oxide nanomaterials with high homogeneity of the oxide distribution [60].

A very important point for the investigation of the reaction mechanisms in sol-gel processes is that the principal reaction mechanisms are independent of the used alkoxide. The principal structure $Ti(OR)_4$ leads to an increase of the coordination number from four to six during hydrolysis. Because this change of the coordination number is the main driving force of the chemical reaction, the results gained from the investigations of a certain titanium alkoxide should be transferable to other titanium alkoxides and also for methods like the preparation of TiO_2 from $TiCl_4$ [42].

2.4 Crystallization of nanostructures

The nanostructures which are synthesized in the sol-gel process and annealing procedure are small crystallites or clusters, which have dimensions in the size range between 1 and 100 nm. A crystal is in general an ensemble of atoms or molecules, which are ordered in certain spacial arrangements. The whole arrangement of atoms or molecules can be represented by units called elementary cells, which consist of three vectors $\vec{a_i}$ with i=1, 2, 3 in a three dimensional space. Every crystal is built up from translations of the elementary cell in all space directions. For every crystal, it is possible to find more than one cell, which can build up the atomic arrangement by translation. A special cell is the one which is able to assemble the structure by translation and has the lowest possible cell volume. This cell is called the primary cell. Thus, every point in the lattice can be described by a vector $\vec{R}$ with [61]

$$\vec{R} = n_1\vec{a}_1 + n_2\vec{a}_2 + n_3\vec{a}_3,\ n_i \in \mathbb{N}. \tag{2.9}$$

The arrangement of atoms in the elementary cells is given by the so called atomic basis. This basis can be a single atom, a molecule or a group of atoms. The elementary cell and the basis describe the crystal structure.

For many crystalline composites, there is more than one possible crystalline structure, which means more than one spatial arrangement of the atoms or molecules. This is called polymorphism, the different structures are called crystalline phases or polymorphs. The most stable crystalline structure is that one with the highest cation-cation distances [42]. Polyhedral substructures in a crystal cell can share corners, edges or faces. The substructures sharing corners of the long polyhedra axis have the highest cation-cation distance and are thus most stable configurations. This reduces the electromagnetic repulsion forces between the positively charged ions. In the case of TiO_2 and ZrO_2, there are three polymorphs existing at normal conditions. Thermodynamically, the most stable phase can be determined by the Gibbs free energy [62]

$$G = E + PV - TS, \tag{2.10}$$

where E is the inner energy, which means mainly the crystallization energy, P is the pressure, V the volume, T the temperature and S the entropy. The free energy shows that the phase stability is also a function of the pressure. All samples are treated at ambient pressure in this work. There are three polymorphs known for TiO_2 at ambient pressures. The change in the cell volume with respect to changes in the temperature or due to phase transformations is very small, thus the equation can be simplified to [62]

$$G \sim E - TS. \tag{2.11}$$

At low temperatures, the free energy is mostly determined by the crystallization energy of a certain polymorph. With increasing temperature, the second term in Eq. 2.11 becomes more important, and another polymorph with a higher crystallization entropy may reduce the free energy to lower values and thus be more stable. In the nanoregime, there is a surface pressure on the crystalline bulk, which might influence the free energy.

The arrangement of atoms or molecules in a crystalline structure has important consequences for the electrons in a crystal. They are confined in a three dimensional periodic potential. Thus, the potential can be written as a Fourier expansion. The Schrödinger equation of an electron moving in such a potential can be solved by an expansion of plane waves with wave vector $\vec{k}$. The eigenvalues determined from this solution can be indexed by k. The amount of all possible solutions builds an energy band, equivalent to the energy levels of electrons in atoms. The chemical bonding of the atoms or molecules in the solid state of course strongly influences the band structure by its influence on the potential. The width of a band is dependent on the overlap between the electron waves of the neighboring atoms [63].

In the case of insulators and semiconductors, there is a gap occurring between energy bands. The bands of lower energy than the Fermi energy are called valence bands, the band of higher energy is the conduction band. The Fermi energy is the energy of that band which is the one with the highest energy which is filled at T=0 K in metals [63]. In semiconductors, the Fermi energy is located in a band gap between the valence bands and the conduction band. In insulators, the band gap is very large ($\gtrsim 3\,\mathrm{eV}$) and electrons cannot travel it to the conduction band. In case of semiconductors the band gap is much smaller ($\approx 1\,\mathrm{eV}$) and if electrons get sufficient energy (for example by heating of the solid), they can travel to the conduction band [63].

In the nanoregime, additional factors become important for the crystallization processes. The most significant one is the increasing relative fraction of the crystallite surface. This leads to an additional term which concerns the surface free energy, see for example [23]. Being dependent on the particle size, the free energy of the specific surface and thus the stability of crystalline phases is a function of the crystallite size in the range between 1 and 100 nm. The usually occurring polymorphs of TiO_2 in ambient conditions are called anatase, brookite and rutile.

Other phases are known, for example hollandite TiO_2 and ramsdellite TiO_2 [64], but are only occurring at extreme conditions and are thus not considered here.

Polymorph	Cell type	Length of a	Length of b	Length of c	ρ [g/cm^3] [56]
Anatase	Tetragonal	3.785	3.785	9.541	3.84
Brookite	Orthorhombic	5.436	9.166	5.135	4.11
Rutile	Tetragonal	4.594	4.594	2.958	4.26

Table 2.1: Structural parameters of anatase, brookite and rutile. Lattice parameters of anatase from [65], those of brookite and rutile from [66]. All axis lengths are given in Å.

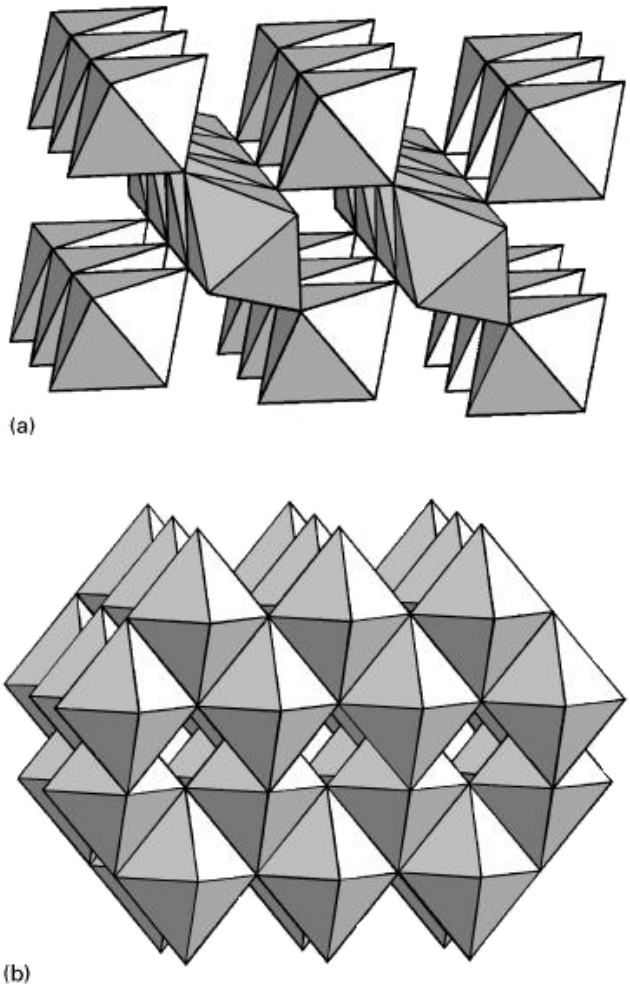

Figure 2.1: Arrangement of TiO_6 octahedra in rutile (part a) and anatase (part b). Picture taken from [42].

All three TiO_2 polymorphs are built up of octahedral TiO_6 subunits. The difference is just the arrangement of the subunits and the axis length of the octahedra. In anatase TiO_2, there is a titanium atom in the center of the octahedron and four oxygen atoms at the ends of the 1.934 Å short axis and two at the 1.980 Å long axis. In rutile, the distances of the central titanium atom to the first neighboring oxygen atoms are longer, the short axis length is 1.949 Å and the long ones are 1.980 Å long.

On a macroscopic scale, rutile is the most stable phase due to the chain like structures, which are built up of TiO_6 octahedra sharing corners at the end of the long axes and by this leading to a linear arrangement of Ti cations, maximizing the cation distances (Fig. 2.1 a) [42]. In contrast, Zhang and Banfield found by theoretical investigations of the surface free energy as a function of the particle size, that up to sizes of about 11 nm, the anatase phase has a lower free energy than rutile and brookite [23]. Usually, the anatase structure is not stable due to the structure, which also contains TiO_6 octahedra, but if three of those ones are regarded, only two of them are linked by corner-sharing and one is added by edge-sharing perpendicular to the chain that is built-up by the other two (compare Fig. 2.1 b). This is also the case for the brookite structure. This configuration has lower cation distances than the rutile structure and is thus less stable. In a small intermediate region of the particle sizes, the brookite free energy values are very close to those of the anatase phase [23]. As a consequence, brookite is often found to occur next to anatase in sol-gel derived TiO_2 [54]. Because samples with pure anatase crystalline phase can be synthesized, it can be assumed that the reaction kinetics in the crystallization of anatase rules the process instead of the thermodynamics. Brookite is also very important for the phase transitions to rutile, because it is a polytypism of anatase and can transform to anatase as well as to rutile. From particle sizes of 35 nm on, rutile is the most stable polymorph. In another work of Zhang and Banfield, it is found that also the phase transition from amorphous TiO_2 to anatase is size dependent [67]. In this work they also show that the nucleation of anatase seems to happen in the boundary regions of attached amorphous particles. The nucleation of new crystalline phases at particle interfaces also seems to be important for the anatase-brookite phase transition. It shows up that the structural characteristics of TiO_2 nanoparticles are dependent on each other. A small particle size leads to a higher specific surface of the material, but also has an influence on the crystalline phase stability.

Also the reaction additives have an influence on the crystallization processes. The dilution of the precursor in alcohol is used to reduce the high reactivity of TTIP. The effect of alcohol solution of the precursors during the reaction step was investigated by Song et al. [51], who studied the influence of the dilution of TTIP in methanol, ethanol, isopropanol and sec-butanol and the effect of the amount of added alcohol. They found that the phase transition temperature from amorphous TiO_2 to the anatase phase increased with increasing amount of added ethanol. Also the specific surface area was found to be dependent on the alcohol dilution. This is because the added alcohol has also an important influence on the agglomeration of the particles.

Rossmanith et al. [2] studied the influence of the chemical reaction path on the products of sol-gel processes combined with miniemulsion techniques. They studied the influence of the reaction temperature, added electrolytes, namely hydrochloric acid and sodium hydroxide, the amount of added surfactant and the annealing temperature. In case of the influence of added electrolyte, they found that hydrochloric acid leads to phase transitions, especially from the anatase to the rutile phase while the addition of sodium hydroxide leads to relatively pure anatase phase.

The favored phase transition from the anatase to the rutile phase in TiO_2 samples prepared with hydrochloric acid was announced by Gopal et al. [42]. They explained that the hydrolysis reaction rate is enhanced by a destabilization of the Ti cation-organic bonds in the alkoxide precursor due to the formation of a positively charged ion cloud around the anionic ligands. This charge cloud reduces the negative charge of the ligand with respect to the metal cation and thus the attractive electromagnetic force determin-

ing the strength of the bonding. On the other side, the condensation reaction rate is reduced due to repulsive forces between the clusters formed in the reaction, caused by a cloud of positive charges from the electrolyte. This group also found that the polymorph of the reaction product is dependent on the amount of added acid. High amounts of acid as reaction medium favor the formation of the rutile phase while small amounts favor the anatase phase.

The reaction product is not only influenced by the amount of acid, but also by the pH value of the reaction medium and the type of ions in the solution [42]. An influence of the reaction pH value in hydrothermal treatment was investigated by Isley and Penn [25]. They investigated samples treated with hydrochloric acid and found that at pH 0, the samples were nearly fully crystallized while at pH 3, there were high remaining amorphous concentrations. The influence of different electrolytes was investigated by the use of hydrochloric acid and nitric acid (HNO_3) at pH 3. The sample prepared with HCl had a much higher remaining amorphous concentration than that one prepared with HNO_3. As an additional result, they found that the amount of brookite in the samples was strongly dependent on the pH value and the type of electrolyte.

Another important point in context with the addition of acids for the structure of resulting materials from the sol-gel process is the solubility of TiO_2. This solubility is dependent on the titania polymorph. Amorphous titania has a higher solubility than anatase. Next to this, the solubility is strongly influenced by the solute temperature and the addition of acid to the solute medium [68]. The solved amorphous TiO_2 can adsorb on anatase particles or might built new nuclei and particles and thus lead to structural changes.

The particle size decreases with increasing amount of added HCl solution [47]. Next to this effect, the particle size generally increases with increasing pH value if acids or bases are added to the reaction medium [69].

The amount of added water is especially important in the question if the hydrolysis reaction can be completed or not. If the water amount added to an alkoxide is reduced, not all Ti-OR bonds can be hydrolyzed to Ti-OH bonds [70]. These remaining alkyl-groups prohibit the crystallization of the material. Thus, the water to alkoxide ratio can be expected to have an influence on the degree of crystallinity and the particle size. It is obvious that the water to alkoxide ratio also plays a role if different amounts of aqueous electrolytes are added to the reaction solution.

The effect of the water to alkoxide ratio was investigated by Wang and Ying [47] to decrease the particle size with increasing water to alkoxide ratio. They explained their results with the favoring of nucleation processes instead of particle growth if the hydrolysis is finished due to the high water amount. They also found that the degree of crystallinity increases with increasing water to alkoxide ratio. Also the intermediate reaction product species of the sol-gel process were found to be influenced by the amount of added water [21]. If the amount of added water is low, the polycondensation step leads to more linear polymers with a low number of crosslinks. If the amount of added water is high on the other side, the polymers resulting from the polycondensation process are much more interconnected and have many crosslinks [21].

Isley and Penn [25] found that the amount of added water in hydrothermal treatment influences the concentration of brookite built in the samples. Choi and Park [71] showed that also the reaction atmosphere has an influence on the crystallinity and phase composition of the reaction products.

During heat treatment of titania powders, phase transitions may occur. The first phase

transition occurring is the amorphous-anatase transition. The process was explained by Zhang and Banfield for nanosized titania as follows [67]: Similar to the case of crystalline titania phases, the amorphous-anatase phase transition depends on the sizes of the amorphous particles. The phase transition is suggested to occur at particle sizes of 2.5-3 nm. When smaller particles grow together, the phase transition is able to occur. The phase transition temperature is believed to be between 300 and 400°C. To build up anatase particles from amorphous ones, nucleation and growth of anatase clusters are necessary. This is also similar to the anatase to rutile phase transition. Once when anatase nuclei are formed at the amorphous-amorphous particle interfaces, the amorphous fractions of the powders will crystallize on the anatase surfaces due to atom diffusion. This leads to the growth of the anatase nuclei. Another possibility for the growth of the anatase nuclei is the diffusion of atoms from one anatase particle to another. If two neighboring anatase particles are oriented to each other in certain orientations, they are able to grow to one large particle (growth by oriented attachment). Oriented attachment is also an important point in the anatase to rutile phase transition, as will be explained later. This process of anatase crystallization from amorphous TiO_2 can be expressed by the following steps in the kinematic mechanism [67]

1. Anatase nucleation at the interface of two amorphous TiO_2 particles A_{amorph}. This step has the form
$$2A_{amorph} \rightarrow A_2. \tag{2.12}$$

2. Growth of anatase (indexed by j+1) nuclei due to the diffusion of atoms from the amorphous TiO_2 particles to an existing anatase nucleus (indexed j)
$$A_{amorph} + A_j \rightarrow A_{j+1}. \tag{2.13}$$

3. Growth of anatase particles by redistribution of atoms from one anatase particle (indexed i) to another (indexed j)
$$A_i + A_j \rightarrow A_{i+j}. \tag{2.14}$$

This model is the first one which is able to describe crystallization as well as crystal growth. From equations 2.12, 2.13 and 2.14, it is clear that the crystallization process is dependent on the number of available amorphous particles in the sample. The second step is dependent on the number of amorphous particles as well as the number of anatase nuclei and the third step is dependent on the number of anatase particles.

The brookite phase can be built from anatase particles at anatase-anatase particle interfaces, where structures might occur, which are not present in the anatase particle bulk [72]. They are similar to the brookite structure and work as crystallization nuclei for brookite. The size of these structures is of the magnitude of some elementary cells. The brookite particles can transform to anatase particles as well as to rutile particles. The anatase particles built from brookite to anatase phase transitions are very large, because two brookite particles built one large anatase particle. The attendance of brookite has a strong influence on the formation of rutile. If brookite is present in a sample containing amorphous titania and anatase, the anatase amount can further increase even if a phase transition to rutile occurs because the rutile will first be formed from the brookite content. After all brookite is consumed in the phase transition, phase transition from anatase to rutile will be accelerated and the rutile phase content will grow at the cost of the anatase phase, which will thus decrease finally.

At temperatures between T=400°C-1200°C, anatase transforms into the thermodynamically stable rutile phase [73]. The exact transition temperature is dependent on factors like particle size, aggregation or precipitation history [73]. This phase transformation is a nucleation and growth process. In [74], the authors described that nucleation can take place on the anatase surface, at interfaces or in the particle bulk. They investigated the phase transition in a temperature range of T=465-525°C. It is dependent on sample characteristics and temperature if surface nucleation or interface nucleation is dominant. At low temperatures, nucleation cannot take place at the surface or in the particle bulk, because the thermal movement of the atoms in the anatase bulk is too small. At anatase interfaces, rutile like structures can be formed, which can serve as nucleation sites for rutile. Dislocations can contribute to the interface nucleation. When the temperature increases, the nucleation of rutile can occur at free anatase surfaces, where no TiO_2 particles are attached to the surface. In contrast to the nucleation on interfaces, the surface nucleation does not need rutile like structures as nucleation sites. When the temperature is high enough, the amplitude of the thermal movement of the atoms is high enough for the nucleation of rutile structures in the particle bulk. The transformation rate is limited by the rutile nucleation. From the observation that partially transformed anatase crystallites are hardly found experimentally, it can be deduced that the growth of the rutile particles is very fast. The anatase to rutile phase transition requires the breaking of 7 out of 24 Ti-O bonds in every unit cell. Thus, atoms are displaced during the transformation. Zhang and Banfield [74] suggested that the surfaces of the rutile nuclei/particles move through the anatase particles like a distortion wave. If the temperature becomes very high, anatase bulk nucleation might also occur. For bulk nucleation, more chemical bonds than in surface nucleation have to be cracked up due to the higher number of chemical bonds in the particle bulk. This leads to higher activation energies for this process. The transition temperature decreases if the particle/grain size decreases [73].

Another important factor is the agglomeration of the particles. In another work of Zhang and Banfield it was presented that attached nanocrystallites can grow together to form one large particle [58]. If the particles are attached at certain crystallographic surfaces, the possibility of phase transformations from the anatase to the rutile phase increases. Generally, particles can grow to larger crystalline structures if they are close to each other in agglomerates. Additionally, the interfaces of crystallites in agglomerates may have a free energy different from that of free crystallites. So next to the driving force that the system tries to minimize the surface area due to structural changes, also the minimization of the interface area is a driving force for structural changes.

The classical description of the particle growth and coarsening is made by use of the Ostwald ripening, see for example [75]. Zhang and Banfield showed that especially in the case of nanocrystalline systems, a second mechanism is working, which is the oriented attachment of particles [58]. They showed that anatase particles can attach to each other at certain crystallographic surfaces and built long single crystals which might contain two or more primary particles. This growth mechanism is accompanied by strong coarsening. In the work of Zhang and Banfield, a hydrothermal treatment was used to achieve crystallization, but as it was already mentioned, a kind of hydrothermal effect is assumed to already occur during preparation and drying. This growth mechanism is strongly dependent on the surrounding medium. A very strong effect was observed for HCl with $-\log\{a_{H^+}\} = 3.0$, where coarsened particles consisting of up to 10 primary particles were observed. The authors made the hypothesis that oriented attachment

may be favored by precipitation processes. Thermodynamically, oriented attachment of course also helps to eliminate crystal surfaces which have a high surface energy, thus reducing the energy of the system. Due to this, the oriented attachment of anatase occurs mostly at (112), once in a while at (001) and rarely at (101) surfaces, where (112) has the highest surface energy [58].

As it shows up in the theory of crystallization, grain growth and phase transitions, all these steps can be described like chemical reactions with the amorphous phase or the initial crystalline phases as starting materials and the final crystalline phases as products. Like in chemical reactions, where the valence electrons in the outer atomic shells are responsible for the chemical reaction, the nuclei for phase transformations are built on the particle interfaces. The kinetic theory of chemical reactions often made use of the collision theory. Because the formation of interfaces between nano-crystallites in the synthesis step or in hydrothermal treatment is necessary, this is similar to chemical reactions between atoms or molecules. Thus, these processes can be characterized with measuring of the concentrations of the reactant phases with the characterization possibilities known from chemical reactions. As will be seen later, XANES is such a tool that is able to measure reactant concentrations.

The addition of other metal oxides can prevent the anatase phase from growing and phase changing. Elder et al. [1] and Ranade et al. [76] stabilized anatase by addition of ZrO_2 and MoO_3. The first group explained the stabilization by an encapsulation effect of the added metal oxide. Thus, the anatase particles cannot grow together to build larger particles or interfaces where nuclei for new phases can be formed.

Research groups who prepared and investigated TiO_2-ZrO_2 mixed oxides with varying TiO_2:ZrO_2 ratios found that the building of TiO_2 or ZrO_2 crystallites can only be observed if the TiO_2 or the ZrO_2 fractions in the powders are high enough [77]. Thus, if the titania amount is very high with respect to the amount of zirconia, only TiO_2 crystalline phases are observed, while crystalline ZrO_2 phases are observed if the zirconia concentration is high with respect to the amount of added titania [37].

If the amorphous composites, in which none of the two oxides is present in a much higher concentration than the other one, are heated to higher temperatures of about T>650°C, they become crystalline, but instead of crystallization of pure titania phases or pure zirconia phases in the composites, a mixed crystalline $ZrTiO_4$ phase is built [78]. In the past, this crystalline material has been prepared by solid state reaction of TiO_2 and ZrO_2 powders at temperatures of T> 1000°C [79]. Later, it was found that it can be prepared with the aid of sol-gel processes with mixtures of titanium- and zirconium containing alkoxides. Crystallization of the reaction products occurs during the calcination at lower temperatures of T$\geq$ 650°C [79] in this case. Schiller et al. [13] doped TiO_2 with zirconium and found that at high amounts of added zirconium, the $ZrTiO_4$ crystallizes at high annealing temperatures.

For ZrO_2, there are also three crystalline phases occurring, which are namely the cubic one, the tetragonal and the monoclinic one. Also for ZrO_2, theoretical work has been made to investigate the influence of the particle size on the particle structure, for example by Banard et al. [80].

Polymorph	Length of a [Å]	Length of b [Å]	Length of c [Å]	ρ [g/cm^3]
Cubic	5.12	5.12	5.12	6.09
Tetragonal	5.09	5.09	5.18	6.10
Monoclinic	5.16	5.19	5.30	5.83

Table 2.2: Structural parameters of the three most common ZrO_2 polymorphs. Data from [81].

2.5 Investigation methods

In the next section, the possibilities offered by different characterization methods with respect to the investigation of the important structural parameters determining the applicability and efficiency of TiO_2 based nanomaterials should be discussed. Most of them are based on the use of x-rays as probes for the structural parameters. As will be seen, the combination of the methods leads to the possibility to determine nearly all of the structural factors which are important for the usefulness of the materials. The following section about XAS is mainly written based on "Introduction to XAFS" by G. Bunker [82].

2.5.1 X-ray absorption spectroscopy (XAS)

The probability of an interaction of radiation with a particle in a thin material layer is given by the cross section $\rho\sigma\delta x = \mu\delta x$, with the linear absorption coefficient μ, the interaction cross section σ, the electron density ρ and the matter thickness x.

If electromagnetic radiation is absorbed by media of any aggregate state, its intensity will decrease depending on the thickness x of the media and a factor μ, which is called the absorption coefficient and gives the dependence of the absorption on the media characteristics. Thus, the decrease in intensity I can mathematically be written as dI=Iμdx. Solving this differential equation leads to the Lambert-Beer law:

$$I(x) = I_0 \exp(-\mu x), \tag{2.15}$$

where I_0 is the radiation intensity before the absorption process. The absorption process itself can be described in terms of quantum mechanics. The electron wave can be described by wave equations ϕ_f and ϕ_i, the indices accounting for the initial and the final state of the electron wave. The transition rate W can be described with the aid of Fermi's golden rule, see e.g. [82]

$$W = \frac{2\pi}{\hbar} |\left\langle \phi_f | H' | \phi_i \right\rangle|^2 \rho, \tag{2.16}$$

with H' being the Hamiltonian of the interaction between impinging x-ray wave and electron and ρ the density of states.

The development of the absorption cross section with increasing energy behaves like a monotonically decreasing function with approximately $1/E^3$ dependence, intercepted by sharply increasing edges called absorption edges. Regarding the energy range up to about 1 keV above the absorption edges, an oscillatory structure shows up in spectra of samples where atoms are bound in molecules, fluids or solid states.

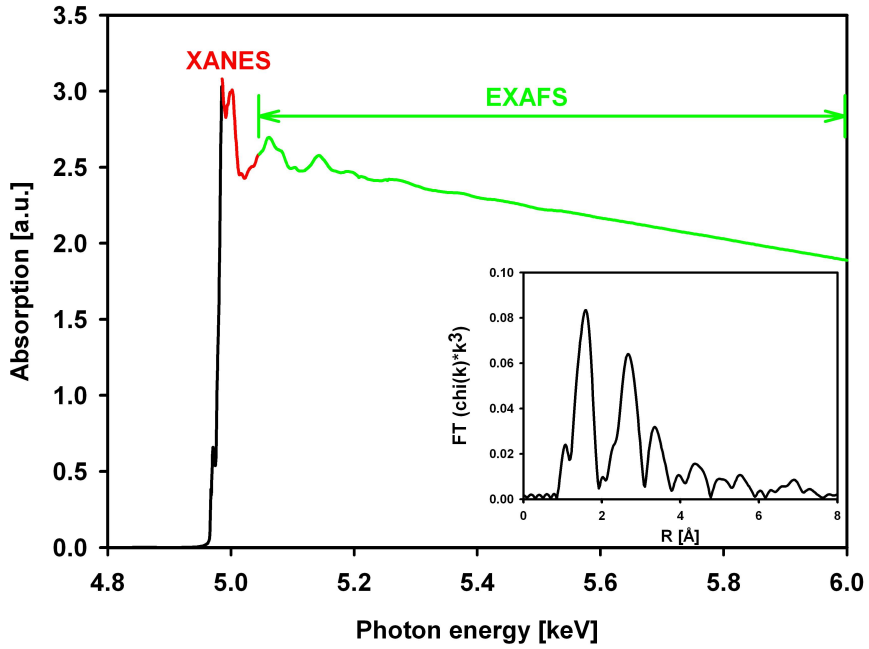

Figure 2.2: X-ray absorption spectrum of a titania sample annealed at T=500°C for four hours. The region of the x-ray absorption near edge structure (XANES) is highlighted in red, the one of the extended x-ray absorption fine structure (EXAFS) is highlighted in light green. The presented spectrum is corrected for the pre-edge line. The embedded graph presents the Fourier transformed spectrum in R-space.

The structure above the absorption edge can be divided into two regions, which are presented in Fig. 2.2. The first region extends over the first 30-50 eV above the absorption edge and is called the x-ray absorption near edge structure (XANES). The second one is chosen to be about 800-1000 eV above the absorption edge in practice and is called the extended x-ray absorption fine structure (EXAFS). The main difference between these two regions is that in the XANES, multiple scattering is of high importance, while it has much less effect on the EXAFS. This makes the EXAFS to the part of the x-ray absorption spectra which can be understood much easier. Nevertheless, it is possible to get important information about the sample structure from the XANES region by using a fingerprint technique, which is explained in more detail later in this section.

The absorption coefficient of a free atom is called μ_0. The XAFS is due to the scattering of the photoelectron wave at surrounding atoms and the interference of the scattered and the incoming wave. If the fraction of absorption caused by these effects is called χ, the total absorption coefficient can be written as $\mu(E)=\mu_0(\mathrm{E})(1+\chi(\mathrm{E}))$ or

$$\chi(E) = \frac{\mu(E) - \mu_0(E)}{\mu_0(E)}. \tag{2.17}$$

With the approximations that only a single electron is regarded, which is described as a plane wave and that only single scattering occurs, Stern, Sayers and Lytle presented a simple equation for χ. In this equation, χ is presented as a function of the wave vector k instead of the energy E. The transformation is given by

$$k = \sqrt{\frac{2m(E - E_0)}{\hbar^2}}, \tag{2.18}$$

where m is the electron mass, E is the x-ray energy and E_0 the energy of the absorption edge.

The EXAFS equation, based on the single scattering approximation, is given by Rehr and Albers in the following form [83]:

$$\chi(k) = -\sum_j S_0^2 N_j \frac{|f_j(k)|}{kR_j^2} \exp(\frac{-2R_j}{\lambda(k)}) \exp(-2\sigma_j^2 k^2) \sin(2kR_j + 2\delta_c + \Phi). \tag{2.19}$$

In this equation, S_0^2 is the amplitude factor, N_j is the number of atoms in the j-th coordination shell, $f_j(k)$ is the backscattering amplitude, R_j is the interatomic distance, $\lambda(k)$ the mean free path and σ_j is a factor which is introduced to consider the thermal fluctuations of the bonding length. The sum extends over all coordination shells. This equation is valid for K and L_1 absorption edges, where only s $\rightarrow$ p transitions are allowed. For $L_{2,3}$-edges, the final states can be d or s states, which makes the equation more complicated. The $\chi(k)$ spectrum consists of a sum of damped sine waves. In the following, the physical meaning of the different contributing terms of the EXAFS equation is given for the approximation of single-scattering.

$S_0^2 \frac{N_j}{kR_j^2}|f_j(k)|$: The amplitude of the EXAFS signal is mainly due to the coordination number N_j of the atomic species surrounding the absorber atoms. The other factors in this part are the wave vector k, the passive electron reduction factor S_0^2 and the distance between the absorber atom and the scattering atoms R. Thus, the amplitude of the EXAFS signal is linearly dependent on the coordination number and is alleviated by $1/kR_j^2$ due to the decrease of the intensity of the spherical electron wave by travelling through the material. The backscattering amplitude is dependent on the type of neighboring atoms. The more electrons are bound to the backscattering atom, the higher the backscattering amplitude. S_0^2 considers a decrease in the coherence due to multi electron excitations.

$\exp(-2R_j/\lambda(k))$: This term concerns the mean free path of the electron wave in the material. This is the length the electron can travel through the material without interaction. At high energies, the photoelectron will interact with the surrounding electron gas in the material. This interaction can be described as an interaction of quasi-particles by a complex, energy dependent function which is called self-energy. Due to the complex nature of this potential, the probability of presence of the photoelectron is no longer conserved. By the decay of the probability, the mean free path is given. While travelling the material, the electron wave loses coherence. As a consequence of the mean free path, the XAFS spectra are only sensitive to the short range order of the samples. This term leads, of course, to a faster decrease of the amplitude of the signal than the $\frac{1}{kR_j^2}$ term above, because of the exponential dependence. Due to the dependency of λ on the energy, multiple scattering is much more important for the XANES than for the EXAFS.

$\exp(-2k^2\sigma_j^2)$: The σ is a sum term of the disorder composed of the thermal and the static disorder. The thermal disorder is considered by the Debye-Waller factor. This factor includes the oscillations of the atoms in a certain material around their rest position due to thermal movement. For small values of k, the wavelength is large and

the wave contributions are in phase. At large wavelengths, the contributions are not in phase. With increasing temperature, the mean square deviation of the path length, σ_j^2, increases. The static disorder is especially important in the investigation of amorphous materials. It is mainly due to the statistical distributions of the binding lengths of the materials atoms [82].

$\sin(2kR_j+2\delta_c+\Phi)$: Due to the scattering of the photoelectron wave at the surrounding atoms, the phase of the incoming and the outgoing wave are shifted with respect to each other. The first and the second term in the argument of the sine function have to be multiplied by two due to the traverse of the scattering path for two times: First, the path from the absorber atom to the scatterer, second the same way back. Fast oscillations belong to large path length. The phase shift of the final state of the absorber atom is given by δ_c, the phase shift of the backscattering process is considered in Φ.

As can be seen from the above explanations, there is no need for a crystalline arrangement of the sample atoms to observe an EXAFS signal. Thus, the method can be used for any solid, amorphous or crystalline, as well as for liquids. As it is also obvious, the amplitude of the EXAFS signal is proportional to the coordination number and anti-proportional to the distance of the absorber atom and the scatterers. Thus, the values of these two parameters can be derived from the measurement of the x-ray absorption. In this way, EXAFS provides information on the local environment of the absorber atoms.

Bond lengths and coordination numbers can be determined from the fitting of the measured spectra by theoretically calculated ones. The measured spectra are transformed to $\chi(k)$ spectra. Fitting can be performed with data in the k-space or in R-space.

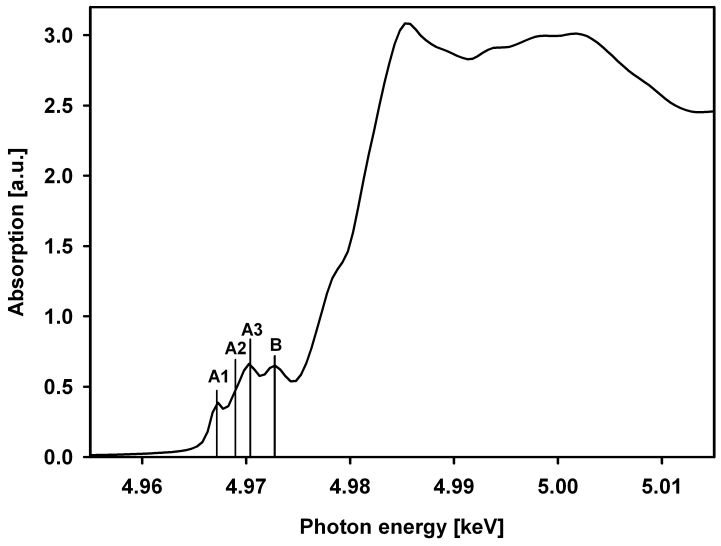

Figure 2.3: XANES spectrum of a TiO_2 sample after annealing at 500°C for four hours with pre-edge peaks labeled by the notation usually used in literature.

The structure of the XANES region is dependent on the electronic transitions which are possible in the material and thus of course on the materials chemical and spatial structure. Thus, if the chemistry of the sample changes due to a chemical reaction, the XANES structure should also change, allowing to follow the chemical reaction by following the changes in the XANES structure. For example, the reduction of cerium was

studied by fingerprinting with linear combination x-ray absorption near edge structure (LC-XANES) [84]. Also other chemical reactions can be investigated with LC-XANES if the structure of the reaction educts and products differ from each other, leading to different structures of the XANES spectra. As it has been described in section 2.4, the crystallization process and the transformation of different polymorphs into each other can be described like chemical reactions. The structures of the polymorphs are different from each other and thus, every polymorph and the amorphous phase has different XANES structures. The analogues to the reactants in this work are the polymorphs, which contribute to the detected signal as a superposition of the signal from single polymorphs. Those ones contained in the samples and thus necessary for the LC-fit can be determined in a principal component analysis (PCA) [85].

In PCA, the absorption spectra are regarded as vectors, spanning a vector space. The reference spectra used for the linear combination fits are analogous to basis vectors. The basis vectors are the smallest possible set of vectors which can be used to describe a vector space. In PCA for LC-XANES, the measured XANES spectra are linear combinations of the XANES reference spectra belonging to the phase pure polymorphs. Thus, with increasing concentration of the polymorphs included in the samples, the reference spectra have a more important weight in the linear combination. All reference spectra which have a low weight value are not included in the measured samples in significant amounts and thus do not have to be taken for linear combination fits [85].

Next to these possibilities, it is also possible to examine the sol-gel process itself with the help of XAS. Stötzel et al. [86] used quick extended x-ray absorption fine structure measurements to investigate short lived intermediate products of the sol-gel preparation of TiO_2 from the TTIP precursor.

As can be observed in the presented spectrum in Fig. 2.3, there are structural features on the low energy site of the absorption edge. These structural features are called pre-edge peaks. The pre-edge peaks are due to transitions from the 1s orbital of titanium to unoccupied bound states. The peak positions are a function of the structural neighborhood of the absorber by hybridization effects of overlapping atomic orbitals. This fact leads to the possibility of getting structural information from the positions of the pre-edge peaks. A physical explanation of the transition origin can be derived from a pseudo atomic model. This leads to the description of the peaks as $1s \rightarrow 3d$ and $1s \rightarrow 4p$ transitions. The nature of the pre-edge structure has been investigated experimentally as well as theoretically [9, 20, 87, 88, 89, 90].

In a more detailed description, the Ti absorber has to be regarded in the octahedral environment of the TiO_6 subunits the titania structure is built of. In this octahedral environment, the oxygen atoms are negatively charged with respect to the titanium cation. Due to the attraction potential between the metal cation and the anions, the solid state bands in an ordered octahedral environment belonging to the orbitals of titanium pointing in the direction of oxygen atoms are lower in energy. The final band states are made up by hybridization of orbitals with Ti 3d symmetry and, to a lower extend, of O 2p symmetry [87]. These bands are the 3d-t_{2g} bands in the case of TiO_2, which are built up of directed orbitals like d_{xy}, d_{yz} and d_{zx}. On the other hand, orbitals which are not directed, like $d_{x^2-y^2}$ or d_{z^2}, which leads to the 3d-e_g bands are not lowered in energy. Thus, there is a split of the 3d-t_{2g} and 3d-e_g bands in an octahedral environment.

The notation usually used in the literature for the pre-edge peaks is presented in Fig. 2.3. The peaks A1 and A2 are assigned to transitions from the Ti 1s orbital to 3d-t_{2g} non-bonding bands, while A3 can be assigned to anti-bonding 3d-e_g bands. Peak

A1 has a high fraction of quadrupole character, which can be proved by the sensitivity of its intensity on the beam polarization [88]. The hybridization of the orbitals building the final states for the A1 transition takes place between the absorber and the first Ti coordination shell at a distance of 3.04 Å. The peak results from a band from built excitons or from a 1s $\rightarrow$ $1t_{1g}$ transition [9]. Peaks A2 and A3 belong to hybridization of absorber orbitals with the second Ti coordination shell at a distance of 3.78 Å. They can be assigned to 1s $\rightarrow$ $2t_{2g}$ and 1s $\rightarrow$ $3e_g$ transitions [9]. Hybridization always involves the oxygen coordination shell between the titanium shells [91]. The peak B can be assigned to an a_1 orbital transition [89]. It is mainly made up of Ti 4p character orbitals hybridized with Ti 4s and/or O 2p orbitals. The pre-edge peak intensity is strongly dependent on the symmetry of the absorber environment because it determines in how far the orbitals may overlap and thus how strong the hybridization is. Jiang et al. [88] studied the influence of the binding lengths and angles on the pre-edge peak intensity and found that the binding length has a strong influence, while effects due to changes in the binding angles are small.

The A2 and A3 peaks have another important dependency, which is that on coordination number of the titanium absorber. The A2 peak can be assigned to five-fold coordination, while A3 can be assigned to six-fold coordination of the absorber atom with oxygen atoms [92]. From this assignment, qualitative statements about the crystallite sizes can be made. Five-fold coordination can mostly be found on the surface of crystallites, while the theoretically predicted six-fold coordination can be found in the crystallite bulk [20]. The smaller the crystallite is, the larger the surface will be with respect to the volume and thus a decrease in the crystallite size leads to an increase in the A2 peak intensity, while the A3 peak will decrease due to the lower number of bulk titanium absorbers. Luca et al. [20] investigated the dependency of the A3/A2 peak intensity ratio on the particle size and surface to volume ratio. They found a linear relationship between the surface to volume ratio and the peak intensity ratio of A2/A3, which is in accordance with the theory described above.

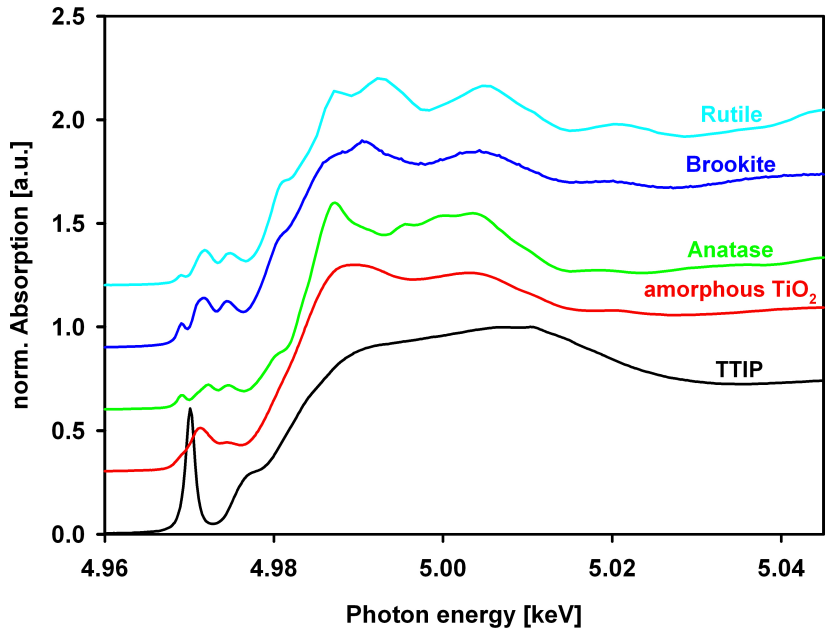

Figure 2.4: XANES reference spectra of the three titania polymorphs regarded in this work, together with those of amorphous titania and the TTIP precursor.

Fig. 2.4 presents reference XANES spectra of the titania polymorphs anatase, brookite and rutile, of amorphous titania as well as the TTIP precursor. As it shows up, the pre-edge peak of the TTIP is much higher with respect to those of amorphous titania or the crystalline polymorphs. The polymorphs have the lowest pre-peak intensity, while that of the amorphous titania sample is in the middle. This is due to the four-fold coordination of TTIP. The hybridization, which gives the ability for the transitions leading to the pre-edge structures, is only possible because the presented titanium structures do not have an inversion center. Especially in the case of the titania polymorphs, which have octahedral symmetries, inversion centers would lead to a drastic decrease down to vanishing of the pre-edge intensity [88].

From the above descriptions, it can be concluded that it is possible to determine the structural environment of the absorber atoms by the determination of the pre-edge peak positions and intensities. Indeed, this possibility was investigated by several authors for titanium x-ray absorption edges. For example, Farges et al. [93] found that the intensities and positions of the A3 pre-edge peak in several oxygen containing titanium composites are a function of the titanium coordination number. Although there are some critical voices that the determination of the coordination environment has to be done carefully [88], pre-edge peak position and intensity analysis is used for structure determination, see e.g. [20, 94].

2.5.2 X-ray diffraction (XRD)

When x-rays interact with matter, the interaction happens between the radiation and the electron density of the material. The electron density in the material is dependent on the position and the number of atoms, as well as on the number of electrons in an

atom. The intensity of the scattered radiation is given by the square of the structure factor F($\vec{k}$) [95]

$$F(\vec{k}) = \sum_n f_n exp(i\vec{k}\vec{r_n}). \tag{2.20}$$

The intensity of the scattered radiation is the product of F($\vec{k}$) with the complex conjugated F*($\vec{k}$). The structure factor itself is the Fourier transform of f_n, the atomic form factor. This factor describes the scattering power of the atoms included in the unit cell. X-rays are scattered by the electrons in the atomic shells and thus it is clear that the atomic form factor should be dependent on Z, the number of electrons in the atom. Due to the fact that the square of the form factor determines the scattered intensity, intensity should be approximately proportional to Z^2. The atomic form factor is the sum over all single electron scattering factors and is given by [95]

$$f_n = \sum \int_0^\infty \rho(\vec{r}) exp(i\vec{k}\vec{r}) dV. \tag{2.21}$$

The electron charge density at a certain point $\vec{r} = |\vec{r}|\vec{e}_r$ in distance $|\vec{r}|$ and direction $\vec{e}_r$ from the observer is given by $\rho(\vec{r})$. Thus, the structure factor given by Eq. 2.20 is the Fourier transform of the electron distribution of the elementary cell.

Due to the fact that the atoms are arranged in the lattice planes, the radiation is scattered at these planes. The radiation from different lattice planes, which are close to each other, is coherent and thus scattered radiation from lattice planes which are arranged parallel to each other can interfere. Positive interference can be observed, if the path difference between the radiation fractions from different lattice planes is equal to an integer multiple of the wavelength, equivalent to the interference conditions known from optics. With geometrical considerations, the Bragg equation, giving the condition for constructive interference, is found to be [95]

$$2d_{hkl}\, sin(\theta) = n\lambda, \tag{2.22}$$

where (hkl) are the Miller indices of the lattice planes, λ is the wavelength of the impinging x-rays and d_{hkl} is the distance between the lattice planes with the Miller indices hkl. The information emerging from XRD experiments is due to the reflection of the impinging radiation at the lattice planes. Thus, a coordinate system based on the lattice plane coordinates would be very suitable for XRD. Such a coordinate system is the reciprocal lattice. The connection between the lattice vectors of the direct space $\vec{a_i}$ and the reciprocal space $\vec{b_i}$ is given by [95]

$$\vec{b_i} = 2\pi \frac{\vec{a_j} \times \vec{a_k}}{\vec{a_i} \cdot (\vec{a_j} \times \vec{a_k})} \tag{2.23}$$

with

$$\vec{a_i} \cdot \vec{b_j} = 2\pi\delta_{ij} = \begin{cases} 0 \quad for \quad i \neq j \\ 2\pi \; for \quad i = j \end{cases} . \tag{2.24}$$

As it shows up in these equations, the i-th direct lattice vector and the j-th vector of the reciprocal lattice are always perpendicular to each other if i≠j. Diffraction peaks occur if the difference of the impinging wave vector $\vec{k_0}$ and the reflected wave vector $\vec{k_i}$ is

a space vector of the reciprocal lattice, given by $\vec{G}$= $m_1\vec{b_1}$ +$m_2\vec{b_2}$+$m_3\vec{b_3}$, $m_i \in \mathbb{N}$, which is called the Laue condition

$$\vec{k_i} - \vec{k_o} = \vec{G}. \tag{2.25}$$

It shows up in the Bragg equation that for a fixed wavelength λ impinging on a certain set of lattice planes with certain distances d_{hkl}, the angles, under which the diffraction peaks occur, are fully determined. Thus, because every crystal structure of a certain material has individual lattice planes, the position of peaks in a diffraction pattern, presenting the intensity measured in dependence on the diffraction angle, allows to determine the included crystalline phases. If the positions of the diffraction peaks are determined from measurements, the distances of the lattice planes can be determined for known incident wavelength. This allows to determine the length of the lattice axis. The general formula for the correlation between the plane spacings d_{hkl} and the lattice constants can be found in [95]. There, also the simplified equations for certain types of lattice symmetries are presented.

From the line positions of the XRD patterns, the crystalline phases can be determined. The relative amount of included crystalline phases can also be quantified, see for example [2]. Theoretically simulated XRD patterns of the three TiO_2 and the three ZrO_2 phases are presented in Fig. 2.5 and 2.6 and show the strong dependency of the diffraction patterns on the different crystalline phases. The diffraction patterns were created with the Powder Cell software [96].

Next to the intensity and the position of the peak, also the peak width delivers information. It is determined by the crystallite size and its distribution, see for example [95, 97]. The crystallite size in the direction perpendicular to the lattice plane of the used diffraction peaks can be determined from diffraction patterns by using the Scherrer formula, given by [95]

$$B(2\theta) = \frac{k_s \lambda}{L \cos(\theta)}. \tag{2.26}$$

This formula is usually used to determine the crystallite sizes, although the coherent scattering domains, leading to the peak broadening, are not necessarily the crystallites. The factor k_s is related to the crystallite shape and has values close to unity. It does not have a great significance, and is set to 0.94 here in agreement with the literature [95].

The broadening of the diffraction peaks is not only due to effects corresponding to the crystallite sizes, but there is also a broadening B_{ap} due to the apparatus. This broadening must be subtracted from the measured broadening. For Gauß-shaped peaks, this can be done with the mathematical expression $B(2\theta) = \sqrt{(B_0(2\theta))^2 - (B_{ap}(2\theta))^2}$. Nevertheless, there are some factors which have to be regarded critically when using the Scherrer formula for the determination of the crystallite size of nanostructured materials. Maybe the most important point is that the formula does not take stress and strain into account, which is a very critical point for crystallite sizes in the nanoscale. The peak broadening depends not only on the particle size itself and the surface stress, but also on the particle size distribution [97]. The crystallite size is a volume-averaged value, with increasing particle size, the formula delivers more uncertain values in the nanorange [98].

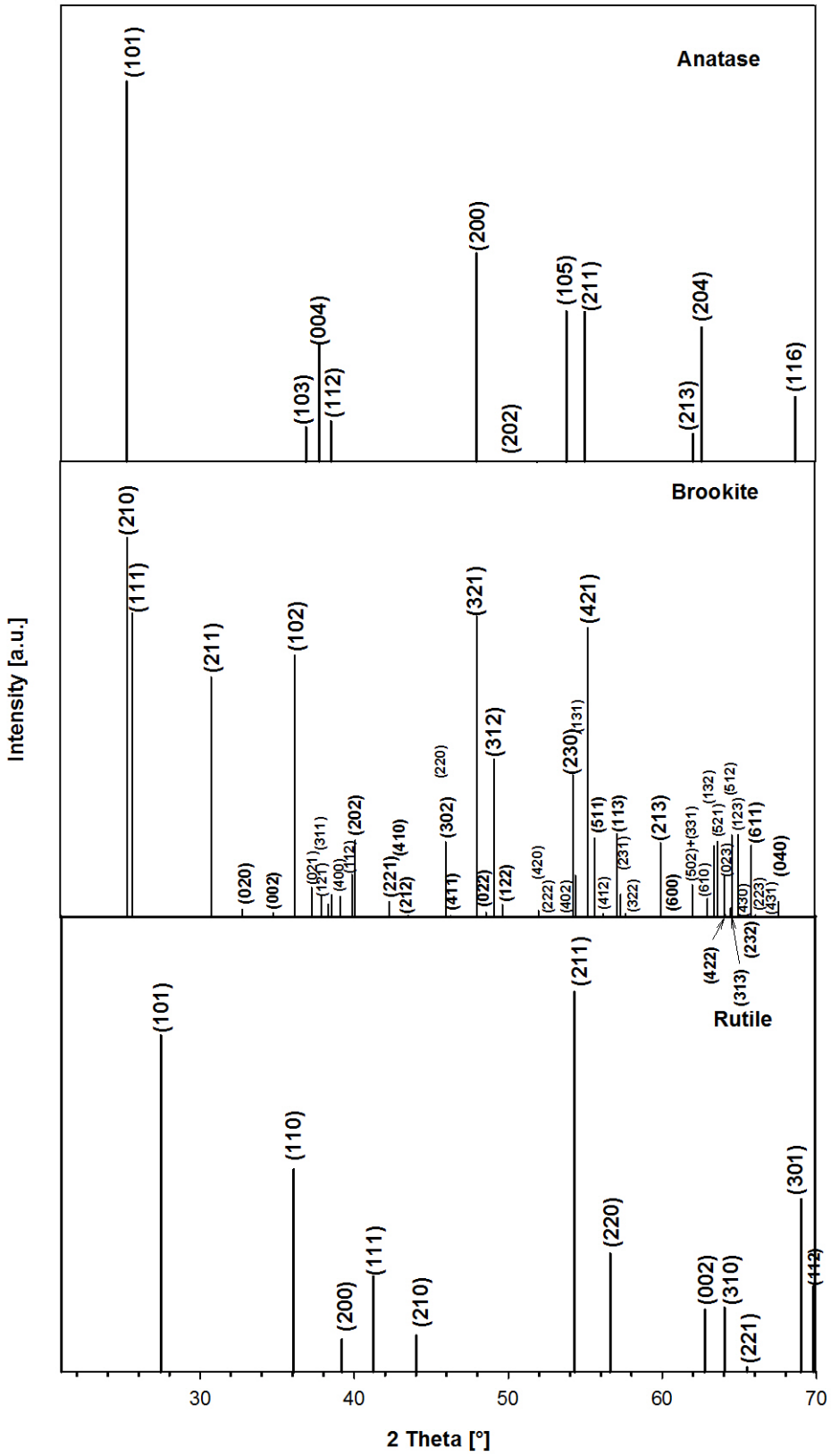

Figure 2.5: Simulated x-ray diffraction patterns of the TiO_2 polymorphs anatase, brookite and rutile. The patterns are calculated with the wavelength of copper K_α radiation, which is 1.54 Å.

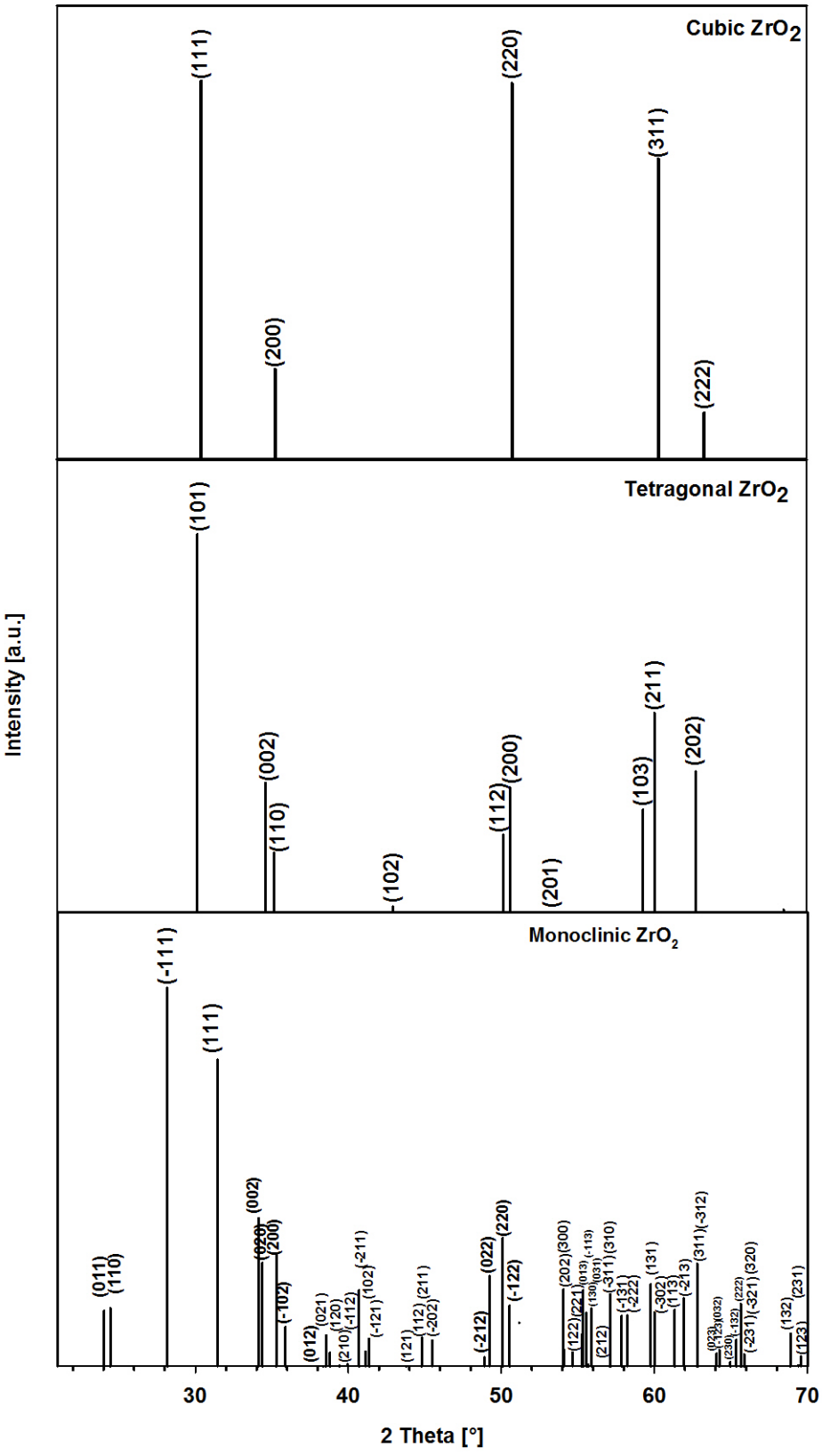

Figure 2.6: Simulated x-ray diffraction patterns of the cubic, tetragonal and monoclinic ZrO_2 polymorph. The patterns are calculated with the wavelength of copper K_α radiation, which is 1.54 Å.

2.5.3 Grazing-incidence small angle x-ray scattering (GISAXS)

This section gives a very rough summary of the GISAXS technique. Overviews of the theory can also be found in [99] and in the works of Müller-Buschbaum [100, 101].

Like XRD, small angle x-ray scattering (SAXS) is an elastic scattering phenomenon. The scattering of electromagnetic radiation at the electrons in the sample was described by structure factor and atomic form factor in section 2.5.2. In SAXS, the scattering at electron density fluctuations is regarded under small scattering angles. Instead of the wave vector $\vec{k}$ used in XRD, the scattering vector $\vec{Q}$ is used in SAXS. The scattering vector is defined as $\vec{Q} = \vec{k_f} - \vec{k_0}$, resulting in the magnitude of the scattering vector to be [102]

$$|\vec{Q}| = |\vec{k_i} - \vec{k_0}| = \frac{4\pi}{\lambda} sin(\Theta). \tag{2.27}$$

With the SAXS technique, structural characteristics like size, size distribution, shape and others can be determined. In this work, SAXS is used for structural investigations of solid particle sizes.

If the incident beam impinges on a film sample under a very small angle, which is or is close to the critical angle of the film material, the beam cannot longer penetrate the sample and the wave propagates at the sample surface. The important point with respect to the surface sensitivity is that the impinging beam is totally externally reflected [103]. This technique is then called grazing-incidence small angle x-ray scattering (GISAXS) and was introduced by Levine in 1989 to study the growth of thin gold films [103]. GISAXS can be regarded as a combination of different longer known techniques, namely small angle x-ray scattering (SAXS), grazing-incidence diffraction (GID) and x-ray reflectivity (XRR) [99]. From GISAXS data, it is possible to obtain information lateral as well as normal to the sample surface [99].

There are two important differences between transmission SAXS and GISAXS. First, the used beam has to be of small circular shaped cross section for GISAXS [101]. The second one is that instead of a single momentum transfer, the momentum transfer coordinates in x-, y- and z-direction are regarded separately. The momentum transfer coordinates are given by [100]

$$q_x = \frac{2\pi}{\lambda} \left[\cos(\Psi)\cos(\alpha_f) - \cos(\alpha_i)\right] \tag{2.28}$$

$$q_y = \frac{2\pi}{\lambda} \left[\sin(\Psi)\cos(\alpha_f)\right] \tag{2.29}$$

$$q_z = \frac{2\pi}{\lambda} \left[\sin(\alpha_i) + \sin(\alpha_f)\right], \tag{2.30}$$

where λ is the wavelength, α_i the angle between the incident beam and the film, α_f the angle between the sample plane and a regarded data point and Ψ the angle between the projection of α_f on the sample plane and the line of intersection of the scattering plane with the sample plane.

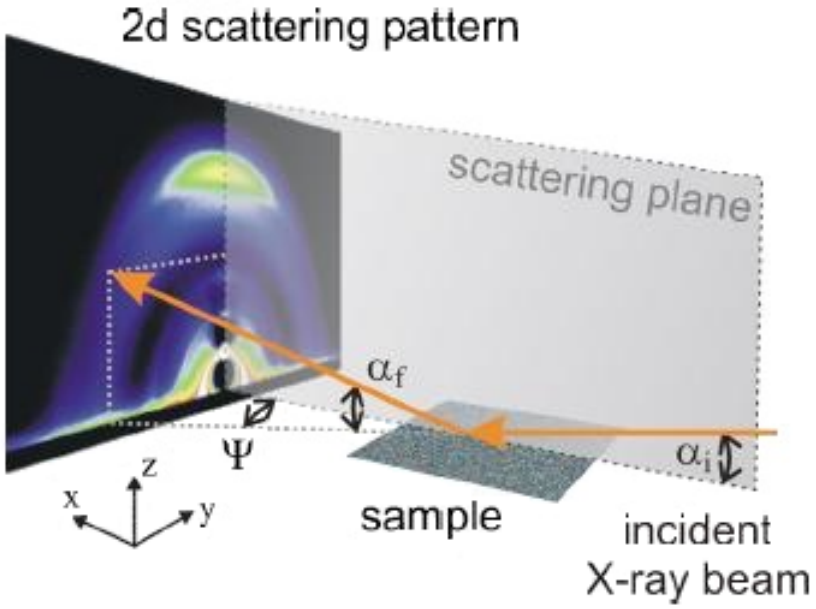

Figure 2.7: Geometry of GISAXS experiments at beamline BW4. Picture taken from [104].

A picture of the measurement geometry is presented in Fig. 2.7. The incidence angle is usually set near to the critical angle of the investigated material. By this choice of the incidence angle, signal from the sample surface regions is collected and the method becomes more surface sensitive.

The dependencies of the measured scattering signal on structural parameters are given by the structure factor. The form factor of a single particle is given by

$$F(\vec{Q}) = \frac{1}{V_p} \int_{V_p} \exp(i\vec{Q}\vec{r}) dV_p, \tag{2.31}$$

where V_p is the volume of the particle. The intensity of the scattered signal is proportional to the square of the form factor. The integral of the form factor cannot be solved analytically in many cases. For spherical particles, this is possible and leads to the equation [102]

$$\begin{aligned} F(Q) = & \\ & = \frac{1}{V_p} \int_0^R \int_0^{2\pi} \int_0^{\pi} \exp(iQrcos(\theta)) r^2 \sin(\theta) d\theta d\phi dr \\ & = \frac{1}{V_p} \int_0^R 4\pi \frac{sin(Qr)}{Qr} r^2 dr \\ & = 3 \left[\frac{sin(QR) - QRcos(QR)}{Q^3 R^3} \right] \equiv \frac{3J_1(QR)}{QR}. \end{aligned} \tag{2.32}$$

In this equation, $J_1(QR)$ is the Bessel function of the first kind and R is the sphere radius.

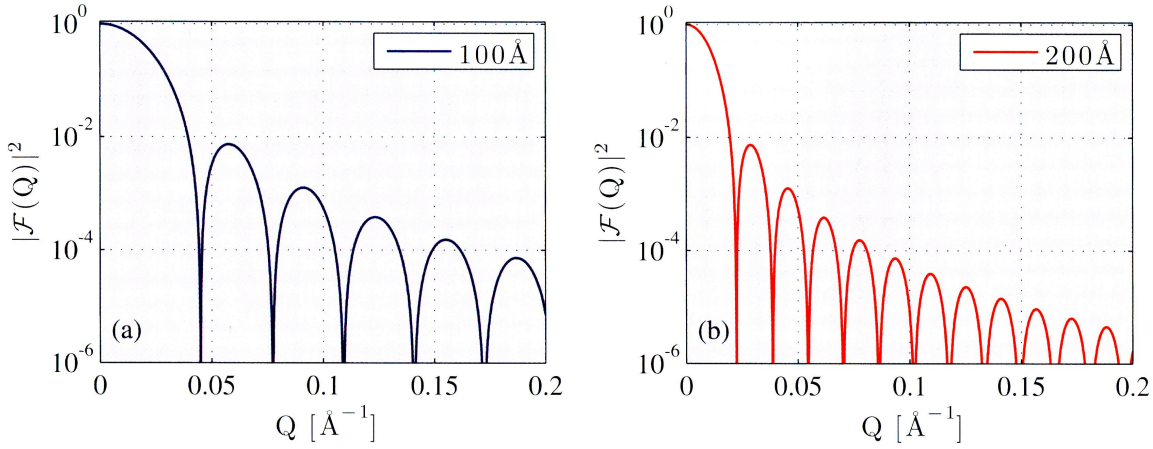

Figure 2.8: X-ray scattering curves of spherical particles with different radii. Pictures taken from [102].

Fig. 2.8 presents scattering curves for spherical particles with different particle sizes. As it shows up, the minima of the scattering curves shift to smaller Q values with increasing particle size.

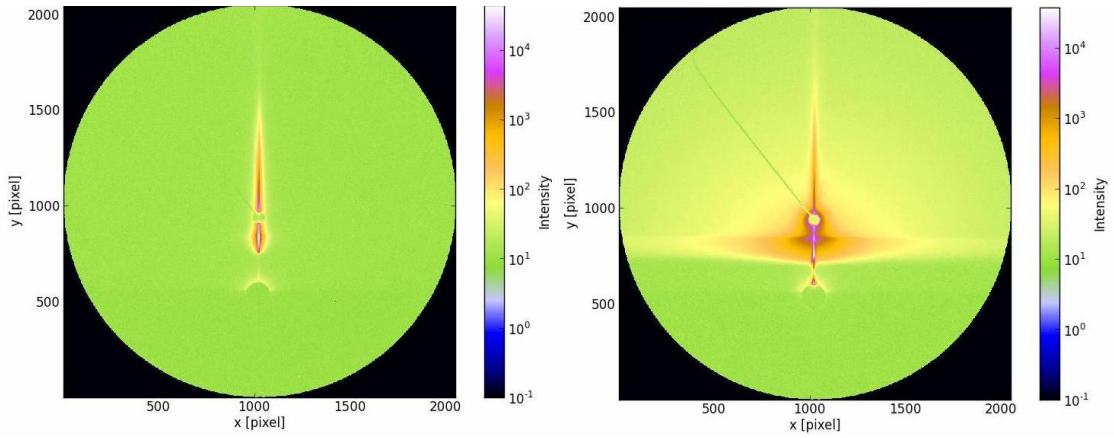

Figure 2.9: GISAXS images taken with the MarCCD 165 detector. The left side shows an image of an uncoated glass substrate, the right side presents the image of a composite sample prepared in 25 ml propanol alcohol dilution without annealing treatment.

Examples of GISAXS images of an uncoated glass substrate and a composite powder synthesized with propanol dilution made at beamline BW4 at HASYLAB, Hamburg are presented in Fig. 2.9. Beam stops cover the areas where the direct and the specular reflected beam would hit the detector. Another special point in the 2D scattering patterns is the Yoneda peak.

The differential cross section of the x-ray-sample interaction can be described in terms of the Fresnel transmission functions. At the Yoneda peak, these transmission functions are at their maximum [105]. The Yoneda peak occurs at a scattering angle of $\alpha_f+\alpha_c$ [99].

An important point is that the first minimum at Q_{min} in the intensity function delivers the particle size. It has the same condition for spherical, rod-shaped and disc-shaped particles. This condition is given by $\tan(Q_{min}R\text{-}1)=Q_{min}R$, which leads to the equation

$$Q_{min}R \approx 4.493. \tag{2.33}$$

From this equation, it is thus possible to calculate the size of the scattering structures [106]. It should be kept in mind that this equation only gives a rough approximation of the structure size, which certainly is dependent on the difference between the model assumptions and the real sample structure.

The scattering curves are derived from horizontal cuts from the measured 2D pictures. Such a cut is called an out-of-plane scan. The cuts were performed in the DPDAK software [107].

If the particles are not monodisperse, a function describing the particle size distribution modifies the intensity integral, which is in this case [102]

$$I(Q) \propto \int_0^\infty D(R)V_p(R)^2|F(Q,R)|^2dR. \tag{2.34}$$

Fig. 2.10 presents SAXS curves from particles with different size distributions. In this example, the size distribution is described by the Schultz function, given by [102]

$$D(R) = \left[\frac{z+1}{\bar{R}}\right]^{z+1} \frac{R^z}{\Gamma(z+1)} exp\left(-(z+1)\frac{R}{\bar{R}}\right). \tag{2.35}$$

In this equation, z is a variable measuring the spread of the particle sizes and $\bar{R}$ the average particle size. For $z \to \infty$, the particle size distribution tends to a delta function. The polydispersity p is given by $p=\frac{100}{(z+1)^{\frac{1}{2}}}$ in case of the Schulz function. With broader size distribution, the scattering maxima become broader and the minima much less pronounced.

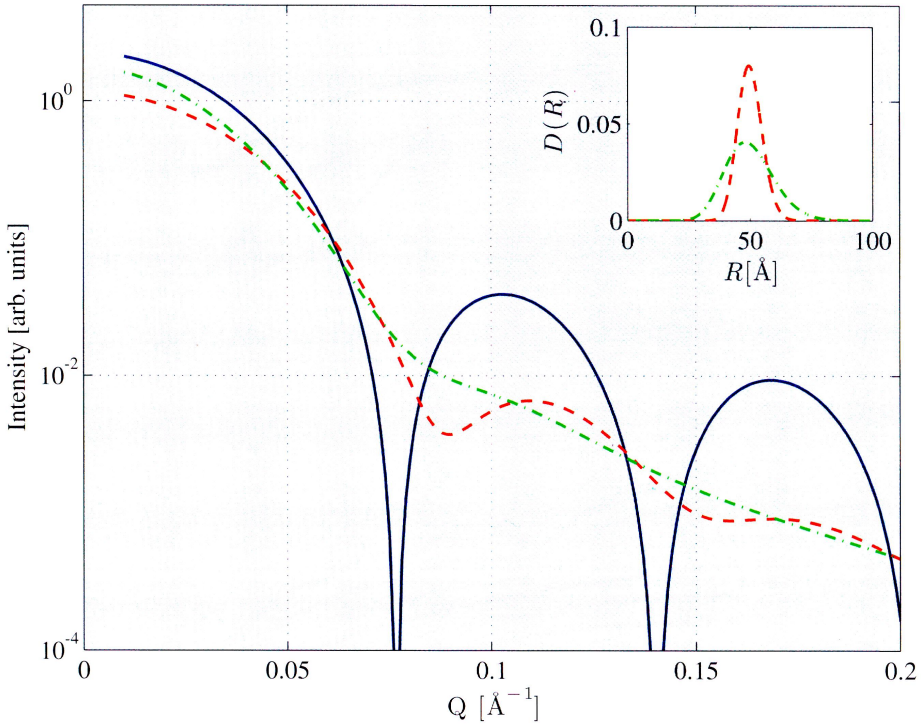

Figure 2.10: SAXS scattering curves in dependence on the particle size distribution. The solid, dark blue colored line is the scattering curve of a spherical particle of size R=50 Å. The dashed red line presents the form factor for spherical particles with an average particle size of $\bar{R}$=50 Å and a polydispersity p of 10% (z=99), the green line is the scattering curve for particles with $\bar{R}$=50 Å and a polydispersity of p=20% (z=24). The particle size distribution for the polydispersities of 10% and 20% are presented in the inset graph. Picture taken from [102].

2.5.4 Optical absorption spectroscopy

Optical absorption spectroscopy is used in this work for the investigation of the photocatalytic decomposition of methylene blue over the prepared titania and titania-zirconia composite powders. Similar to XAS measurements, the absorption of visible light is described by the Lambert-Beer law, which is here written as [108]

$$I(x) = I_0 \exp(-c\epsilon x), \tag{2.36}$$

where x is the thickness of the absorbing sample, c is the absorber concentration and ϵ is the molar extinction module. If this notation of the Lambert-Beer law is compared to Eq. 2.15, it can be found that μ=cϵ in this case. The most important point is that the absorption is dependent on the concentration of the absorber, thus optical absorption spectroscopy provides a method for the determination of c. If the absorber is decomposed into reaction products, which do not absorb in the same region of the visible light spectrum, the decrease in the absorber concentration can be determined from the decrease in the absorption signal.

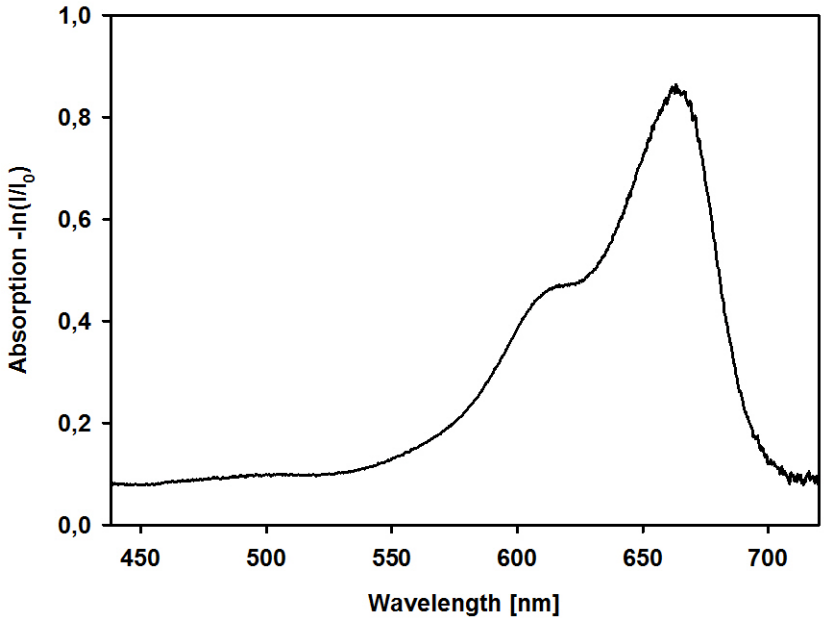

Figure 2.11: Optical absorption spectrum of a methylene blue solution.

An example of a methylene blue absorption spectrum is presented in Fig. 2.11. The measured aqueous methylene blue solution is that one used in the catalysis measurements and was measured before catalyst addition and irradiation.

2.5.5 Other used methods

X-ray photoelectron spectroscopy (XPS)

In section 2.5.1, it was already explained that the inner electrons of atoms can be excited to the continuum by irradiation of a sample with x-rays. If the energy of the photon, E=hν, is larger than the ionization energy, the electron will get the energy difference as kinetic energy. In XPS, the detected signal consists of the electrons ejected from the sample due to the ionization process [109]. If the electron energy is high enough and the ionized atom is close to the sample surface, the electron is able to leave the sample. The ionization energy is a result of the attractive potential of the atomic nucleus. In addition, the electron has to overcome the attractive potential of the solid to leave the sample and reach the detector. With these terms, the kinetic energy of the electron is E_{kin}=hν-E_b-Φ. From this, the binding energy can be determined from the measurement of the kinetic energy of the electron, by known work function Φ [109]

$$E_b = h\nu - E_{kin} - \Phi. \tag{2.37}$$

The term Φ is the work function given by E_{vac}-E_F=Φ [63], with the Fermi energy E_F and the vacuum energy E_{vac}.

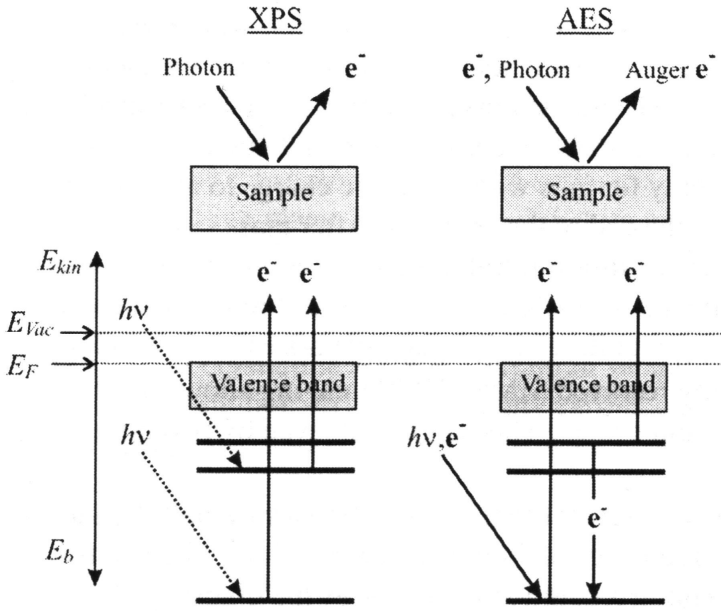

Figure 2.12: Energy levels and principal mechanism of XPS and Auger electron spectroscopy. Figure is part of a picture from [110].

The energy levels and the principal mechanism of XPS and Auger electron spectroscopy are depicted in Fig. 2.12. The more atoms of a certain species are included in the sample, the higher the possibility to collect photoelectrons from these species. The relative concentration c of a species X_i can be determined from the peak intensity $I(X_i)$, divided by the photoionization cross section $\sigma(X_i)$, both divided by the sum over the intensities of all included species [109]:

$$c(X) = \frac{I(X_i)/\sigma(X_i, E)}{\sum_i I(X_i)/\sigma(X_i, E)}. \tag{2.38}$$

This equation is only valid for homogeneous samples. The peak intensity is given by [109]

$$I = \int KT\sigma N(z) \exp\left(-\frac{z}{\lambda \cos(\theta)}\right) dz. \tag{2.39}$$

In this equation, K and T are instrument parameters, N(z) is the atom distribution in the depth z, λ is the electron mean free path and θ is the angle between the surface normal and the analyzer axis. The most important factor for chemical analysis is N(z). This factor shows that the peak intensity is dependent on the amount of a certain element species in the sample and its distribution in depth.

The photoionization cross sections can be looked up from tables, for example, with values calculated from single-potential Hartree-Slater atomic model by Scofield [111]. Due to the possibility of the determination of the chemical composition of samples, XPS is also called electron spectroscopy for chemical analysis (ESCA).

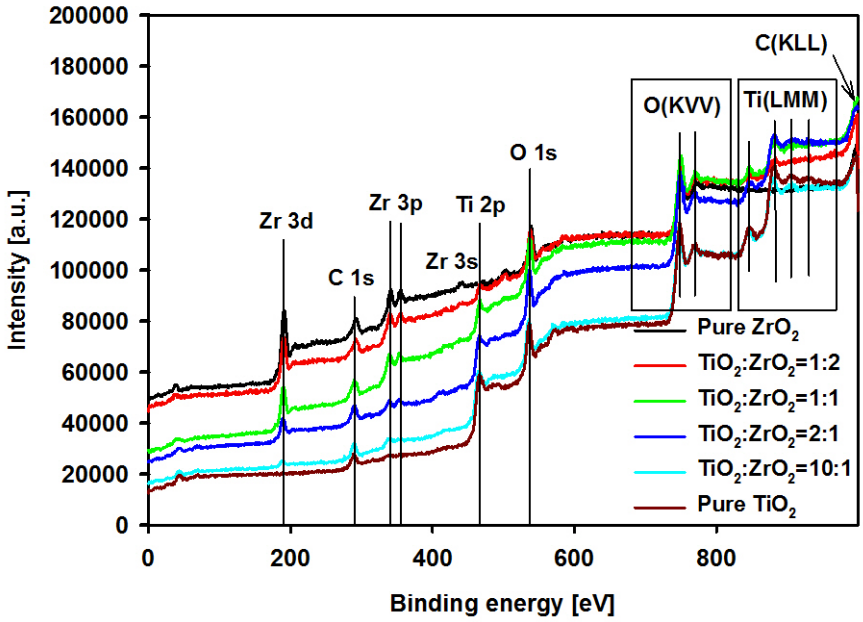

Figure 2.13: XPS spectra of pure oxides and composite samples prepared with alkoxide:water ratio of 1:4 without annealing.

Examples of XPS spectra are collected in Fig. 2.13 together with the assignments of the atomic orbitals the peaks are due to. In the higher energy regions, Auger peaks occur. Auger peaks are due to relaxation processes of the excited atom. Due to the absorption of x-rays, an electron is ejected from an inner shell of the absorber. An electron from an outer shell can fill the hole by energy release. Due to this energy release, an electron from a shell with lower energy than the shell of the refilling electron, the Auger electron, can leave the atom in the radiationless Auger process [112]. Next to the lines which origin is discussed above, photoelectrons of course can interact with the solid before leaving it, if the energy loss due to the interaction is small enough that the remaining energy is adequate for the electron to leave the sample, these electrons give the background of the spectra. For more details, the reader is referred to [113].

In the case of the binding energies of electrons bound to atoms in molecules, the binding energies of the electrons are shifted by values dependent on the difference in the electron affinity of the atoms in a certain bond. From the amount of the chemical shift, the type of chemical bond can be investigated, because the chemical shift is, for example, dependent on the electronegativity of the other elements in the molecule. Due to this, the photoelectron peaks are also shifted by some tens of electron volts to some electron volt. By fitting of the peak structure, the chemical environment of atomic species and the relative amounts of certain chemical environments can be determined [109].

Scanning electron microscopy (SEM)

In a scanning electron microscope, the sample surface is scanned by an electron beam. Only a short summary of the SEM technique is presented here, a detailed description can be found in [114]. The electrons are generated and accelerated in an electron gun.

The electrons are generated by heating of a cathode, field emission or, for example from LaB_6 crystals [114]. By the use of electron optics (magnetic lenses for example), the electron beam is accelerated and focussed and impinges on the sample surface. The electron beam can be scanned over the sample surface. There, different processes may occur, leading to the detected signals, in most cases like in this work, the signal contains of secondary electrons, which are electrons from the sample material ejected by impinging of the probe electrons. These secondary electrons are the most important signal contribution for the visualization of the surface structure of samples. Next to the secondary electrons, fractions of the signal are caused by backscattered electrons. They can be used to get information from deeper sample layers and for chemical analysis. By ejection of electrons from inner orbitals close to the nucleus, x-rays are generated by electron transitions from higher orbitals to the hole. Other processes might contribute to the signal, but are of minor importance [114]. These processes produce, for example, Auger electrons, characteristic x-rays and cathodoluminescence [114]. In this work, SEM is used to visualize the sample structure, thus secondary electrons are the most important signal source.

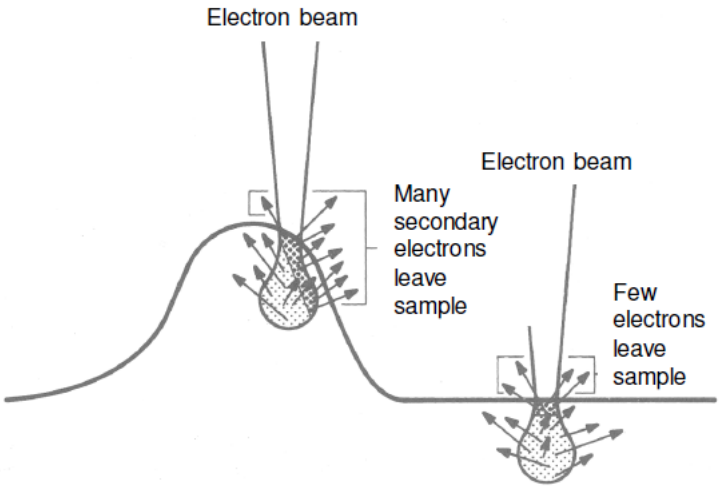

Figure 2.14: Interaction in the sample volume, causing the contrast of SEM. Picture taken from [114].

The contrast in SEM can be explained as follows: The electron beam impinges on the sample surface, the penetration depth is dependent on the electron energy. With Monte-Carlo simulations, it can be proved that the secondary electrons result from a volume in the shape of a pear, see Fig. 2.14. This volume of course has no sharp borders, but for simplicity, it can be assumed to have.

Due to the limited mean free path of particles in the material, only electrons which are generated near the sample surface can leave the sample. If the surface of the sample cuts the interaction volume horizontally, the sectional area of the interaction volume with the sample surface, where secondary electrons can leave the sample, is quite small, so there is only a small number of electrons which can be detected, and the surface presents dark in the SEM image.

On the other hand, if the sample surface is patterned with small structures, the sectional area is larger and more secondary electrons can leave the sample. In this case, the sample surface presents much brighter, compare Fig. 2.14. This contrast mechanism is that of highest importance for the measurements.

The backscattering electrons are not due to the ejection of electrons from the sample material, but are electrons from the impinging beam. Backscattering electrons are no secondary electrons. The strength of the backscattering is dependent on the chemical elements of the sample. Thus, areas with heavy elements are brighter in the SEM picture than those ones with light elements.

Another contributing effect is the charging of the sample due to the electron ejection. The field of the sample due to this charging influences the number of electrons leaving the sample.

The whole apparatus has to be kept under vacuum because the probes and signals are electrons, which would collide with gas atoms in normal atmosphere. This is always necessary if electrons should be detected, for example in the case of XPS. In case of scanning electron microscopes, the pressure requirement of 10^{-6} mbar is lower than that for XPS, which has to be 10^{-8} to 10^{-9} mbar.

2.6 Synchrotron radiation

X-rays are generated in two ways in this work: the first one is the generation in x-ray tubes, the second one implies the application of synchrotron radiation from storage rings. The radiation generation in synchrotron facilities is presented in the following description. Literature with detailed descriptions of x-ray physics, which are also used as references here, are for example 'Elements of modern x-ray physics' by J. Als-Nielsen and D. McMorrow [102] and the book of K. Wille [115]. The following brief description of the radiation generation in particle accelerators is written on the basis of [115, 102].

It is known from Maxwell's laws of electromagnetism that every accelerated charge emits electromagnetic waves. The emitted power P_s of a charged particle with a velocity v, which is much smaller than the speed of light, was calculated by to be

$$P_s = \frac{e^2}{6\pi\epsilon_0 m_0^2 c^3}\left(\frac{d\vec{p}}{dt}\right)^2. \tag{2.40}$$

Here, e is the electron charge, ϵ_0 the dielectric constant, t the time, $\vec{p}$ the momentum and m_0 the rest mass of the electron. The emission of radiation is important for charged particles in accelerators, where high energies are present. In this case, the equation above is no longer valid and by use of transformations of the time differential and the momentum differential in Lorentz invariant form, it is possible to calculate the emitted power of a relativistic particle from equation 2.41. For particles with velocities near the speed of light, v$\sim$c, the emitted power is

$$P_s = \frac{e^2 c}{6\pi\epsilon_0}\frac{1}{(m_0c^2)^2}\left[\left(\frac{d\vec{p}}{d\tau}\right)^2 - \frac{1}{c^2}\left(\frac{dE}{d\tau}\right)^2\right]. \tag{2.41}$$

The term τ is the relativistic time coordinate. From this equation, it is obvious that the emitted power increases with decreasing particle mass m_0. For this reason, electrons or positrons are used for the generation of synchrotron radiation instead of heavier particles like protons. Electrons are easy to generate as an additional advantage.

From equation 2.41 it is evident that longitudinal accelerations only yields a very small amount of radiation. Thus, synchrotron radiation sources are usually ring accelerators to introduce an acceleration component vertical to the direction of electron movement. For the emitted power of a circular movement, one gets

$$P_s = \frac{e^2 c}{6\pi\epsilon_0 (m_0 c^2)^4} \cdot \frac{E^4}{R^2}. \tag{2.42}$$

As it shows up, the emitted power is inverse proportional to the fourth power of the particle mass. If electrons and protons are compared at the same energy and at the same radius of movement R, the result is that the ratio of the emitted power is $1.14{\cdot}10^{13}$.

The first synchrotron radiation sources were particle accelerators used in high energy physics, which were used in a parasitic way for synchrotron radiation experiments. These sources were called first generation sources. The sources of the second generation were built only for the synchrotron radiation applications and used bending magnets (for example LURE, DORIS III). In third generation synchrotron sources (for example ESRF, APS), wigglers and undulators are used as insertion devices. Just for the completeness of this presentation, it should be mentioned that today there is also a fourth generation of synchrotron sources (for example XFEL) of rising importance, which are the free electron lasers (FELs). These sources are not used for the described investigations.

Another point making synchrotron radiation very interesting is the angle distribution of the emitted radiation. It is not the one of a Hertzian dipole, as it would be for non-relativistic particles. For highly relativistic particles, the opening angle of the emitted radiation beam is $tan(\Theta) = \frac{1}{\gamma}$, with $\gamma = \frac{E}{m_0 c^2} = \frac{1}{\sqrt{1-\beta^2}}$. For the high energies necessary to get significant emitted radiation and the small mass for electrons or positrons, γ becomes large and thus $\frac{1}{\gamma}$ is small and the opening angle is very small leading to the approximation $tan(\Theta) \sim \Theta$, and thus the opening angle is

$$\Theta \sim \frac{1}{\gamma}. \tag{2.43}$$

The radiation of relativistic particles is thus emitted in the form of a narrow cone. For the energy of the DELTA storage ring with an electron energy of 1.5 GeV, the opening angle for the wiggler (K=36) in symmetrical mode is 13 mrad [116] and that one of the DORIS storage ring is $K{\cdot}1.46{\cdot}10^{-4}$ rad. These values are the horizontal opening angles for wiggler radiation, compare Fig. 2.15. The parameter K is explained in more detail later.

In synchrotron facilities, the electrons or positrons make their way through the accelerator in groups, called 'bunches'. In a usual beamtime, between 2 and 5 bunches were used in the DORIS III facility at HASYLAB, Hamburg [117]. The formation of bunches is a result of the acceleration steps, the electrons or positrons go through: The first step is the acceleration to energies of a few hundred keV and then, they are accelerated in a linear accelerator consisting of cavities. In these cavities, there is a time dependent electric field, which accelerates the charged particles. Because the strength of this field changes with time, there are periodical field orientations leading to the maximum particle acceleration. To use this strength efficiently, the particles must be packed in bunches [118]. Every time a bunch passes an observation point, a short radiation pulse can be detected. The pulsed nature of the radiation can be used for some kinds of experiments, in which excited states are generated to examine their decay, so called pump-probe experiments.

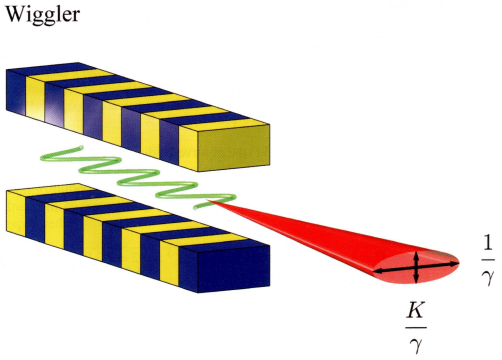

Figure 2.15: Construction of wiggler devices. Also presented are the dependencies of the horizontal and vertical beam cross sections on the opening angle and the undulator-parameter. Picture taken from [102].

A schematic presentation of a wiggler device is shown in Fig. 2.15 together with the x-ray beam divergences. Two alternating arrays of magnetic poles are constructed one upon the other in a way that a north pole is above a south pole and vice versa.

The difference between wigglers and undulators is the maximum angle of the particle path in the magnets. To characterize this angle, a magnitude called wiggler- or undulator- parameter is introduced, defined by

$$K = \frac{\lambda_u e \widetilde{B}}{2\pi m_e c}, \tag{2.44}$$

where λ_u is the periodic length of the magnet arrangement and $\widetilde{B}$ is the magnetic field in the magnet arrangement. The connection between the wiggler/undulator- parameter and the particle path angle is defined by $\Theta_w = \frac{K}{\gamma}$. The definitions for magnetic arrangements are then

$$Magnet = \begin{cases} Undulator : K \leq 1 \Rightarrow \Theta_w \leq \frac{1}{\gamma} \\ Wiggler \quad : K > 1 \Rightarrow \Theta_w > \frac{1}{\gamma}. \end{cases} \tag{2.45}$$

The opening angle of the undulator radiation is very small, while the radiation emitted by wigglers has a broader distribution. Undulators are especially used in diffraction experiments, while wigglers are usually used for XAFS measurements.

3 Experimental

3.1 Sample preparation

The samples were all prepared via sol-gel processes in ambient conditions. As alkoxide precursors, titanium tetraisopropoxide ($Ti(OC_3H_7)_4$, TTIP, ChemPur) and zirconium n-propoxide ($Zr(OC_3H_7)_4$, ZNP, ChemPur, 70% solution in propanol) were used. Samples have been prepared with the following changes in the synthesis parameters: TiO_2:ZrO_2 ratio, dilution of the reaction environment with n-propanol (C_3H_7OH), differences in the alkoxide:H_2O ratio, different aqueous electrolyte solutions, different amounts of added hydrochloric acid and different reaction temperatures. Details of the different preparations can be found in the following subsections. Generally, the amount of used alkoxide has been 40 mmol. In the case of composite samples, the fractions of the two alkoxides were chosen in a way that leads to the desired TiO_2:ZrO_2 ratios. To start the hydrolysis reaction, de-ionized water or aqueous electrolyte solutions were added. All samples were dried at room temperature between two sheets of filter paper for about 14-60 hours. Freshly prepared samples were found to be x-ray amorphous in all cases. To achieve crystallization of the samples, they were annealed in an industrial furnace in air at ambient pressure for four hours at temperatures of 350°C, 400°C, 450°C and 500°C. The heating rate was 10°C/min.

The two liquid alkoxides were mixed with a magnetic stirrer to lead to TiO_2:ZrO_2 ratios of 1:2, 1:1, 2:1, 4:1, 6:1, 8:1, 10:1, 15:1, 20:1 and 25:1. Pure TiO_2 and ZrO_2 powders have been prepared in the same manner to compare the results to those of the composites.

Pure titania and TiO_2-ZrO_2 composite samples were prepared with different reaction paths. The samples prepared in diluted reaction media were prepared by the addition of 5 ml, 15 ml and 25 ml n-propanol to the alkoxide mixture on a magnetic stirrer before the addition of water. The alkoxide to water ratio was again set to 1:4.

The samples prepared with different alkoxide to water ratios were prepared by the addition of 80 mmol, 320 mmol and 800 mmol of water to the alkoxide mixtures or the pure TTIP.

For the variation of the reaction environment by electrolytes, 1 M hydrochloric acid (HCl), 1 M sodium hydroxide (NaOH) and 1 M potassium hydroxide (KOH) were used instead of pure water with a ratio of alkoxide:electrolyte=1:4. In the case of HCl, composite and pure samples were also synthesized with alkoxide:HCl ratios of 1:2 and 1:8.

Six samples were prepared at different reaction temperatures, namely three samples of pure titania and three samples of TiO_2:ZrO_2=20:1, each prepared at reaction temperatures of T_{react}=50°C, 75°C and 100°C. The water for the hydrolysis reaction was heated on a heat plate, the alkoxide liquids were at room temperature when added to the heated water. In [54], it was shown for pure titania samples that this approach leads to results comparable with those ones in the literature, where both reagents are heated up. The resulting powders were dried and heat treated as all other samples.

Coatings for GISAXS measurements were prepared by the grounding of about 20 mg of dried amorphous powder in a mortar and the dissolving of this powder in some ml acetone. The mixtures of acetone and the powders were dropped on float glass substrates with a pipette. Two powders, namely pure titania and composite powder with TiO_2:ZrO_2=20:1, prepared via dip-coating by dilution of the alkoxides with 5 ml propanol were coated on substrates in their as prepared states without any heat treatment and annealed as thin films. This mixture was stirred with 450 rotations/min on a magnetic stirrer plate for three hours. Substrates were dip-coated in the solution and withdrawn with a Fischer-motor with a withdraw velocity of 5 mm/min.

3.2 X-ray absorption experiments

X-ray absorption experiments were performed in transmission mode. For these measurements, the powder samples were grounded in a mortar and mixed with polyethylene (PE) powder for dilution. The resulting powder mixtures were pressed to pellets of about 13 mm diameter and less than 5 mm thickness by application of about three tons weight with a mechanical press. The pellets were then put between two adhesion tape stripes (Scotch tape, which is nearly free of transition metal compounds [82]).

The experiments were performed at the beamlines A1 and C [119] at the DORIS III storage ring at the Hamburg synchrotron radiation laboratory (HASYLAB) at Hamburg, Germany and at the beamline 8 [120] at the DELTA storage ring in Dortmund, Germany. Positrons are accelerated up to energies of 4.45 GeV in the DORIS storage ring and electrons are accelerated up to 1.5 GeV in the DELTA storage ring. The positrons are concentrated in five bunches and the initial beam current is 140 mA at the DORIS facility. For measurements at the Ti K edge, Si(111) monochromators were used at all beamlines, only for a few measurements of the Zr K edge of the samples with TiO_2:ZrO_2=1:2, 1:1, 2:1, 10:1 and pure ZrO_2, a Si(311) monochromator at beamline C at the DORIS facility was used. For the measurements at the Ti K edge, the whole beamline set-up was evacuated at the DORIS storage ring to avoid parasitic absorption in air, comparable efforts were not possible at the beamline 8 at DELTA. There, the whole set-up was built up with distances between the different components (ionization chambers) as small as possible to keep the parasitic absorption as low as possible. To suppress higher harmonics from the monochromator, it was detuned to 50-60% of the maximum intensity.

Radiation was detected by gas-filled ionization chambers. At all beamlines, the first chamber was filled with nitrogen, and the second and third ones with argon. The gas pressures were chosen in a way that leads to an absorption of about 10% of the incident beam intensity in the first chamber and 90% in the second and third ones.

The PCA and LC-XANES analysis were performed using the WinXAS software [121]. The data first had to be energy calibrated, then the pre-edge background was subtracted from the Ti K-edges by a Victoreen-polynomial [122]. In case of the Zr K-edges, a linear polynomial was found to be a more suitable choice for the background subtraction. After these steps, all XANES spectra of powders annealed at the four used temperatures and belonging to a certain sample type (TiO_2:ZrO_2 ratio, chemical reaction environment) were taken as a data set for principal component analysis. The spectra of the powders which were not annealed were taken as the amorphous TiO_2 references. The reference samples which were determined by PCA to be appropriate for the sample set were then used in the LC-XANES fits.

For the pre-edge peak fitting, the data were first handled in the Athena software of the IFEFFIT package [123] to calibrate the energy, subtract the background and normalize the data. The peak fitting itself was made in the Fityk software [124]. Gauß-peaks were used for the fitting of the XANES region.

3.3 X-ray diffraction experiments

The XRD measurements were all made with laboratory equipment. A Phillips X'Pert Pro multi-purpose diffractometer was used. The measurements were performed in Bragg-Brentano geometry with Cu K_α radiation in an angle range between about 21° and 70°. In the incident beam optics, a 10 mm mask is used together with a 0.04 rad Soller-slit and a divergence slit. The incident beam impinged on a small amount of powder mounted on a zero-background holder, which was spun horizontally for better sample statistics. The diffracted beam path consisted of a 0.02 rad Soller-slit and an anti-scatter slit (opening angle 4°), next to a 0.02 mm nickel filter to suppress the Cu K_β line.

The determination of the included crystalline phases was performed by comparison of the positions of the occurring diffraction lines with theoretically calculated patterns, which were simulated in the Powder Cell software [96]. To determine the average particle size from the diffraction data, the most intense reflex of a crystalline phase was fitted with a Gauß-shaped peak to determine the peak broadening. This was used for calculation of the crystallite size via the Scherrer-formula (Eq. 2.26).

3.4 X-ray photoemission spectroscopy experiments

X-ray photoelectron spectroscopy measurements are performed on all samples prepared with aqueous electrolyte solution medium.

The x-ray photoemission spectroscopy measurements were performed with an ESCALAB5 spectrometer. The spectrometer consists of three evacuated chambers, namely the pre-chamber, the preparation chamber, which is used only for gating of the samples in this work, and the analysis chamber with the x-ray tube, the entrance of the analyzer and sources for other kinds of probes (for example an ion gun and a UV source). The x-rays generated in the tube impinge on the sample surface and electrons are ejected due to the mechanisms presented in section 2.5.5. The ejected electrons are accelerated to the analyzer by electrostatic transfer lenses. In this work, the energy analyzer is operated in the constant analyzer energy (CAE) mode. This means that the voltage over the analyzer hemispheres is set to a constant value, allowing electrons of a certain energy to reach the channeltron. This very short overview over the working principle is written according to [109]. There, a more detailed description can be found.

The x-rays generated in the tube impinge on the sample surface, where the generated photoelectrons leave the sample. These are accelerated to the detector.

The sample preparation for these measurements consisted of the grounding of the powders in a mortar, to alleviate the transport of the charges generated in the photoionization processes during the measurements. To ensure the charge transport away from the sample, the powders were pressed on copper sample holders with conducting adhesion tape.

The samples had to be introduced into the spectrometer through a pre-chamber and a preparation chamber. The samples were first stored in the analysis chamber overnight to allow them to degas from the air components which adsorbed to the large particle surface. The measurements were performed at pressures between about $5{\cdot}10^{-9}$ and $5{\cdot}10^{-8}$ mbar. The sample surfaces were slanted by an angle that allowed the electrons ejected from the sample to enter the analyzer vertically. The current at the x-ray tube was set to 20 mA, the voltage was 10 kV. Magnesium was used as anode material (E=1253.6 eV).

First, a survey scan between 0 and 1100 eV was performed of each sample at a pass energy of 200 eV and a step width of 0.7 eV. Three scans were taken and averaged. After this scan, detailed scans were performed around the energy regions of the theoretical binding energies of each species included in the sample. Scans of titanium 2p (E_b=475 eV), carbon 1s (E_b=285 eV) and oxygen 1s (E_b=530 eV) were always made, in case of composite samples, also the binding energy region of zirconium 3d (E_b=185 eV) is scanned. Powders prepared in electrolytes were investigated with respect to contaminations by electrolyte ions, namely chlorine 2p (E_b=198 eV), sodium 1s (E_b=1072 eV) and potassium 2p (E_b=230 eV). These detailed scans were collected at a pass energy of 20 eV and a step width of 0.05 eV. The number of scans to be averaged were chosen in dependence on the peak intensities to achieve a good signal to noise ratio.

The data were handled in the Fityk software [124] to remove the background and to fit the measured data by Gauß-functions.

3.5 Grazing incidence small angle x-ray scattering experiments

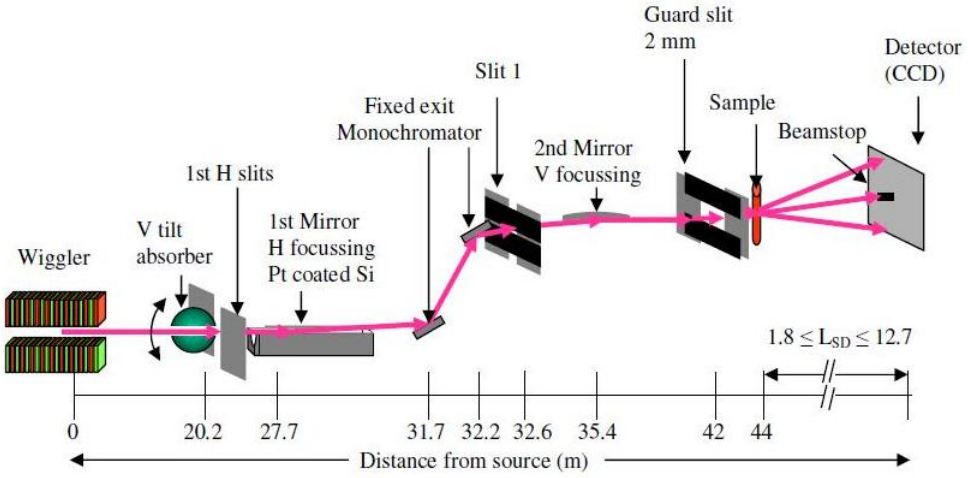

Figure 3.1: Set-up of the x-ray scattering beamline BW 4 at DORIS III (HASYLAB, Hamburg, Germany) from the insertion device (Wiggler) to the detector (MarCCD 165). The abbreviation L_{SD} stands for the sample-detector distance. Picture taken from [125].

GISAXS measurements were executed at the beamline BW4 at the DORIS III storage ring [125]. A technical picture of the beamline set-up is shown in Fig. 3.1. The beam comes from a wiggler source and passes an absorber and a first slit, is then focused horizontally by an x-ray mirror and passes a Si(111) monochromator, where a wavelength of λ=1.381 Å is selected from the white beam. The monochromatic beam then passes

a slit, is focussed vertically by a second x-ray mirror and then passes a further slit, before impinging on the samples, which are thin films in this work. From the wiggler exit to the detector, the whole beamline has a total length of 56 m. For the detection of the scattered beam, a MarCCD 165 detector was used. The active detector area has a diameter of 165 mm, which is reduced to the 2048×2048 pixels, each of size 79.1 μm, by a taped glass fiber [126]. More details about the beamline can be found in Ref. [126].

The samples were mounted on a table with a sample to detector distance of 2.31 m. The angle between the incident beam direction and the sample surface was about 0.4°. Slight deviations from this value has sometimes been used to coincide the passed synchrotron beam and the beam stop, to avoid saturation of the detector. The data acquisition was performed with an exposure time of 10 min. The whole data sampling time was 20 minutes, because two pictures were taken and then averaged by the data acquisition software. This leads to a better signal to noise ratio.

3.6 Photocatalytic measurements

For the investigation of the photocatalytic efficiency of the samples, (10 ± 0.5) mg of some of them were added to an aqueous methylene blue solution. The solutions were prepared from an initial solution made from 160 mg methylene blue powder (Carl Roth) and 250 ml deionized water. This leads to a very dark blue solution, which is not clear and thus not suitable for optical absorption measurements. One drop of this solution is added to 25 ml deionized water for dilution. To have a constant sample thickness, the solutions and the catalysts are put into disposable plastic cuvettes (PLASTIBRAND®, Carl Roth) with a UV/Vis window of 220-900 nm. The sample thickness was 10 mm.

The samples were irradiated with UV radiation under a UV exposure unit (Isel UV-Belichtungsgerät 2). The emitted wavelength is 365 nm. The distance between the glass plate of the UV exposure unit and the sample table was 8 cm. The UV exposure unit had four tubular fluorescent lamps, each with 15 W power. The samples were irradiated for 10 minutes and measured, then irradiated again and so forth. Some of the samples with fast reaction rates were irradiated with 2 min. time period.

Optical absorption measurements were performed on an Ocean Optics HR4000 spectrometer [127]. The incoming radiation is focussed by a glass lens and lead through a glass fiber. In the spectrometer, a Czerny-Turner set-up is used for the wavelength specific light analysis. The light is detected by a linear CCD array (Toshiba TCD1304AP). The CCD consists of 3648 Pixels with a size of 8 μm × 200 μm [127]. In the stated reference, more information about the spectrometer can be found. As a light source for the optical absorption measurements, 8 LEDs with total power of ca. 2.6 W from a torchlight were used, emitting radiation in a wavelength range from ca. 420 to 690 nm.

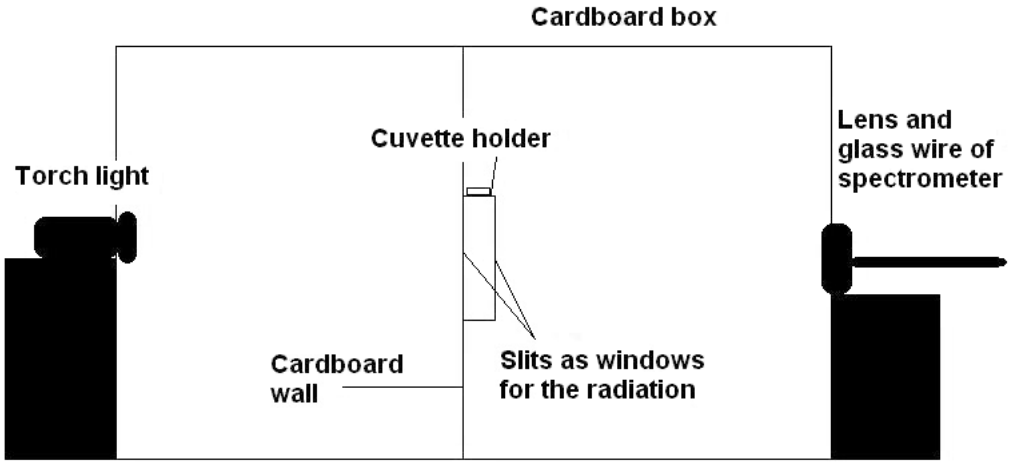

Figure 3.2: Schematic presentation of the experimental construction for the optical absorption measurements. The light passes through slits in the cardboard of the cuvette holder, which are not observable in this perspective.

The measurement set-up was put into a cardboard box to reduce background radiation. A schematic view is presented in Fig. 3.2. In the center of the box, a cardboard wall with a radiation entrance slit and a cuvette holder with a radiation exit slit in the middle of the wall was installed. On the other side of the box, face to face with the torchlight, the lens of the spectrometer was mounted.

The measurement time for one spectrum was 100 ms, for every measurement 10 spectra were averaged. For every new time measurement of the cuvettes, a new reference spectrum (measurement without sample in the beam path, determines I_0) and new dark spectrum (spectrum without light source, for the subtraction of radiation background due to the light environment) were measured.

For the analysis of the peak intensity, three Gaußian shaped peaks had to be fitted to the spectra. Two peaks were found to be unsuitable for a fit matching to the data with low deviation. The peak fits were performed after a background subtraction in the Fityk software. (Absorption background resulted from the absorption of the cuvette material and from catalyst particles solute in the methylene blue solution.)

The degradation of the methylene blue is calculated from the absorption spectra by [128]

$$Degradation[\%] = \frac{A_0 - A(t)}{A_0} \times 100, \tag{3.1}$$

where A_0=A(t=0) is the absorption of the methylene blue solution before irradiation and A(t) is the absorption after an irradiation time t. The absorption is determined from the peak area of the most intense peak at about 670 nm.

4 Investigation of sol-gel derived TiO_2-ZrO_2 and TiO_2 powders

The methods which were explained in the previous chapters will now be applied to the investigation of titania containing, nanostructured powders. The emphasis is the use of x-ray absorption spectroscopy to investigate the influence of the reaction parameters on the structure of the precipitates and their influence on the crystallization process during heat treatment. The results derived from the investigations on the composite samples will be compared to those of pure TiO_2 samples. Annealed samples are investigated with respect to the crystalline and amorphous phase concentration and the crystallite size with LC-XANES and XRD. The results are used to determine the titania to zirconia ratio which lead to the most suitable materials structure for catalytic applications. Samples with this ratio are prepared with different chemical reaction conditions. Pure titania samples are prepared in the same way for comparison. Samples prepared with electrolytes are examined with XPS to search for possible contaminations from the electrolytes. The agglomerated structure of some of the samples is examined with SEM and GISAXS. The combination of these techniques allows the determination of many of the characteristics important for nanostructured catalysts. Some of the samples are used as catalysts for the decomposition of methylene blue. The results are explained on the basis of the determined material structures.

4.1 Influence of the TiO_2:ZrO_2 ratio on the TiO_2 precipitate structure

First, the structure of the samples with different TiO_2:ZrO_2 ratios is investigated shortly after their preparation, without any further treatment. XRD provides information about the crystalline polymorphs and the crystallite sizes. The first structures in the as-synthesized powders might be important for further crystallization processes during the heat treatment and are examined by XRD and fitting of the XANES pre-edge. In none of the XRD patterns presented in Fig. 4.1, sharp diffraction lines are observable. Thus, for all TiO_2:ZrO_2 ratios, the as-prepared samples, which means the samples before the heat treatment, are x-ray amorphous, and thus a structural investigation by XRD is not possible.

The structure of the samples before the annealing process is investigated by pre-edge fitting of the Ti K-edge XANES region and EXAFS.

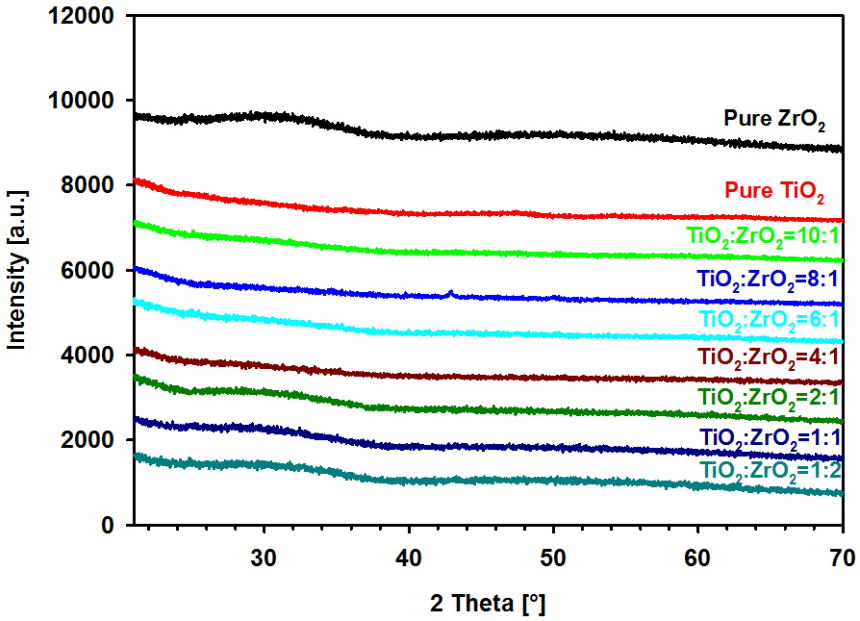

Figure 4.1: XRD patterns of powder samples with different TiO_2:ZrO_2 ratios without heat treatment. Patterns are shifted vertically with respect to each other by 1000 units for a better comparison.

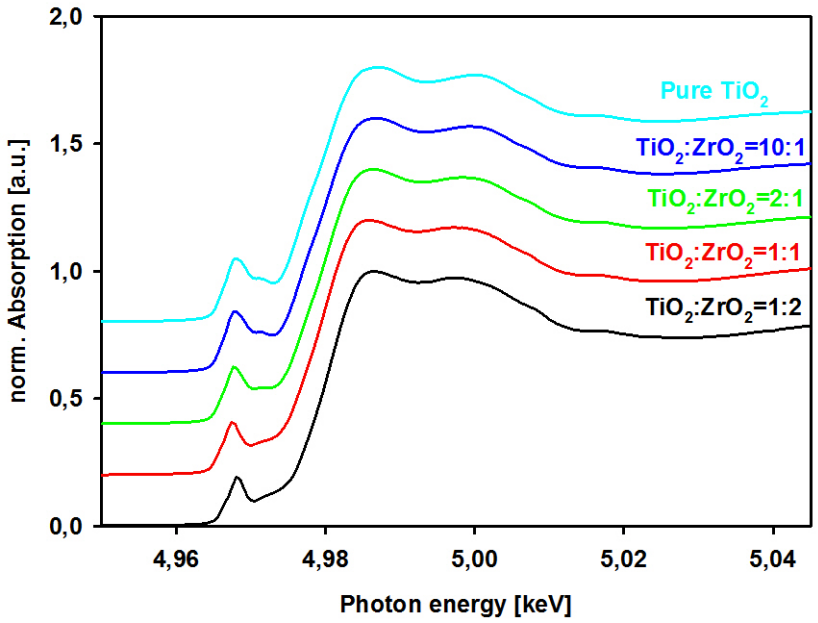

Figure 4.2: Ti K edges of amorphous composites and a pure titania sample. Spectra are shifted vertically with respect to each other by 0.2 units for more clarity.

The differences in the XANES structures of amorphous titania samples are usually very small, as can be seen in Fig. 4.2, so also LC-XANES fits are not possible. As was explained in the section about x-ray absorption spectroscopy, the pre-edge peak shapes of the Ti K-edge XANES are sensitive to the coordination of the titanium absorbers. The A2 peak is ascribed to five-fold coordinated titanium, the A3 peak to six-fold coordination, compare section 2.5.1. It was also explained before that titanium is six-fold coordinated in all three crystalline polymorphs, but that the coordination is reduced on the particle surface due to missing binding partners on surfaces. If now the crystalline nuclei formed in the precipitates are very small, the specific surfaces are very large and the coordination is reduced, thus the A2 peak intensity will increase. On the other side, the amount of titanium absorbers in the bulk of the clusters, which have a higher coordination, is reduced, which decreases the A3 peak intensity. Thus, the intensity ratio A3:A2 provides a qualitative statement on the size of the clusters. In the presented spectra, it also shows up that the B peak changes with changing oxide ratio. It becomes more pronounced with increasing titania content.

An example of a Ti XANES spectrum fit is presented in Fig. 4.3 a. This method was already presented in the literature for the investigation of pure titania samples, for example by Luca et al. [32]. To the best knowledge of the author, the method has not yet been applied to mixed oxide composite samples.

The A3:A2 peak intensity in dependence on the zirconia concentration in the samples is depicted in part b of Fig. 4.3. The intensity ratios tend to increase with decreasing amount of zirconia in the powders, as is shown by the dotted trend line. The two gray data points belong to the samples with TiO_2:ZrO_2=20:1 and 25:1. These do not match to the expected trend and were not taken into account in the determination of the trend line. The reason for this strange behavior is unknown. Thus, the size of the small ordered titania clusters built in the precipitates is larger for smaller zirconia amounts. Such a result is in agreement with the encapsulation theory of Elder et al. [1]. The more zirconium is incorporated in the samples, the smaller the encapsulated titania fractions, and thus the near range order can maximally be as large as a capsule. In the chemical reaction step, the first small particles with crystalline order are built up. In this reaction step the zirconium might built a layer during the reaction, zirconia precursors might react to ZrO_2 on the titania surface and thus no more titania can be adsorbed on the particle surface. From this point it might be assumed that the crystallite sizes after heat treatment will be larger for the samples with large TiO_2:ZrO_2 ratio.

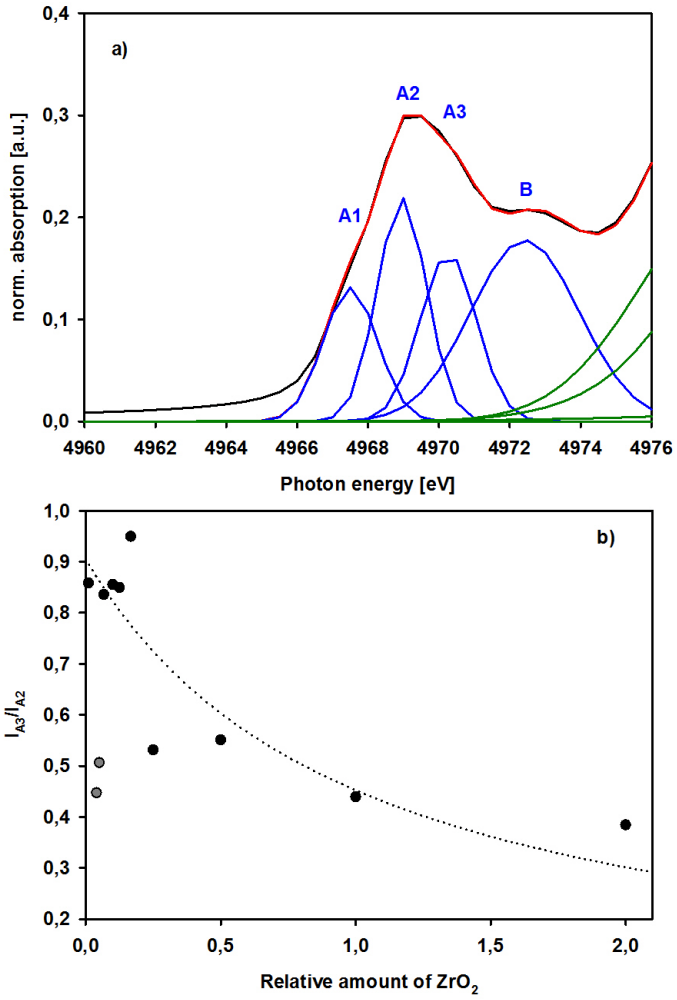

Figure 4.3: An example of the fitting of the XANES pre-edge region of a Ti K-edge spectrum of a sample with TiO_2:ZrO_2=25:1 is presented in part a, part b shows the I_{A3}:I_{A2} peak intensity ratios for the powders with different TiO_2:ZrO_2 ratios. The dotted line is a trend line just to guide the eye to the decreasing trend. The two gray data points do not match to the trend and were not taken into account in the determination of the trend line.

A proof of Ti-O-Zr bonds in the samples can be given by Fourier transformed EXAFS spectra. An example is presented in Fig. 4.4 b, showing the EXAFS data of samples with different TiO_2:ZrO_2 ratios. The samples were not annealed before the measurements. As can be seen, there is one peak in the higher coordination shells which increases with increasing zirconia amount. In the picture, this peak is marked by an arrow. A similar trend with increasing zirconia amount is observable in the $k\chi(k)$ spectra presented in part a. The higher amplitude of the oscillation is due to the higher amount of zirconia scatterers at a certain binding distance, as can be seen in the EXAFS formula, Eq. 2.19. It is also observable that the marked peak shifts to smaller binding length with increasing zirconia concentration. The peaks at the higher coordination shells are not strongly pronounced and at higher binding length, they are due to sine functions resulting from

the Fourier transformation. This is due to the amorphous character of the samples. There is no long range order in the samples, leading to statical disorder, resulting in a damping of the EXAFS amplitude, compare section 2.5.1.

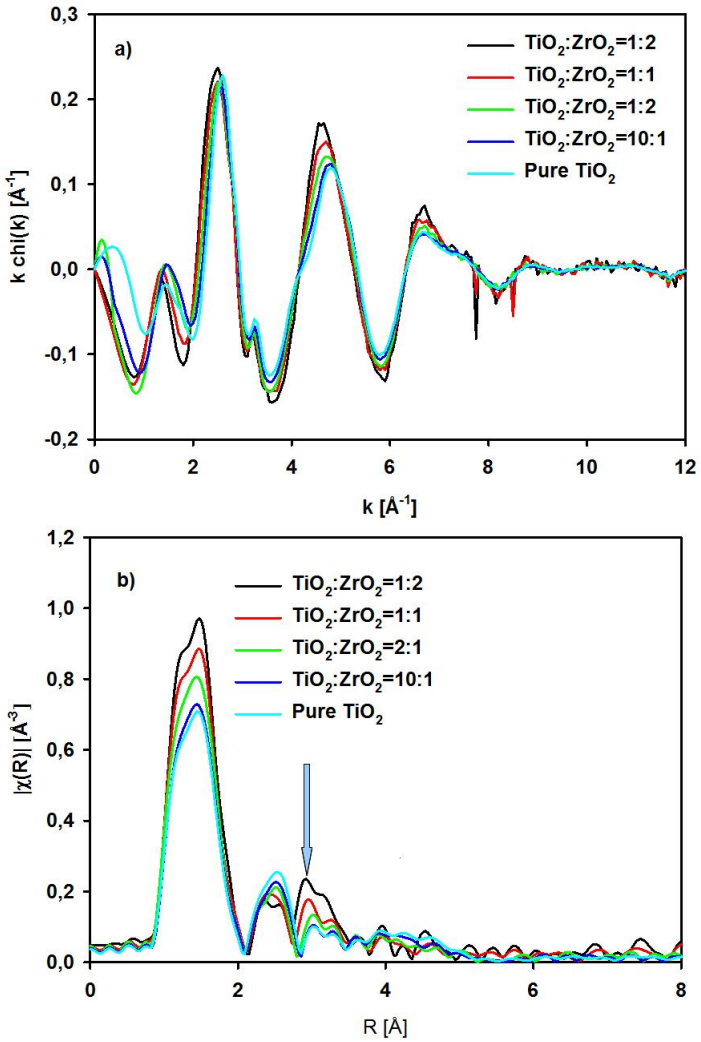

Figure 4.4: EXAFS plotted as kχ(k) spectra of samples with different TiO_2:ZrO_2 ratios and pure titania in part a. The same data plotted in R-space (k=2 weight) in part b. The samples were not annealed. The arrow shows to the peak which is due to the Ti-O-Zr bond.

4.2 Influence of the TiO_2:ZrO_2 ratio on the TiO_2 crystalline structure

In a first step, the influence of the TiO_2:ZrO_2 ratio should be investigated with respect to the anatase crystallization of the included titania. The important questions to answer are first, which oxide ratio leads to the highest anatase concentrations and second, how the particle size depends on the oxide ratio.

Another important point is if the oxides have only physical contact or if there are chemical bonds between the oxides. This is examined with XRD as well as XAFS spectroscopy.

Fig. 4.5 shows XANES spectra of samples with different TiO_2:ZrO_2 ratios after annealing at 500°C for four hours. The reference spectra of amorphous titania and anatase are presented for comparison.

What is obvious at first glance is that there is only a phase transition from the amorphous to the anatase phase if the TiO_2 concentration in the powders is much higher than that of ZrO_2. The larger the TiO_2 fraction in the material, the more pronounced are the absorption structures belonging to the anatase phase. The first obvious structural change in the XANES occurs for samples with TiO_2:ZrO_2=4:1. For larger zirconia concentrations, no crystallization of the TiO_2 fractions can be observed, which is also obvious in XRD measurements of the samples, which will be presented later in context with the discussion of the crystallite sizes.

A reason for the amorphous character of the samples might be that the fraction of pure O-Ti-O or O-Zr-O bonds with respect to Ti-O-Zr bonds is too small. From Ti-O-Zr bonds, $ZrTiO_4$ may be built at temperatures of T$\geq$ 650°C [12], which is substantially more than was applied in this work, explaining that this phase is not detectable in any of the samples. If the molar amounts of TTIP and ZNP are equal or nearly equal to each other, there are many Ti-O-Zr bonds, which are however not able to crystallize at the applied annealing temperatures, leading to the observed amorphous nature of the samples with TiO_2:ZrO_2=1:2, 1:1 and 2:1. If the amount of titania is larger, volumes of the samples are dominated by pure O-Ti-O bonds, which may crystallize at suitable annealing temperatures, because the amorphous-anatase phase transition of pure TiO_2 is somewhere between about 300-400°C for pure TiO_2 materials prepared via sol-gel processes [67]. An argument against the formation of amorphous zirconium titanate phase is the fact that from the shape of the measured XANES structures, there is no reason to assume any more phase than amorphous TiO_2 and anatase TiO_2, because all features can be assigned to titania.

Elder et al. [1] assumed that the stabilization of anatase crystallites in TiO_2-ZrO_2 composite powders is due to the encapsulation of TiO_2 fractions in an amorphous ZrO_2 matrix. Thus, they assumed a physical contact between TiO_2 and ZrO_2 instead of a chemical one. Nevertheless, it is difficult to explain the formation of $ZrTiO_4$ crystalline phase at higher annealing temperatures observed by other working groups, except it is assumed that a rearrangement of chemical bondings takes place during the annealing treatment at high temperatures. Before it was found that $ZrTiO_4$ can be prepared by sol-gel processes and annealing at T$\geq$ 650°C, it was prepared by solid state reactions between TiO_2 and ZrO_2 at annealing temperatures T > 1000°C [129].

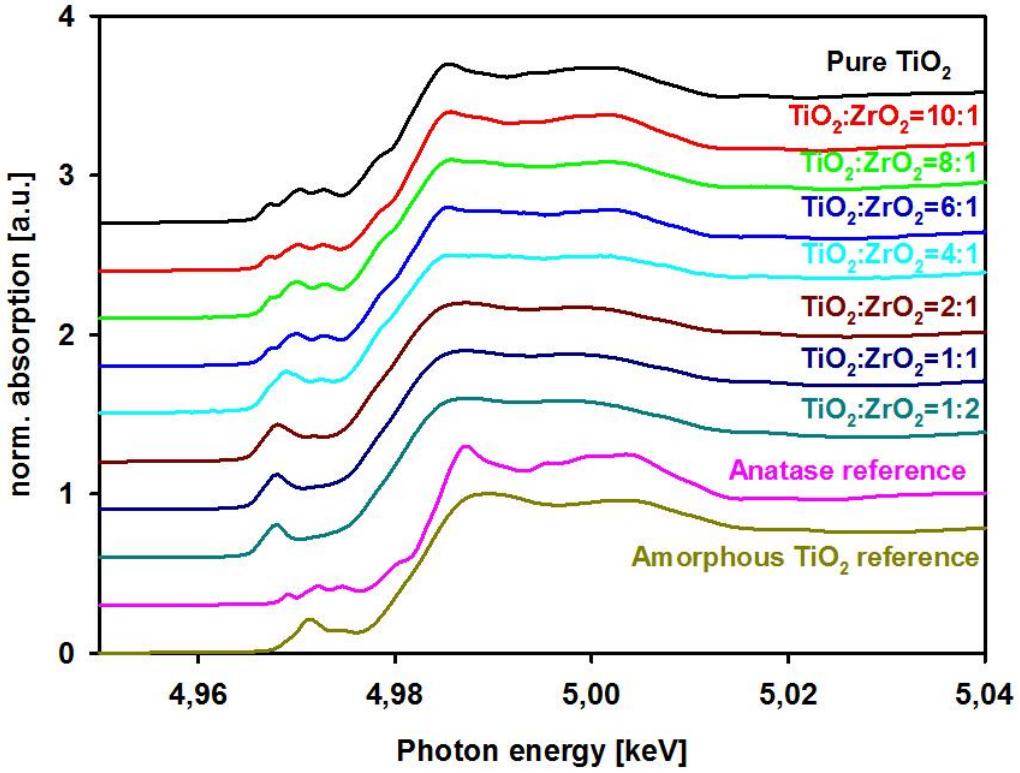

Figure 4.5: XANES spectra of powders composed of different TiO_2:ZrO_2 ratios and annealed at 500°C for four hours. Reference spectra of anatase and amorphous TiO_2 are presented for comparison. Spectra are shifted vertically with respect to each other by 0.3 units for a better comparison.

If the oxides are only in physical contact after sol-gel reaction of mixed alkoxides, there is no reason for the decrease of the formation temperature of $ZrTiO_4$. In a picture concerning chemical bondings like Ti-O-Zr, the formation of $ZrTiO_4$ can be explained easily. An encapsulation effect is nevertheless possible, the titania volume fractions may be encapsulated in a matrix of amorphous mixed oxide, remaining amorphous during annealing at T$\leq$ 500°C.

A question remaining is why the temperature of the phase transition from the amorphous TiO_2 phase to anatase changes with changing TiO_2:ZrO_2 ratio. The amorphous TiO_2 transforms to anatase when two amorphous particles are combined to a larger particle, which has to exceed a critical size for the phase transformation, see section 2.4. The anatase nucleus is then nucleated at the interface between the amorphous particles [67], needing energy for the rearrangement of atoms at the interface [67]. This phase transformation mechanism is similar to that of the anatase-brookite and anatase-rutile phase transformation [67]. For the critical radius of the titania particles for phase transformation, different values were found experimentally. The critical radius of phase transformations seems to be dependent on other factors like the free surface enthalpy, the annealing temperature or additives. The phase transformation temperature for the amorphous TiO_2-anatase transition may be influenced by changes in the area of the interface between the pure TiO_2 volumes and the Ti-O-Zr regions. The changes in the critical

particle size could have an influence on the temperature of the phase transition, because if smaller sizes are required, these sizes can be reached at lower annealing temperatures. Due to the observation that the phase transition temperature of the amorphous TiO_2 to the anatase phase increases with the addition of ZrO_2, it can be assumed that there is a rearrangement of areas with O-Ti-O-Zr-O bonds and O-Ti-O bonds, so that TiO_2 domains become large enough for crystallization.

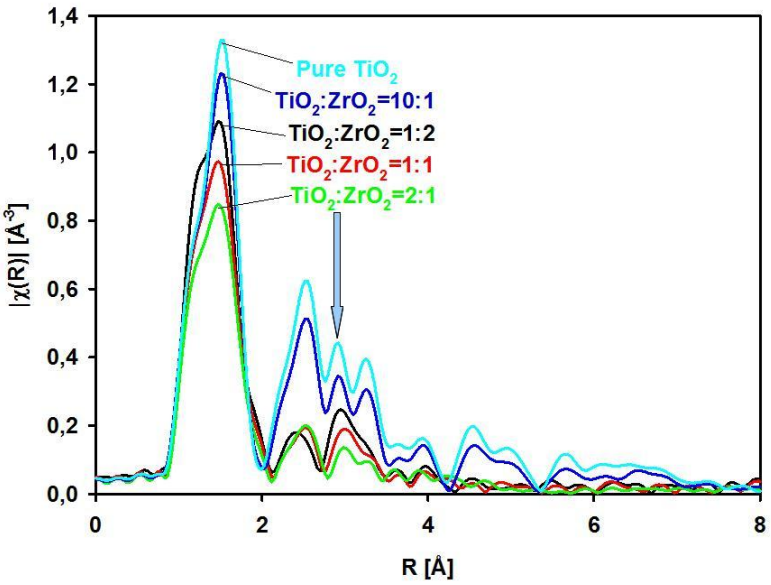

Figure 4.6: EXAFS data of samples with different TiO_2:ZrO_2 ratios annealed at T=400°C for four hours, presented in R-space (k=2 weight). The arrow shows to the peak which is due to Ti-O-Zr bonds.

Again, EXAFS data of the annealed samples provide proof for the existence of Ti-O-Zr bonds. EXAFS data of composite samples with different TiO_2:ZrO_2 ratios, annealed at T=400°C for four hours, are presented in Fig. 4.6. The peak marked with an arrow increases with increasing zirconia content in the samples and is thus due to Ti-O-Zr bonds. In this picture, it can be seen that the two graphs belonging to the samples with TiO_2:ZrO_2=10:1 and that one of the pure titania sample show strong peaks at higher binding distances, due to the crystalline order found for these two samples.

In Fig. 4.7, the XANES measurements of the samples with TiO_2:ZrO_2=6:1 are presented without annealing and for all applied annealing temperatures. As can be observed, the XANES measurements all look very much like the amorphous TiO_2 reference, especially also the pre-edge regions. A change in the XANES structure is only observed for the measurement of the powder annealed at T=500°C for four hours.

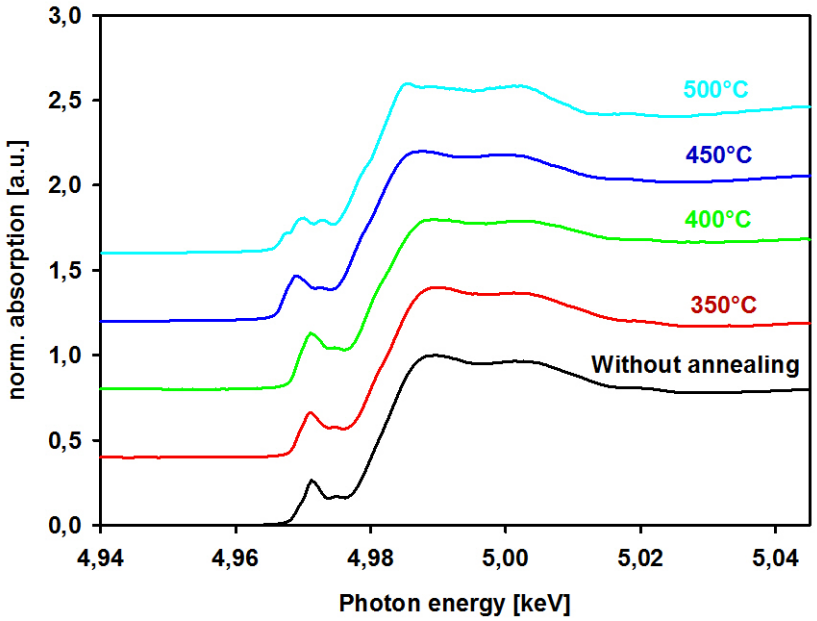

Figure 4.7: Ti K-edge of composite powders with TiO_2:ZrO_2=6:1 annealed at different temperatures and of the amorphous powder which has not been annealed. Spectra are shifted vertically with respect to each other by 0.4 units for more clarity.

There, a strong change in the pre-edge is observable, with now three clearly distinguishable peaks and a shoulder at the low energy side of the center peak. The total structure of the XANES looks more like the anatase reference, and thus the XANES measurements lead to the result that a phase transition from amorphous TiO_2 to the anatase polymorph only occurs from temperatures of T=500°C on.

If the XRD patterns of these samples in Fig. 4.8 are regarded, a first small peak, which is assignable to the anatase (101) reflex already occurs at T=400°C. At T=450°C more peaks become observable, all assignable to anatase reflexes. At T=500°C, the whole diffraction pattern of anatase in the observed angle range becomes clearly visible. There are also some peaks observable in the measurement of the powder which has not been annealed, but these cannot be assigned to any TiO_2 polymorph. Also the sample stage cannot be responsible for these peaks, whose origins are not clear. Thus, the XRD measurements show the appearance of very small fractions of anatase from annealing temperatures of T=400°C on, which are not observable with XANES.

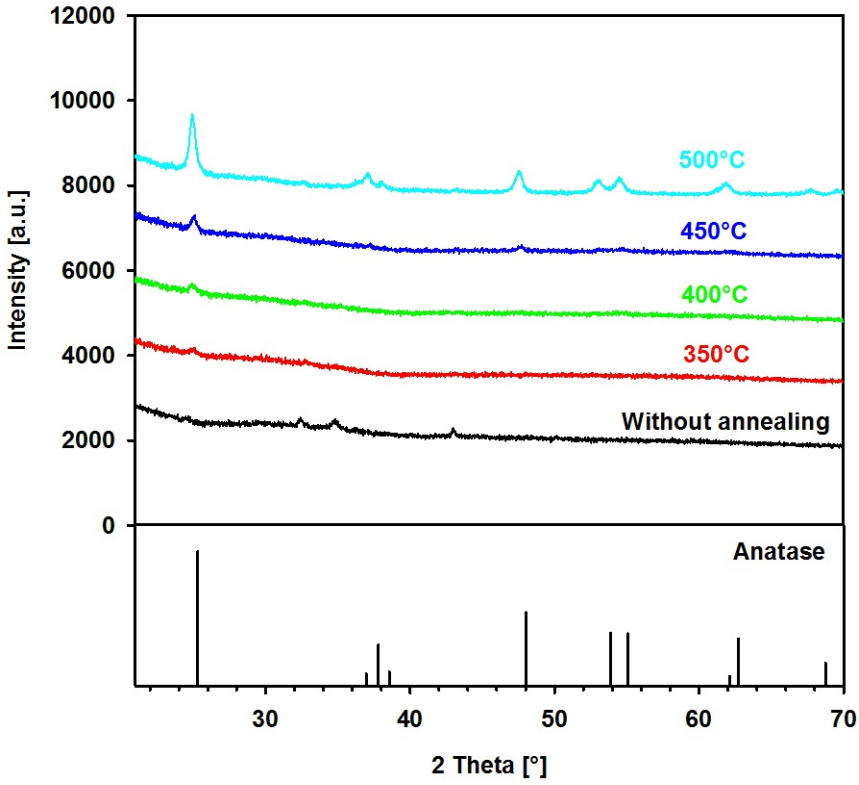

Figure 4.8: XRD patterns of the samples with TiO_2:ZrO_2=6:1 annealed at different temperatures for four hours and without annealing. Patterns are shifted with respect to each other by 1500 units for a better comparison.

In Fig. 4.5, the features which can be assigned to the anatase phase are most pronounced in the spectrum belonging to pure TiO_2. This gives a first hint that the TiO_2 in the composite samples contains larger amorphous fractions than that in pure titania. To quantify the anatase concentration in dependence on the TiO_2:ZrO_2 ratio, LC-XANES fits have been performed, the results of which are presented later in this section. Due to the necessity for high crystalline concentration in the samples and the observation that crystalline concentration decreases with increasing zirconia amount, a composite with a high titania to zirconia ratio should be found as a suitable catalyst material.

For this reason, three samples with small ZrO_2 concentrations, namely TiO_2:ZrO_2=15:1, 20:1 and 25:1, were investigated. The samples prepared with a small zirconia concentration must provide two characteristics. The first one is that the anatase amount should be as large as possible in comparison especially to the remaining amorphous fractions. On the other hand, the zirconia concentration has still to be large enough to stabilize the particle size as well as the crystalline phase in the applied temperature range.

In XRD, it is also obvious that the powders with TiO_2:ZrO_2=1:2, 1:1 and 2:1 do not crystallize after annealing at 500°C for four hours due to the absence of diffraction peaks. This can be followed from the diffraction patterns presented in Fig. 4.9 a. All diffraction peaks of the samples with high titania content can be assigned to the anatase phase by comparison with the presented simulated diffraction pattern made with Powder Cell at the bottom of the picture. Only in the samples with TiO_2:ZrO_2=15:1, 20:1 and

25:1, small peaks assignable to the brookite phase are observable, especially the peak at about $2\theta \cong 30°$, which is only observed in a closer zoom. No peaks which belong to any crystalline ZrO_2 phase are observable. This is consistent with the results of Elder et al. [1], who investigated the crystallization and stabilization of titania nanoparticles in TiO_2-ZrO_2 during hydrothermal treatment by TEM investigations. They also found that the ZrO_2 contents of their samples always stayed amorphous. In this context, the zirconia seems to behave similar to the titania in the samples with low titania content. In the composite powders with TiO_2:ZrO_2=1:2, 1:1 and 2:1, no crystallization of the titania fractions were observable. In these samples, the titania concentration is twice as high as the zirconia concentration or lower. This is also true for the zirconia concentration of these samples, in the sample with TiO_2:ZrO_2=4:1, 6:1, 8:1, 10:1, 15:1, 20:1 and 25:1 it is even much lower. Thus, if one of the oxide fractions in the composites should be able to crystallize, its relative amount should be more than twice as high than the other oxide. This is consistent with other works, where it was found that one oxide is only able to crystallize if the other one is included with concentration smaller that 25% [77].

In part b of this picture, the development of the anatase crystallite sizes is presented. The crystallites tend to be larger in composites with larger ZrO_2 concentrations, it is much larger for the sample with TiO_2:ZrO_2=10:1 than for those ones with smaller zirconia concentrations. Due to the observation that the powders are not able to crystallize in samples with too high concentrations of the other oxide, this is quite confusing at first glance. If the encapsulation theory of Elder et al. applies, it might be assumed that the spaces between the ZrO_2 network fractions are very small, thus there is not enough TiO_2 in these spaces to built up a crystal. If the ZrO_2 amount is smaller, there is more space between the ZrO_2 fractions in which titania nanocrystals can built during the annealing process. In this picture, the assumption is likely that the crystallite size should increase with decreasing zirconia concentration. This was also found for titania samples doped with zirconium [13].

Also a comparison of the anatase crystallite size behavior in dependence on the annealing temperature shows unexpected results, compare Fig. 4.10. The crystallites seem to be comparably small in samples with low zirconia content. But especially these samples are assumed to allow the growth of larger crystallites.

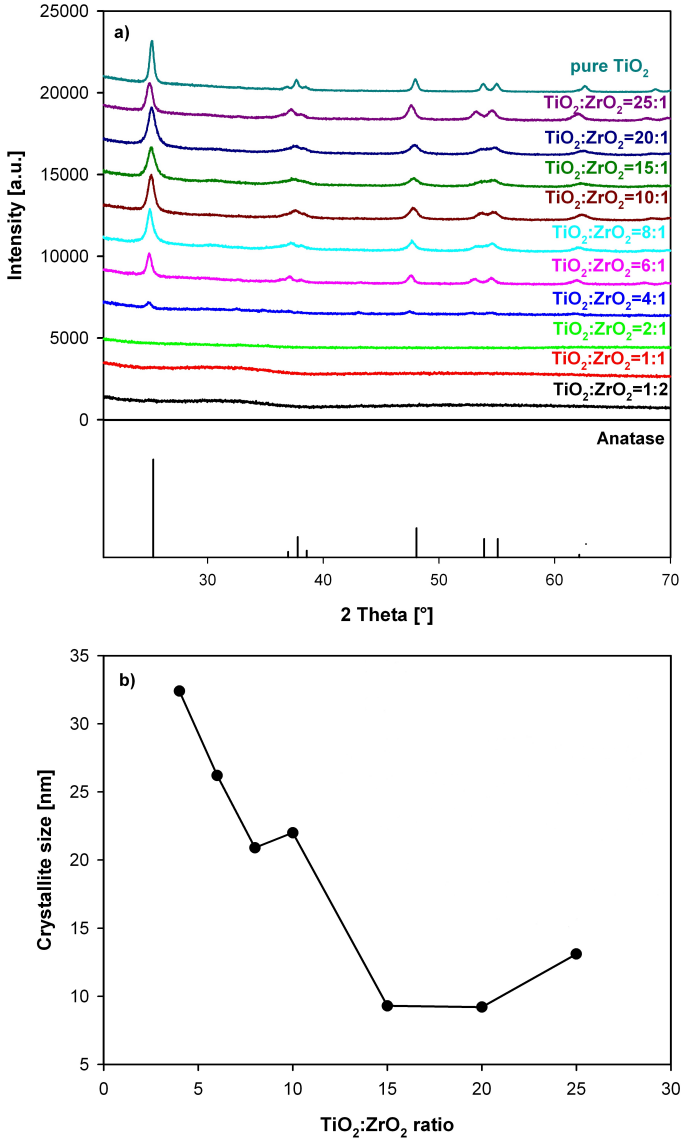

Figure 4.9: Diffraction patterns of the samples with different TiO_2:ZrO_2 ratios annealed at 500°C for four hours in part a. The anatase crystallite sizes derived from XRD peak broadening are presented in part b.

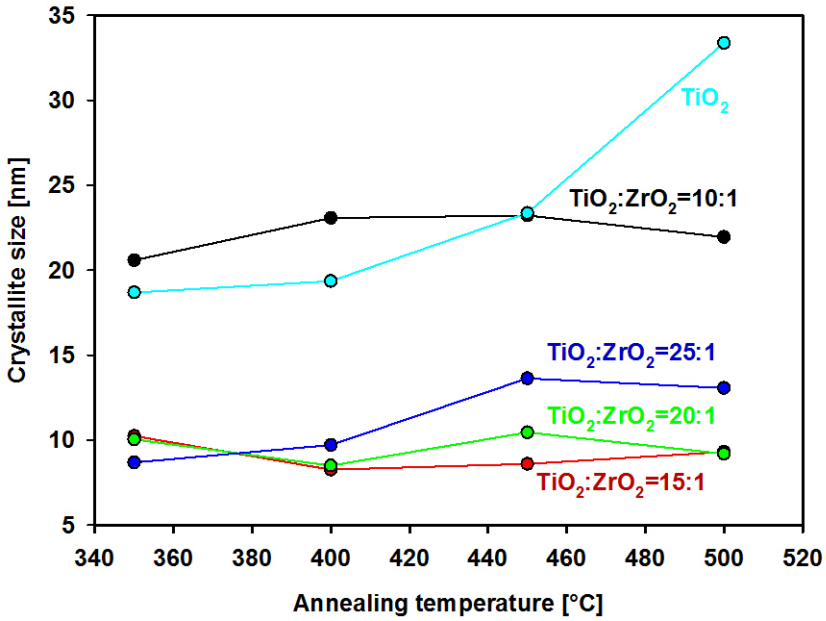

Figure 4.10: Development of the anatase crystallite size with increasing annealing temperature for the composite samples crystallizing at all applied annealing temperatures.

The size of the anatase crystallites in the samples containing brookite might be underestimated due to the following reason. As can be observed in the simulated XRD patterns, the anatase (101) peak is very close to the brookite (210) and (111) peaks (compare Fig. 2.5). These three peaks are not resolvable as single peaks in XRD. The fit of the peak is very difficult. Zhang and Banfield [23] reported about the numerical fit of these diffraction peaks. Due to the fact that the peak consists of more than the anatase (101) signal, there is an additional broadening and thus with respect to the Scherrer formula, the particle size determined from XRD data could be underestimated.

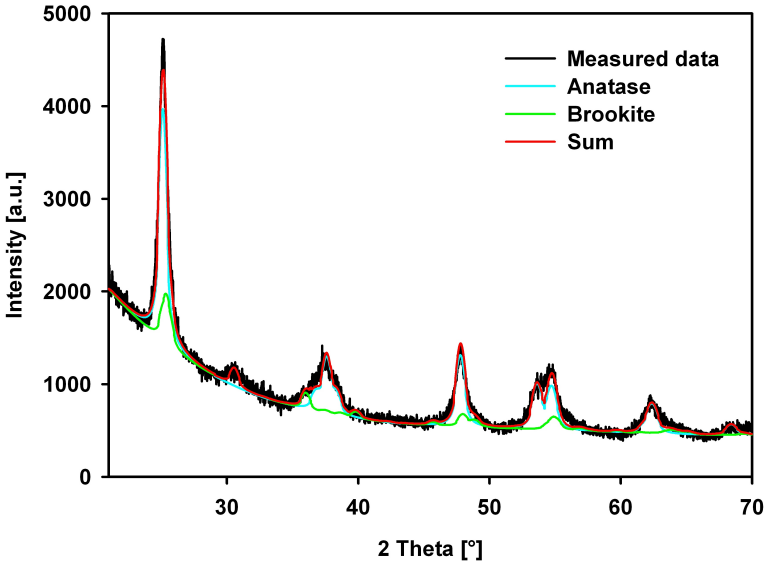

Figure 4.11: Example of a Rietveld refinement of a diffraction pattern of a composite sample with TiO_2:ZrO_2=15:1 after annealing at T=500°C for four hours.

The patterns were fitted in addition by Rietveld refinements in the PowderCell software. An example of such a refinement is presented in Fig. 4.11.

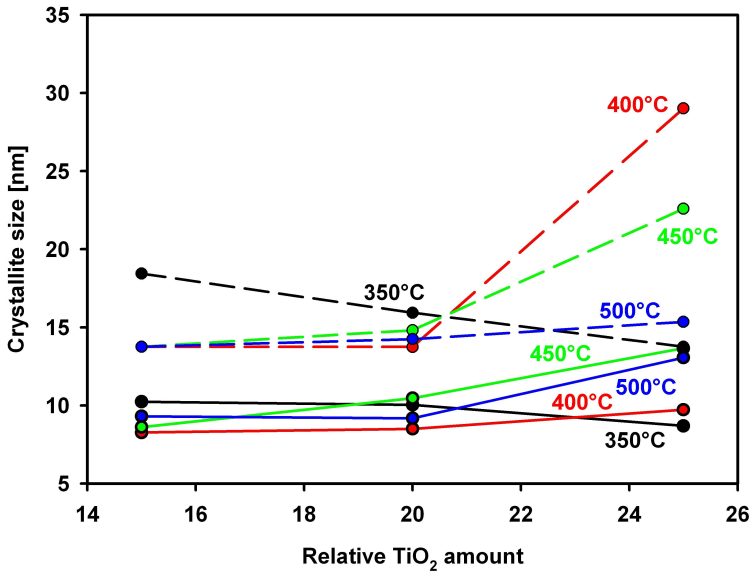

Figure 4.12: Crystallite sizes determined from peak fitting/Scherrer formula (solid lines) and from Rietveld refinement (dashed lines).

The development of the crystallite size with increasing amount of titania in the composites for different annealing temperatures, determined by the Scherrer formula (solid lines) and Rietveld refinement (dashed lines) is presented in Fig. 4.12. As can be seen, the crystallite sizes determined from Rietveld refinement are a few nanometers larger than those ones determined from Scherrer analysis. Thus, the effect of the peak broadening

due to the overlap of anatase and brookite peaks seems to give rise to an underestimation of the anatase crystallite size in Scherrer analysis. Also in the development of the crystallite sizes derived from this analysis method, the crystallite sizes stayed nearly constant for the composite powders with increasing annealing temperature. The crystallite sizes of the pure titania samples were very similar to each other for the samples annealed at T=350°C and T=400°C and showed a strong increase in size at higher annealing temperatures, like in the analysis with single peak fitting. The crystallite sizes of the powders with TiO_2:ZrO_2=15:1, 20:1 and 25:1 derived from refinement are only very slightly lower than that of the samples with TiO_2:ZrO_2=10:1. The effect of the analysis method on the magnitude of the crystallite sizes in the samples with TiO_2:ZrO_2=10:1 and in pure titania were smaller than that on the other three samples. The crystallite size of the sample with TiO_2:ZrO_2=25:1 is not constant like in the samples with TiO_2:ZrO_2=15:1 and 20:1. Instead, a small increase of the crystallite size is observable. This observation can be explained by the very small zirconia concentration in this sample, which is maybe too small for a crystallite size stabilization, which can be observed for all other composite samples. In contrast to the composites, the crystallite size development of the pure titania sample with increasing annealing temperature shows a strong growth of anatase TiO_2 crystallites, especially at annealing temperatures of T=450°C and T=500°C.

The possible influence of incorporated zirconia in the titania network can also be seen in the position of the diffraction peaks in the XRD patterns. Fig. 4.13 presents the determined lattice constant deviation $\Delta d_{anatase,(101)}/d_{anatase,(101),theo}$, where $d_{anatase,(101),theo}$ is the theoretical value of the anatase (101) plane distance, calculated from the anatase lattice constants, which can be found for example in [130] and $\Delta d_{anatase,(101)}$= $d_{anatase,measured}$-$d_{anatase,(101),theo}$. If zirconia is incorporated into the titania network via solid solution (formation of O-Ti-O-Zr-O bonds), the size difference between the titanium cations and the zirconium cation should lead to a distortion of the lattice [13]. As can be seen, the deviation of the lattice constant decreases with decreasing zirconia concentration. Also the peak shift which was observed in the EXAFS data might be due to changes in the anatase lattice constants due to zirconium atoms included in the TiO_2 lattice. The sample with TiO_2:ZrO_2=25:1 is not presented in the plots. The relative deviation shows a slight increase in the case of this sample, which might be due to influences of brookite or difficulties in the preparation of samples with very low zirconia amount. This can be due to a deviation of the peak position due to the two brookite peaks in the 2-Theta region of the anatase (101) peak, which will also change the center position of the total peak profile. This might still influence the values, although a Rietveld refinement is used for analysis here. When the zirconia concentration becomes smaller, there are not enough zirconium cations so that not every anatase unit cell can incorporate zirconium cations. Thus, there are more undisturbed anatase cells, which might be the reason for the higher crystallinity for the pure titania samples, where no cell distortions due to foreign cations occur. This result also allows the suggestion that TiO_2 is able to crystallize if only small amounts of zirconia are incorporated in the titania structure, because the XRD peaks are only due to the crystalline contributions of the samples, and thus zirconia can only influence the XRD patterns when it is incorporated in the structure of the built crystallites. In this case, the samples would remain amorphous only in the case when there is so much zirconia incorporated that the TiO_2 structure is strongly disturbed.

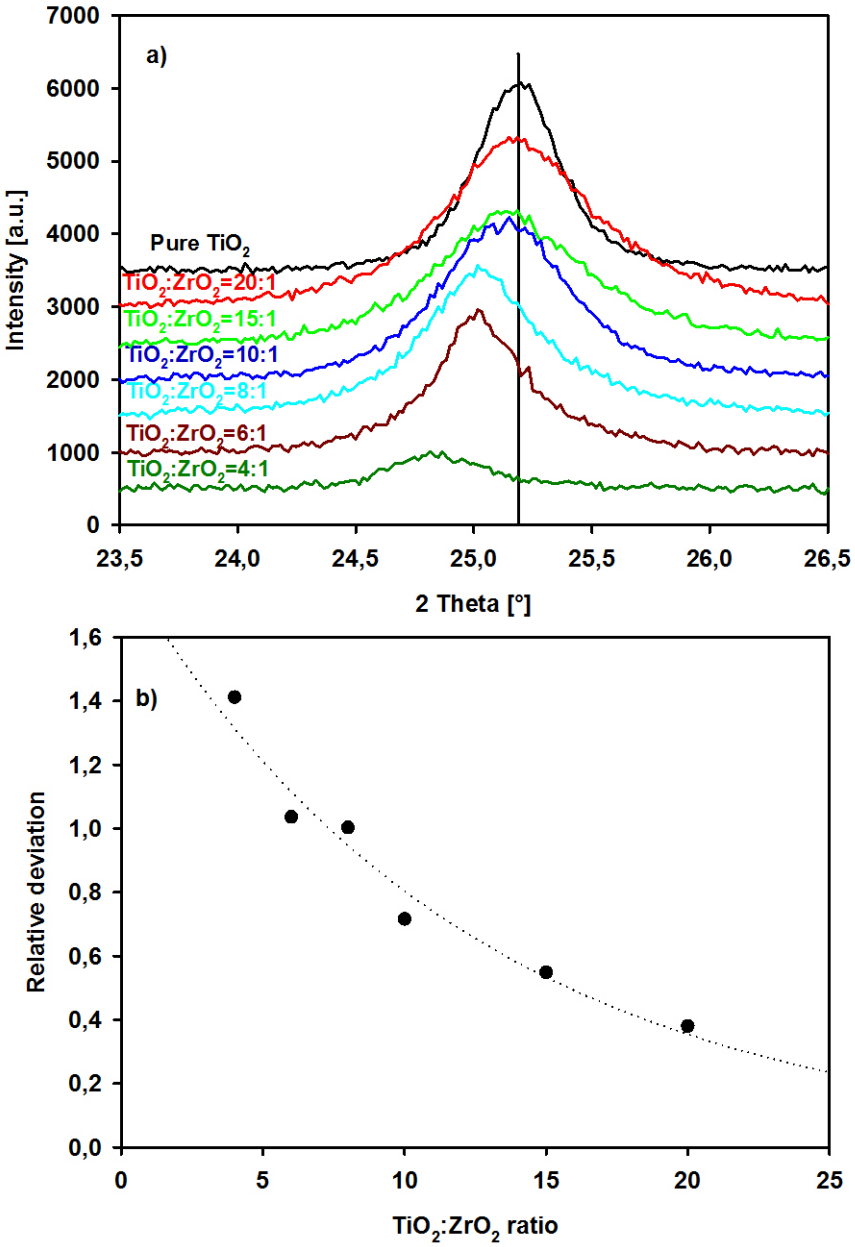

Figure 4.13: Anatase (101) XRD peaks of powders with different TiO_2:ZrO_2 ratios, annealed at 500°C for four hours in part a. Patterns were shifted vertically by 500 units for more clarity. The deviation of the lattice spacing d in dependence on the titania to zirconia concentration in part b. The dotted line presents a trend line which should just help to guide the eye.

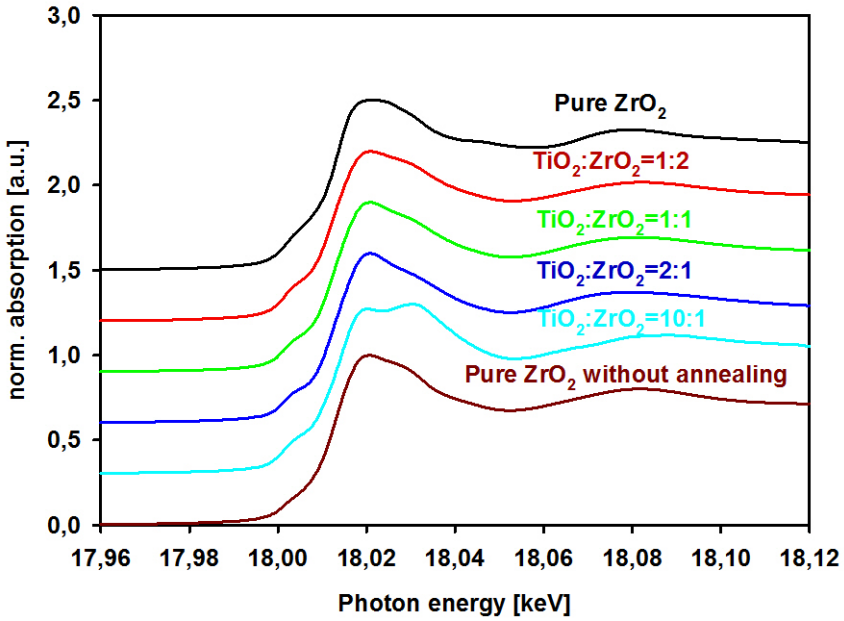

Figure 4.14: Zr K-edge XANES spectra of the samples with TiO_2:ZrO_2=10:1, 2:1, 1:1 and 1:2 and pure ZrO_2 after annealing at 500°C for four hours. The XANES spectrum of pure ZrO_2, which was not annealed is presented as a reference of the XANES structure of amorphous zirconia (black line). The spectra are shifted vertically with respect to each other by 0.3 units for a better comparison.

Fig. 4.14 shows the Zr K-edge XANES of pure ZrO_2 without annealing as a reference for amorphous ZrO_2 and the Zr K-edges of the samples with TiO_2:ZrO_2=10:1, 2:1, 1:1, 1:2 and pure ZrO_2 after annealing at T=500°C for four hours. As can be seen, most of the XANES spectra look like the amorphous reference, which is in good agreement with the absence of XRD lines in all composite samples annealed at this temperature. There are two exceptions: The sample with TiO_2:ZrO_2=10:1 and the pure ZrO_2 powder. The applied annealing temperatures are high enough for the crystallization of ZrO_2 from an annealing temperature of T=400°C on.

This can be seen in Fig. 4.15, presenting the XRD patterns of the pure ZrO_2 at all applied annealing temperatures and without annealing treatment. It can be seen that there are no diffraction lines observable for the powder which has not been annealed and for the one annealed at T=350°C. This justifies the use of the powder which has not been annealed as a reference spectrum for amorphous ZrO_2 in Fig. 4.14. At all higher temperatures, diffraction peaks are observable which are assignable to a mixture of cubic and tetragonal ZrO_2 at annealing temperatures of T=400°C and T=450°C. At T=500°C, additional lines due to the monoclinic phase are occurring.

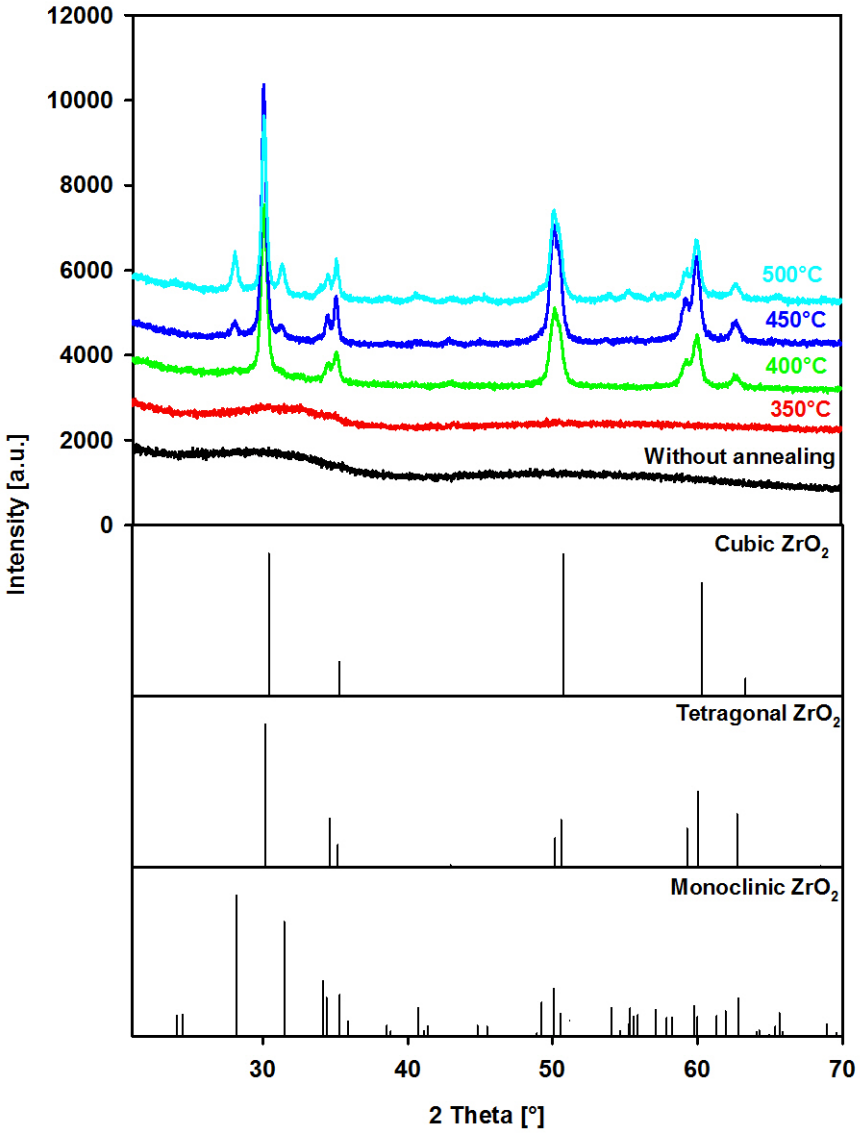

Figure 4.15: The XRD patterns of pure zirconia samples annealed at different temperatures for four hours. The second pattern is shifted vertically by 1500 units with respect to the first one, all other ones are shifted by 2500 units with respect to each other.

Thus, it is not surprising that the XANES spectrum belonging to the pure ZrO_2 sample does not look like the amorphous reference, it is a superposition of the three included crystalline phases and the remaining amorphous fractions. It does not fit to the XRD observations that the XANES belonging to the sample with TiO_2:ZrO_2=10:1 does not look like the amorphous reference. In XRD, no diffraction lines due to ZrO_2 phases are observable for all annealing temperatures for this composition. It showed up in the observations on the TiO_2 fractions of different composites that oxides in the composites are only able to crystallize if its relative amount in the sample is high. This is obviously not the case for ZrO_2 in the sample with TiO_2:ZrO_2=10:1. Even thought

the ZrO_2 in this sample might have been crystallized, XRD peaks should be observable also for this very small amount of crystalline ZrO_2 in the sample, due to the higher intensities of zirconia diffraction peaks with respect to those of titania, resulting from the higher atomic form factor. Thus, with the exception of the structure of the XANES spectrum belonging to the sample with TiO_2:ZrO_2=10:1, there is every indication that the zirconia in this sample also stays amorphous, what will be assumed here.

As it was explained in the theoretical section, the degree of crystallinity is a very important parameter in many applications of TiO_2. The amount of crystalline and amorphous phases can be determined from linear combination fits of the XANES spectra (LC-XANES). What is made qualitatively till here can be made quantitatively this way.

An example of an LC-XANES fit is depicted in Fig. 4.16 a for the sample with TiO_2:ZrO_2=15:1 after annealing at T=400°C for four hours. The development of the concentration of the desired anatase phase with increasing annealing temperature is presented in part b of the picture. As it shows up, the anatase phase concentration increases with increasing annealing temperature due to crystallization of the amorphous phase. Because of the thermodynamic stability of the anatase phase at low crystallite sizes, anatase is first formed from the amorphous precursor. What is seen as amorphous material in the XANES are signal fractions from titanium absorbers with distorted coordination. This is fulfilled for large volume fractions of the material which have no ordered structure, but this is also true for the titanium absorber at the surfaces of crystals. Thus, if there would be no remaining amorphous fractions in a powder, but the crystallites would be very small, amorphous fractions could be determined from XANES measurements due to large signal fractions from the particle surfaces. This could bring a small error to the determined amorphous fractions, because the surfaces are of course part of the crystalline materials, but might contribute to an amorphous signal. Brookite can also be built in the case of small crystallite sizes, because the thermodynamic stability is very close to each other at small crystallite sizes, see section 2.4. As it was mentioned above, the crystallite sizes of the samples with TiO_2:ZrO_2=15:1, 20:1 and 25:1 are smaller than the ones of pure TiO_2 and TiO_2:ZrO_2=10:1 after annealing at T=500°C for four hours. Indeed, XRD patterns included some very weak diffraction lines assignable to the brookite phase. Thus, it is difficult to suppress the formation of brookite with zirconia addition, because of the close thermodynamic stabilities of anatase and brookite at small crystallite sizes. Higher annealing temperatures are required for a high degree of crystallinity, which shows the importance of the crystallite size stabilization to avoid the growth of crystallites to undesired high diameters during the high temperature annealing processes.

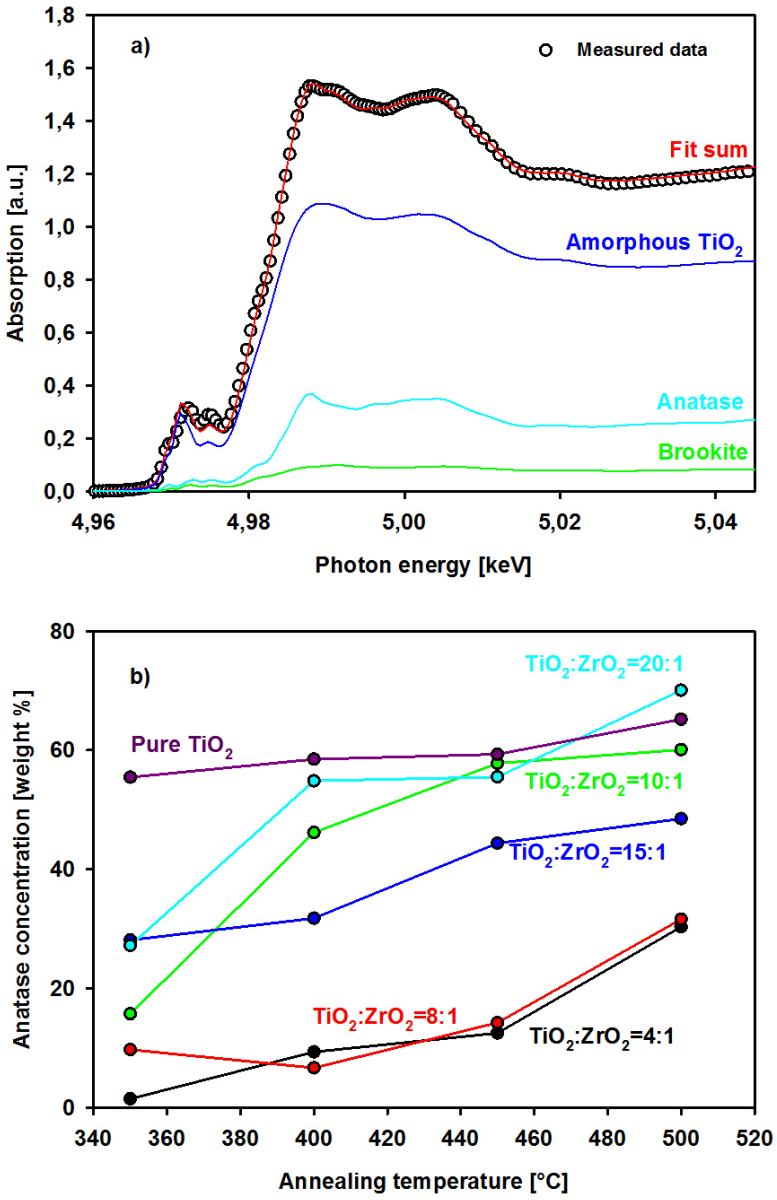

Figure 4.16: Example of an LC-XANES fit of a sample with TiO_2:ZrO_2=15:1 at the Ti K-edge, annealed at T=400°C for four hours in part a. The anatase concentrations derived from the LC-fits for the samples with varying titania to zirconia ratio in dependence on the annealing temperature are presented in part b. The concentrations of the samples with TiO_2:ZrO_2=1:6 are not presented in this plot.

It also shows up that the anatase concentration is smaller for the composites than for the pure TiO_2 powders at a certain annealing temperature. This leads to the necessity to keep the zirconia concentration in the samples as small as possible to achieve the crystallization of large amounts of the titania fractions during the annealing processes. Thus, the samples with TiO_2:ZrO_2=15:1, 20:1 and 25:1 are the most interesting candidates for

good material characteristics. If the anatase concentration is observed, it can be seen that the sample with TiO_2:ZrO_2=15:1 shows a comparably small increase in concentration, while the increase for the other two oxide ratios is higher and the anatase concentrations reached at T=500°C are higher. For the ratio of TiO_2:ZrO_2=25:1, it should be kept in mind that there was an increase in the crystallite size with increasing annealing temperature. Thus, this low zirconia concentration might be too small to stabilize the crystallite size and thus there is also a higher probability of phase transitions for certain reaction paths which might favor phase transitions. Due to these observations, the sample with TiO_2:ZrO_2=20:1 is used for further investigations, in which the influence of the reaction environment on the materials structure is investigated and the structural changes due to the reaction environments are compared for the TiO_2:ZrO_2=20:1 composite samples and pure titania samples. (The samples with TiO_2:ZrO_2=6:1 show strange fluctuation in the anatase concentration. The results are not presented here, the sample system with this oxide ratio was discussed above.)

4.3 Influence of the reaction environment on the materials structure

In the following section, the investigations of pure TiO_2 and composite TiO_2:ZrO_2=20:1 powders prepared in different reaction environments are presented. The influence of the reaction paths on structural parameters is first examined with respect to the structure of the amorphous precipitates. The clusters in these untreated precipitates work as crystallization nuclei during the annealing process and thus might have a critical influence on the crystallization and the structure of the nanocrystallites formed. The examination of the structure of the crystalline, i. e. annealed materials, is the topic of the second part of this section.

4.3.1 Structure of the untreated precipitates

A first qualitative hint to the structure of the TiO_2 clusters in the precipitates can be derived from the XANES pre-edge peaks. Similar investigations were already explained in section 4.1.

A first look on the pre-edge spectra of the samples prepared with different electrolytes is presented in Fig. 4.17. Some differences in the shapes can be observed. In the samples prepared with alkaline electrolytes, i.e. KOH and NaOH, the shoulder at the low energy side of the pre-edge, which is the A1 peak, is less pronounced compared to the samples prepared with hydrochloric acid. Also the A3 peak, which is the shoulder at the high energy side of the most intense A2 peak, is a bit more pronounced, indicating a slightly higher cluster size in the precipitate. The pre-edges of the samples prepared in basic reaction media are very similar to each other. The changes of the pre-edge structure with respect to the used electrolyte are very similar for the composite and the pure titania samples.

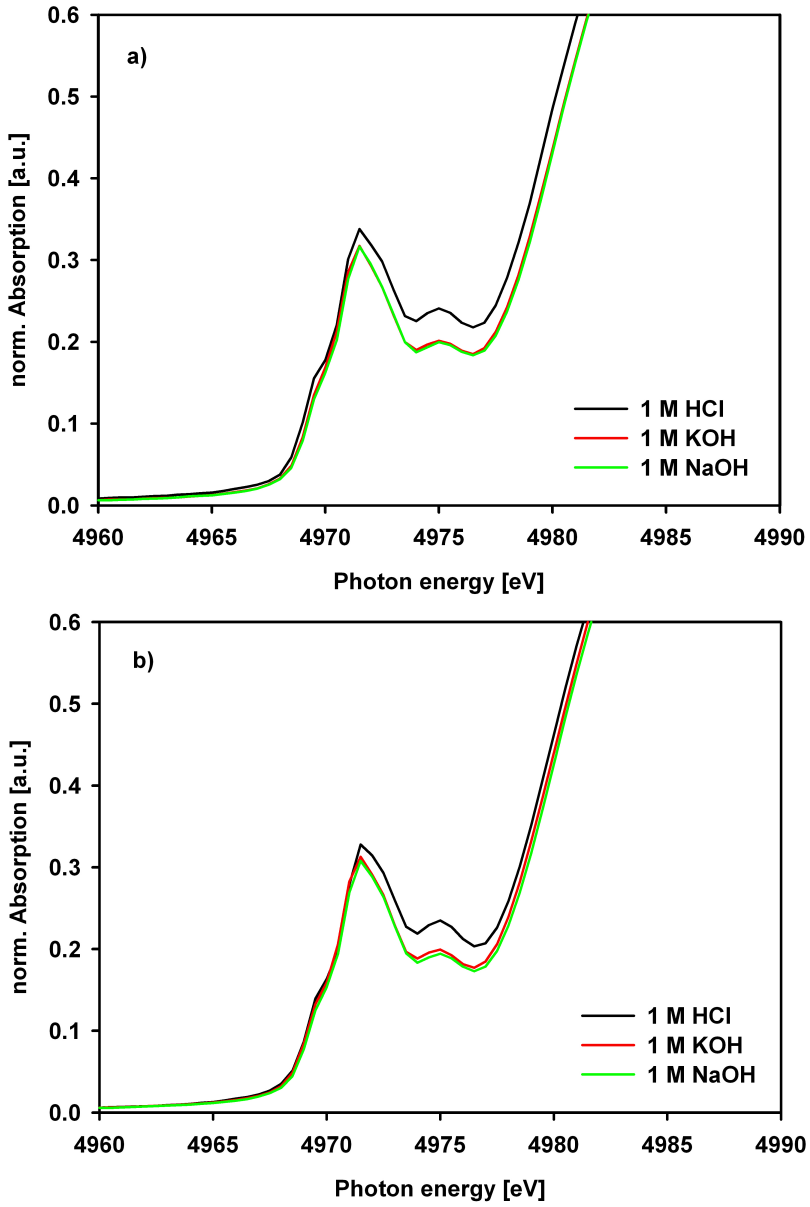

Figure 4.17: Pre-edge features of Ti K-edge of untreated composites (part a) and pure titania samples (part b) prepared with different electrolyte solutions.

In the samples prepared with different water to alkoxide ratios, there is no significant change of the pre-edge peak shape with the amount of added water for the composite samples. In the case of the pure titania samples, data is only available for water to alkoxide ratios of 1:2 and 1:8, also no significant change in pre-edge structure was observable here. In the case of the samples prepared with alcohol dilution, data was only collected from the composite samples, where no shape-changes were observable. Thus, these methods do not seem to have much effect on the precipitate structure.

The XANES Ti K-edge spectra of the pure TiO_2 powders synthesized with different amounts of 1 M hydrochloric acid are presented in Fig. 4.18 a. In the development of

the XANES structure with increasing amount of added acid, it is obvious that the edges show first tendencies to the anatase structure, especially for the powder synthesized with TTIP:HCl ratio of 1:8. Thus, there seems to be much more structural order in this precipitate than in those ones prepared with lower amounts of HCl. The development of the I_{A3}:I_{A2} peak intensity ratio is presented in part c (red dots). As can be observed, there is a distinct increase in the intensity ratio, which leads to the assumption that larger clusters occur in the precipitates synthesized with more HCl. This is in good agreement with the suggestion made from the observations of the whole XANES structure in part a, that the order increases with increasing HCl amount. Such observations were already made by Gopal et al. [42], who also found an explanation of their results on the basis of the influence of the added HCl with respect to the relative rates of hydrolysis and condensation in the sol-gel synthesis, see section 2.3.

In summary, the explanation is that the positive H_3O^+ cations resulting from the HCl dissociation in aqueous solution arrange as clouds around the negatively charged organic ligands of the TTIP molecule. Thus, the negative partial charge of the ligands with respect to the positively charged Ti ion is reduced by the positively charged cloud. In this way, the electromagnetic attraction forces between metal ion and organic ligands are reduced and thus the stability toward hydrolysis is also reduced. This leads to an increase in the hydrolysis reaction rate. On the other hand, the positively charged H_3O^+ ions will also built a cloud around the formed hydroxides and lead to repulsive forces between the titanium hydroxide molecules. The polycondensation reaction occurs if two hydroxide ligands can 'touch' to built a Ti-O-Ti bond. If now the repulsive forces between the hydroxide molecules increase, the polycondensation rate is decreased. Due to the slower polycondensation, the TiO_2 molecules and clusters have more time to arrange in an energetically favorable, more ordered way, leading to larger clusters.

XANES spectra of TiO_2:ZrO_2=20:1 composite powders prepared with different amounts of 1 M hydrochloric acid are presented in Fig. 4.18 b, the results of the determination of I_{A3}:I_{A2} pre-edge peak intensities are presented in part c (black dots). As it shows up, the increase of the I_{A3}:I_{A2} ratio with increasing amount of added hydrochloric acid is very small, from about 0.405 for alkoxide:HCl=1:2 to 0.435 for alkoxide:HCl=1:8. The comparison with the intensity ratio development for pure titania shows the strong suppression of cluster growth in the synthesis step by zirconia addition. Between the powders prepared with alkoxide:HCl ratio of 1:2 and 1:4, there is nearly no difference between the peak intensity ratios. An increase of only 0.03 is observed for the sample with alkoxide:HCl ratio of 1:8. Thus, the influence of the alkoxide to hydrochloric acid ratio on the precipitate structure is only very small for the composite samples.

In comparison to the composite powders prepared with hydrochloric acid, the pure titania powder can be influenced much more by the addition of large amounts of hydrochloric acid. Thus, it can be concluded that the preparation path has a smaller effect on the composite precipitate structure than it has on the pure titania precipitate structure.

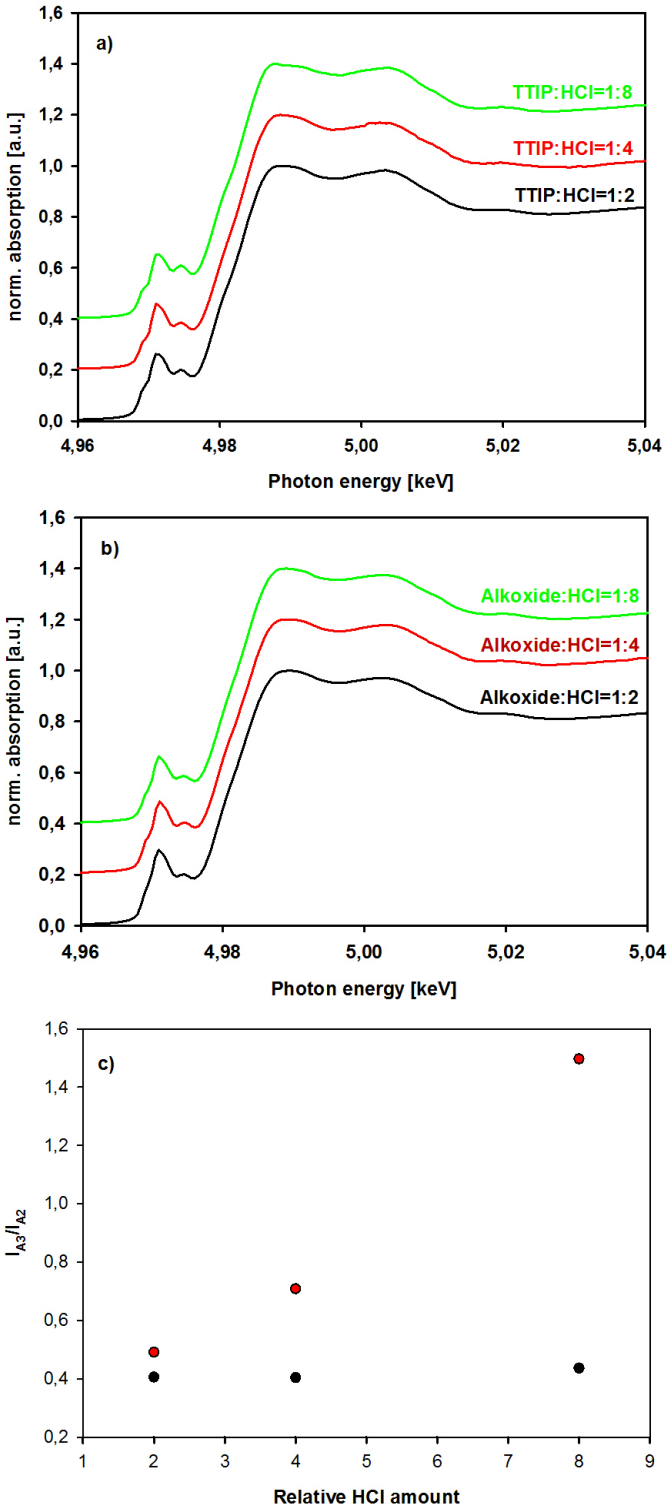

Figure 4.18: XANES Ti K-edge of pure titania in part a and of TiO_2:ZrO_2=20:1 composite powders in part b. In both parts, the spectra are shifted vertically with respect to each other by 0.2 units for a better comparison. The I_{A3}:I_{A2} peak intensity ratio is presented in part c for the composite samples (black dots) and the pure titania samples (red dots).

4.3.2 Structure of the materials after annealing or ageing

Now, the structure of the samples prepared in different synthesis ways is investigated after annealing, leading to crystallization of the amorphous, as-prepared powders. Samples are characterized after annealing at T=350-500°C for four hours. As will be seen, crystallization does not necessarily need heat treatment, but can also be achieved by storage of the amorphous samples for some months in ambient conditions at room temperature.

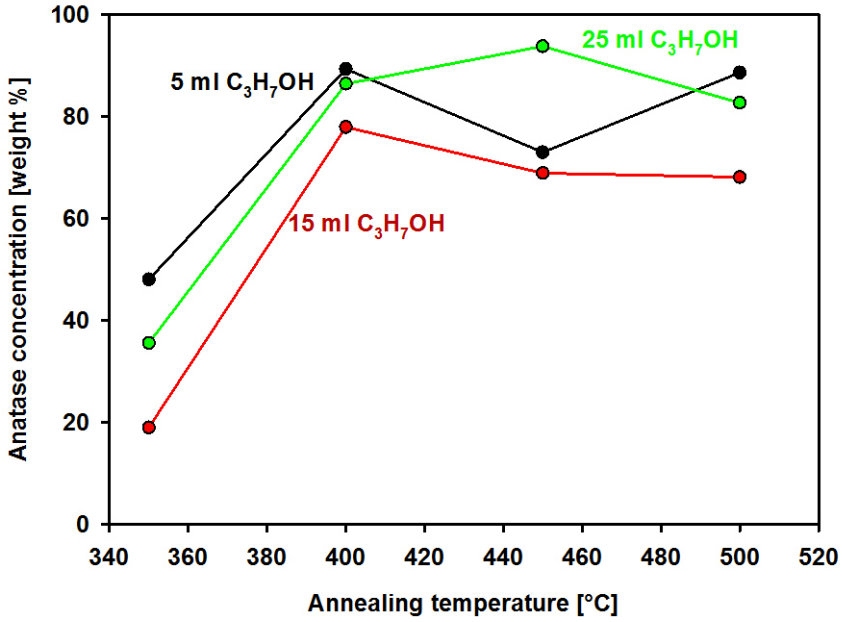

Figure 4.19: Development of the anatase concentration in dependence on the annealing temperature for TiO_2:ZrO_2=20:1 composite powders prepared in different amounts of propanol dilution.

Fig. 4.19 presents the LC-XANES results for the anatase concentration for composite samples prepared in propanol dilution.

In all samples, the anatase concentration increases with increasing annealing temperature, while the particle size derived from XRD stays constant over the whole temperature range. In all samples prepared in different alcohol solution, only the anatase crystalline phase could be observed. It shows up that the anatase concentration increases quickly between T=350°C and T=400°C and then reach a level of about 80 % anatase in the TiO_2 contents. So in these powders it seems that no very high calcination temperature is necessary to achieve comparably good crystallinity.

The crystallite sizes of the composite samples prepared with alcohol solution vary between about 9.5 and 16 nm. There are slight increases of the anatase crystallite size with increasing annealing temperature, but they are very small and not comparable to the increase by about 20 nm for the pure titania sample presented in section 4.2. There may be a slight increase, but crystallite growth is strongly constrained due to the addition of zirconia.

Pure titania samples synthesized with alcohol dilution lead to materials with anatase concentrations of 70%, 84% and 76% for dilution with 5, 15 and 25 ml propanol, derived

from LC-XANES fits. The development of the anatase concentration was measured for the pure titania sample prepared with 25 ml propanol.

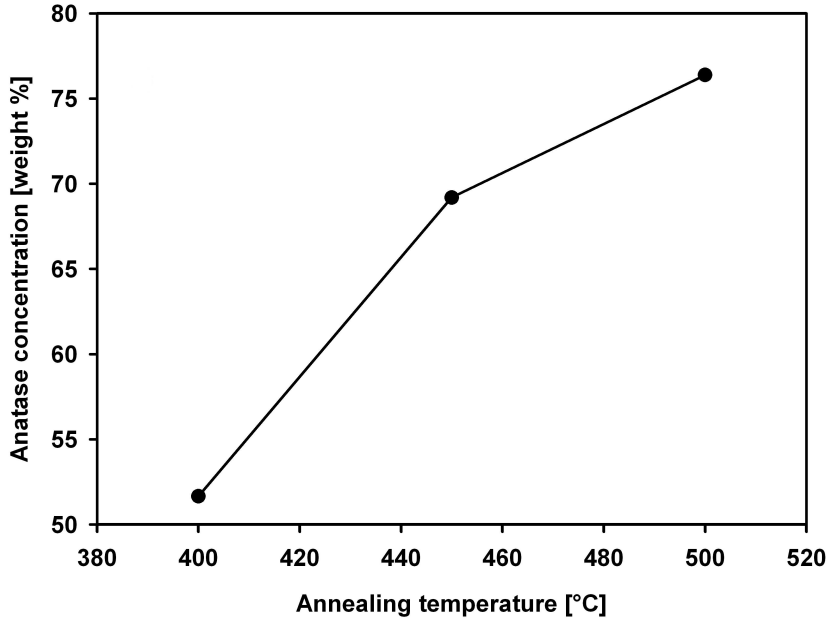

Figure 4.20: Development of the anatase concentration in dependence of the annealing temperature of the pure titania samples prepared with dilution in 25 ml propanol.

The results for the anatase concentration derived from LC-XANES fits are presented in Fig. 4.20. It shows up that the anatase concentration shows a strong increase for annealing temperatures between 400°C and 500°C in contrast to the composite samples, where a strong increase in the anatase concentration between 350°C and 400°C and a nearly constant concentration between 400°C and 500°C was observed. The growth might be unconstrained due to the missing ZrO_2. In the composite samples, the crystallite size does not increase much and thus, due to smaller anatase particles, there are more titanium absorbers at the surface, which might lead to a larger signal from titanium absorbers with distorted coordination environment. When the anatase crystallite or particle size increases, more absorbers are in the bulk. In this case, the crystallinity increases according to x-ray absorption. If the particle size is constant and does not increase, the number of surface absorbers stays constant and there will be no increase due to this effect.

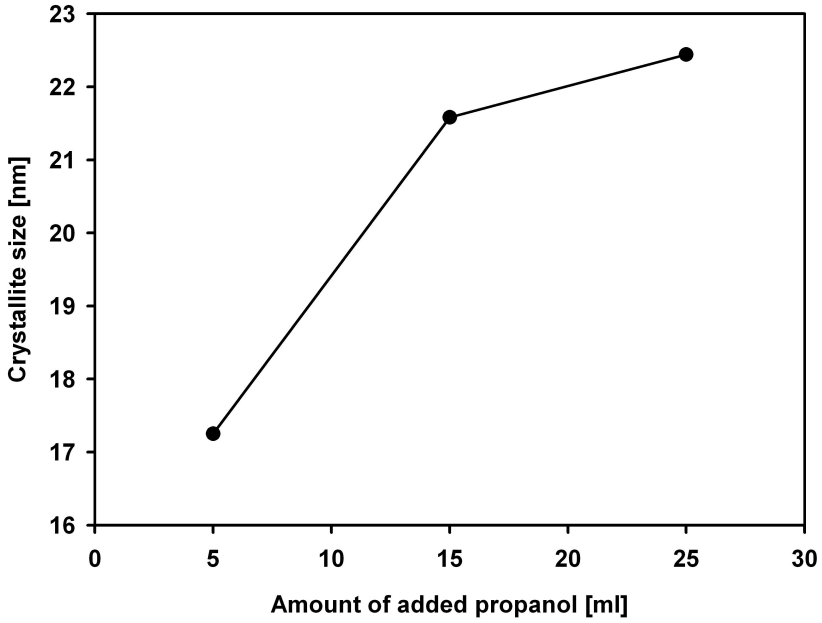

Figure 4.21: Development of the anatase crystallite size in dependence of the annealing temperature of pure titania samples prepared with dilution in 25 ml propanol.

The crystallite size of the pure titania samples prepared with alcohol dilution of the TTIP precursor is presented in Fig. 4.21. The crystallite sizes vary between about 17 and 22.5 nm and is thus larger than those ones for the composite samples. In contrast to the composites, where no trend of the crystallite size with respect to the amount of added propanol in the reaction step was observed, there is an increase of the crystallite size with increasing amount of added propanol for the pure TiO_2 samples. As can be observed in Fig. 4.20, the increase of the anatase concentration and that one of the anatase crystallite size show very similar trends. Between 400°C and 450°C, there is a stronger increase than between 450°C and 500°C. This is in good agreement with the theory that the measured crystallinity is influenced by the particle size due to surface effects.

Fig. 4.22 a and b show the results for the composite samples synthesized with different amounts of added water in the hydrolysis step. A constant value of anatase concentration from a certain temperature on, like in the samples synthesized in alcohol solution, is not observed here. The anatase concentration increases over the whole annealing temperature range. Due to the observation that the crystallinity is lower in these samples, it might be assumed that there is still a significant amorphous titania content, which is not only due to the distorted coordination at the crystallite/particle surface.

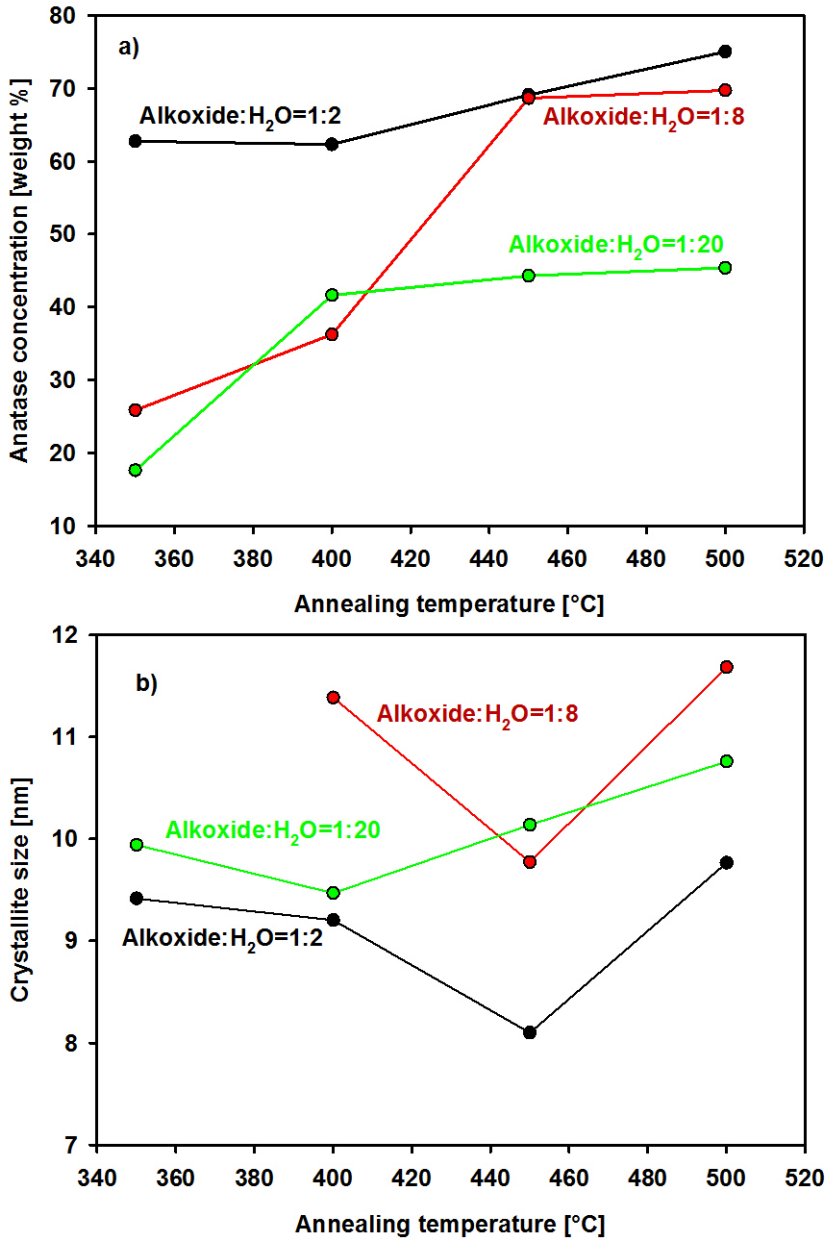

Figure 4.22: Development of the anatase concentration (part a) and crystallite size (part b) in dependence of the annealing temperature for TiO_2:ZrO_2=20:1 composite powders prepared with different amounts of water.

The increase in the anatase concentration might be due to the crystallization of these amorphous fractions. The maximum values reached are about 60-70 % anatase in the TiO_2 fractions. Pure TiO_2 synthesized with TTIP:H_2O=1:2 and 1:8 and annealed at T=500°C for four hours lead to anatase concentrations of 75% and 79%, similar to the values reached in the composites, only slightly larger, comparable to those ones reached in the composite samples prepared in alcohol diluted reaction medium. Thus, there is no significant difference in the degree of crystallinity between the pure TiO_2 and TiO_2-ZrO_2

composite materials synthesized with different amount of water in dependence on the alkoxide:H_2O ratios.

The crystallite sizes in the composite samples vary between 9 and 12 nm and are thus smaller than those ones in the samples prepared with alcohol dilution. For the sample prepared with alkoxide:H_2O=1:8, no suitable diffraction peaks for data analysis could be found in the XRD data after annealing at 350°C. In pure titania samples prepared with TTIP:H_2O=1:2 and 1:8, the crystallite sizes were found to be 15.0 nm and 15.9 nm after calcination at 500°C for four hours. Thus, the crystallites were again larger than in the composite samples, but like in the case of the composite samples, they are smaller than in the pure titania samples prepared with propanol dilution than in those ones prepared with different amounts of water.

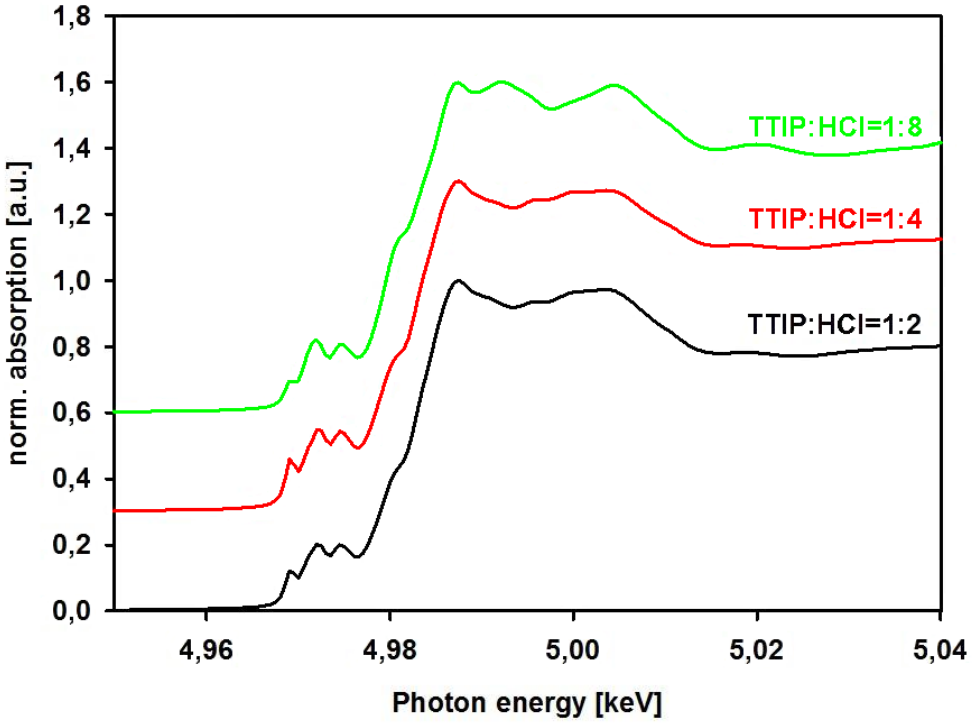

Figure 4.23: XANES measurements of pure TiO_2 powders synthesized with different amounts of hydrochloric acid and annealed at 500°C for four hours. Spectra are shifted vertically with respect to each other by 0.3 units.

Fig. 4.23 presents the XANES spectra of pure titania samples prepared with TTIP:HCl ratios of 1:2, 1:4 and 1:8 after annealing at 500°C for four hours. As it shows up, the samples prepared with TTIP:HCl=1:2 and 1:4, the last one already discussed above, seem to include the anatase phase as the only crystalline phase. In contrast, for the sample prepared with TTIP:HCl=1:8, the XANES looks very similar to the rutile reference, compare Fig. 2.4.

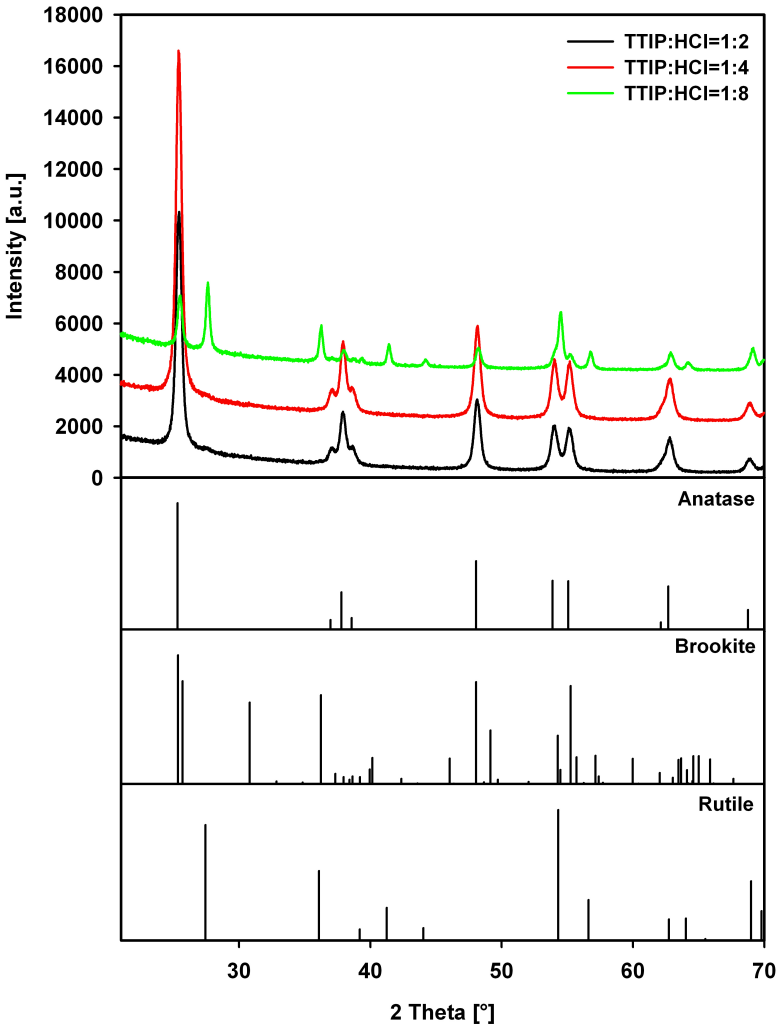

Figure 4.24: XRD measurements of pure TiO_2 powders synthesized with different amounts of hydrochloric acid and annealed at 500°C for four hours. Patterns are shifted with respect to each other for more clarity by 2000 units.

The XRD patterns of pure TiO_2 powders prepared in different amounts of 1 M hydrochloric acid and annealed at 500°C for four hours are presented in Fig. 4.24. As it shows up, the powders synthesized with TTIP:HCl ratios of 1:2 and 1:4 only crystallize in the anatase phase and do not show significant peaks which can be assigned to the rutile or brookite phases. In contrast to this observation, the XRD pattern belonging to the powder prepared with a TTIP:HCl ratio of 1:8 show peaks which can be ascribed to the rutile phase by comparison with the simulated rutile diffraction pattern.

These results are in good agreement with the PCA and linear combination of the XANES spectra of these powders in dependence on the annealing temperature, which also show only a mixture of the anatase phase and remaining amorphous TiO_2 for the samples prepared with TTIP:HCl=1:2 and 1:4 and mixtures of anatase, rutile and residual amorphous TiO_2 for the samples with TTIP:HCl=1:8.

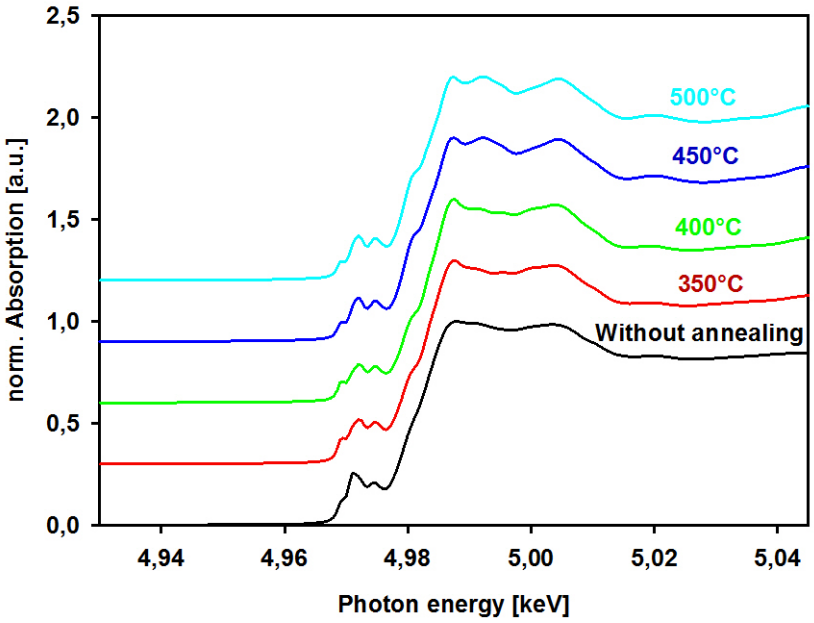

Figure 4.25: XANES spectra of pure titania samples prepared with TTIP:HCl=1:8 without annealing and at different annealing temperatures. Spectra are shifted vertically with respect to each other by 0.3 units.

In Fig. 4.25, the XANES spectra of pure titania powders synthesized with TTIP:HCl=1:8 and annealed at different annealing temperatures are presented. Next to the annealed samples, the spectrum of the powder which was not annealed is shown. As can be observed, the first phase transition is that of amorphous TiO_2 transforming to anatase at 350°C. Also at 400°C, the XANES looks very much like that of the anatase reference. For annealing temperatures of 450°C and 500°C, the XANES starts to resemble the structure of the rutile reference. In this temperature region, the second phase transition from the anatase to the rutile phase becomes very fast. Small amounts of rutile are already observable in the XANES spectra of the powders annealed at 350°C and 400°C.

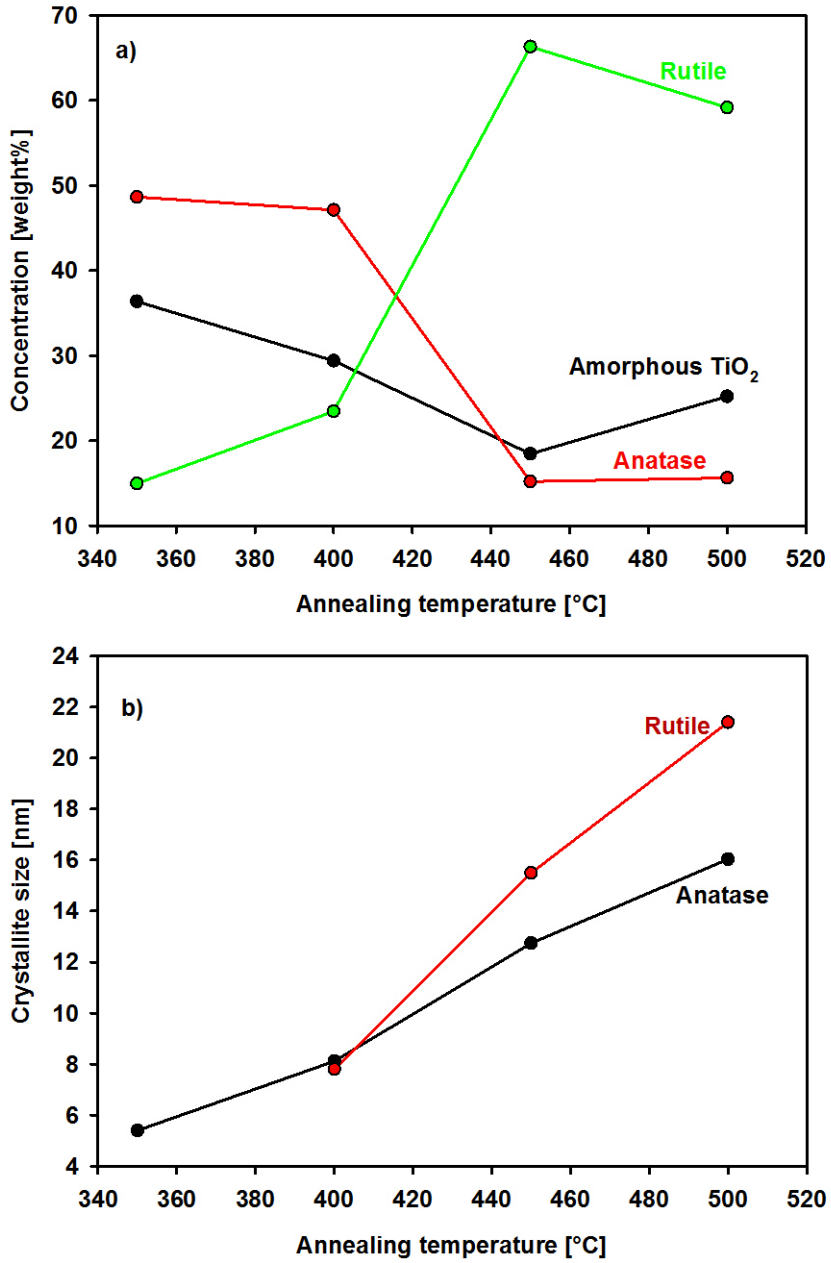

Figure 4.26: Development of the crystalline phase concentrations (part a) and crystallite sizes (part b) in the pure titania samples synthesized with TTIP:HCl=1:8 in dependence on the annealing temperature.

The development of the concentrations of the different phases determined from LC-XANES and the particle sizes of the anatase and rutile crystallites determined from XRD peak broadening are presented in Fig. 4.26 a and b. As can be seen, the anatase and the amorphous concentration both decrease with increasing annealing temperature, while the rutile concentration increases. This shows that the rutile crystallites grow at the cost of the crystallites of the anatase phase. Due to the trend that the anatase and the

amorphous phase both decrease, it might be assumed that the reaction rate of the phase transition from the amorphous to the anatase phase is smaller than that of the anatase-rutile phase transition. The development of the particle sizes shows that the anatase crystallite size is lower than the rutile particle size for all annealing temperatures. This is in agreement with the theory of Zhang and Banfield, suggesting that the anatase to rutile phase transition occurs when the anatase crystallites reach a critical size [23]. It is observable that the increase in the rutile crystallite size is larger than that of the anatase crystallite size, both presented in part b of Fig. 4.26. In context with the results from the LC-XANES measurements, this might be an additional hint that the phase transition from the amorphous to the anatase phase is slower, so that the crystallite growth rates are slower, but the anatase to rutile transformation rate is faster, so these particles grow faster.

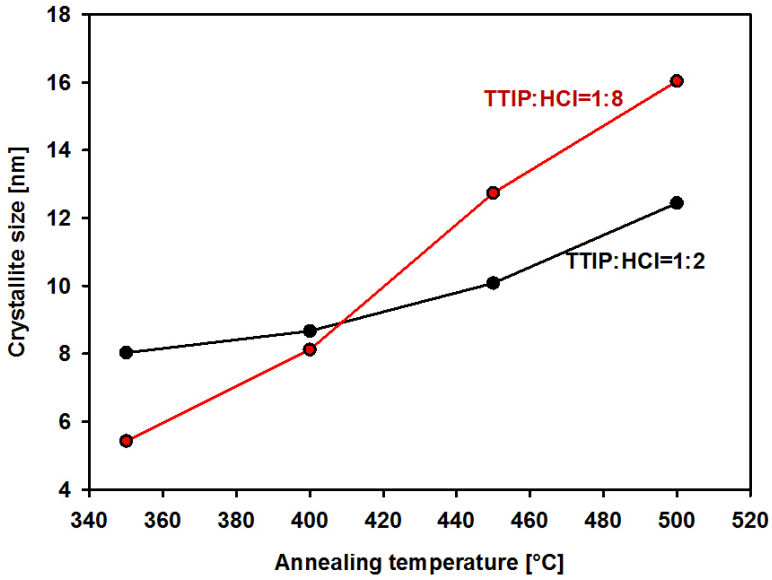

Figure 4.27: Development of the anatase crystallite size with increasing annealing temperature for pure titania materials prepared with TTIP:HCl=1:2 and TTIP:HCl=1:8.

The evolution of the crystallite size with increasing annealing temperature of the sample prepared with TTIP:HCl=1:2 is presented in Fig. 4.27. The development for the samples prepared with TTIP:HCl=1:8 is presented again for comparison. The particle size increases from about 8 nm to about 12.5 nm and thus remains much smaller compared to those ones prepared with TTIP:HCl=1:8. The growth is much slower. In comparison with the crystallite growth of the samples prepared with TTIP:HCl=1:8, the initial crystallite size at T=350°C is about 2 nm larger, but the crystallite growth and the final size at T=500°C is much slower, which is in good agreement with the theory, which states that small particles are growing faster due to the stronger driving force to reduce the surface energy by growing. The reached crystallite size is smaller than the critical sizes for phase transition to rutile, given by Zhang and Banfield to be about 11 nm [23]. This explains why there is no rutile formed in the annealing process for TTIP:HCl=1:2 samples, even at T=500°C.

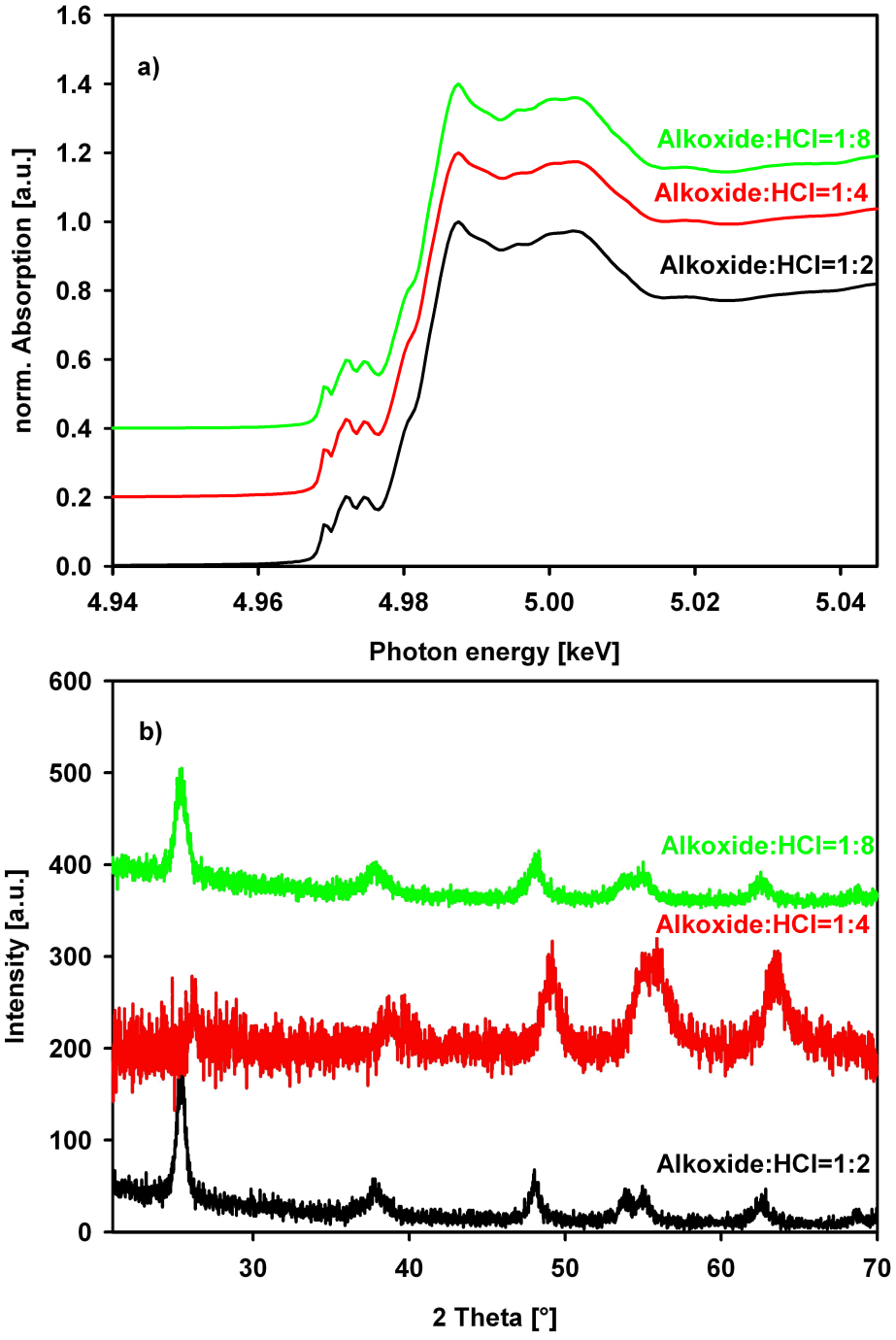

Figure 4.28: XANES (part a) and XRD (part b) measurements of TiO_2:ZrO_2=20:1 composite samples synthesized in different HCl amounts and annealed at 500°C for four hours. The XANES spectra are shifted vertically with respect to each other by 0.2 units, the XRD patterns are shifted by 200 units. The XRD pattern belonging to the sample prepared with alkoxide to HCl ratio of 1:4 has been background subtracted for better presentation.

The XANES and XRD measurements of the TiO_2:ZrO_2=20:1 composite powders synthesized with different alkoxide:HCl ratios and annealed at T=500°C for four hours are presented in Fig. 4.28 a and b. As it shows up, only peaks which are assignable to the anatase phase occur in all diffraction patterns. Also all three XANES spectra look like the anatase reference with smeared fine structure due to the superposition with the signal from the remaining amorphous TiO_2. Thus, there is no evidence for the formation of rutile in the composite samples, even in the sample synthesized with alkoxide:HCl ratio of 1:8, which showed rutile concentrations of about 70 weight% in the case of pure TiO_2. Thus, these data provide evidence that the small zirconia concentrations in the TiO_2:ZrO_2=20:1 composite samples are able to stabilize the anatase crystallites with respect to phase transitions.

This is not surprising, because as described before, this zirconia concentration was able to stabilize the crystallite sizes during the annealing process independent on the synthesis path. As was already explained in chapter two, the thermodynamic stability of the different TiO_2 polymorphs is strongly dependent on the particle size. While anatase is the thermodynamically stable phase for small particles up to sizes of about 11 nm, rutile is stable for larger particles. As was observed in the former experiments, the crystalline particle size reached at a certain annealing temperature is dependent on the reaction environment of the powder synthesis, but in all pure TiO_2 samples, the crystallites were able to grow unconstrained. Thus, they are able to reach particle sizes at which the phase transition to rutile is favored energetically. In contrast, the particle size was always observed to stay nearly constant with increasing annealing temperature for the TiO_2:ZrO_2=20:1 composite, thus, the critical size for phase transitions is not reached in the applied temperature range.

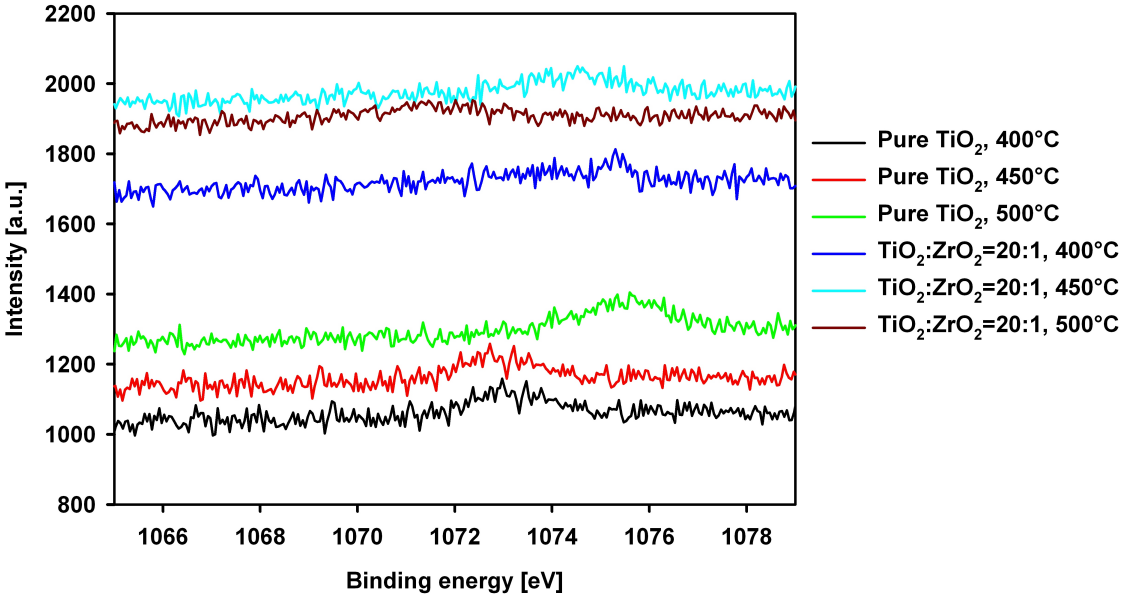

Figure 4.29: XPS spectra of the sodium 1s peak for pure TiO_2 samples and TiO_2:ZrO_2=20:1 composite samples prepared with 1 M sodium hydroxide with alkoxide:NaOH ratio of 1:4. The spectra are shifted vertically for more clarity.

The preparation of transition metal oxides via electrolyte assisted sol-gel process leads to contaminations of the synthesized materials with electrolyte ions [54]. Fig. 4.29 presents the sodium 1s photoelectron peak in the pure TiO_2 and TiO_2:ZrO_2=20:1 composite materials from an annealing temperature of 400°C on. All of the powders were prepared with 1 M sodium hydroxide and annealed for four hours at the stated temperatures. In the samples prepared with different electrolytes, which have not been heat treated, no signals at the binding energies of the belonging Na 1s electron levels could be observed. Thus, because XPS signals always come from material layers at or close to the surface, it can be assumed that the electrolyte ions are included in the material volume and only segregate to the surface when the material is heated. The energy shift in the spectra might be due to difficulties in the determination of the C 1s peak energy resulting from a poor signal to noise ratio even if a large number of spectra is averaged. For the samples prepared with hydrochloric acid and potassium hydroxide, no significant signals due to Cl 2p or K 2p could be observed in the heated samples. However, the cross sections of these elements for the excitation with Mg K_α radiation are substantially smaller than that of the Na 1s peak, thus the signal is expected to be small. In units of the carbon 1s cross section (22.2 barns), the Na 1s cross section is 7.99, that one for Cl $2s_{1/2}$ is 1.48 and that one for K $2p_{3/2}$ is 2.67 [111]. The Na 1s peaks presented in Fig. 4.29 are already very low in intensity. Therefore, the peaks belonging to chlorine and potassium would be even smaller because of the smaller cross sections, if similar amounts of those elements are present in the samples. Thus, there might be contaminations in the samples prepared with hydrochloric acid and potassium hydroxide, but the assigned signals in XPS are below the detection limit. The concentrations of the sodium contaminations are between 3.0 and 5.2%.

As it shows up, the pure titania samples have more sodium included than the composite samples. As was already presented before, the anatase lattice parameters in the composites are broadened due to incorporated zirconium atoms. This less denser structure may allow faster diffusion of the electrolyte ions in the material. Wu et al. [131] prepared anatase TiO_2 samples with hydrofluoric acid and observed fluorine peaks in XPS measurements of samples without calcination treatment. After the heat treatment, these peaks vanished. Thus, the contaminations can be removed from the sample surface by heat treatment. In the composite samples, the faster diffusion, if really occurring, would lead to a fast segregation of the ions to the surface, where they can be removed faster. In the pure titania samples, the amount of sodium remains larger. Nevertheless, in both types of samples, ions due to the preparation medium are in the samples.

Another important point concerning the materials structure is that the crystallites are no isolated, free particles, but are agglomerated to larger structures.

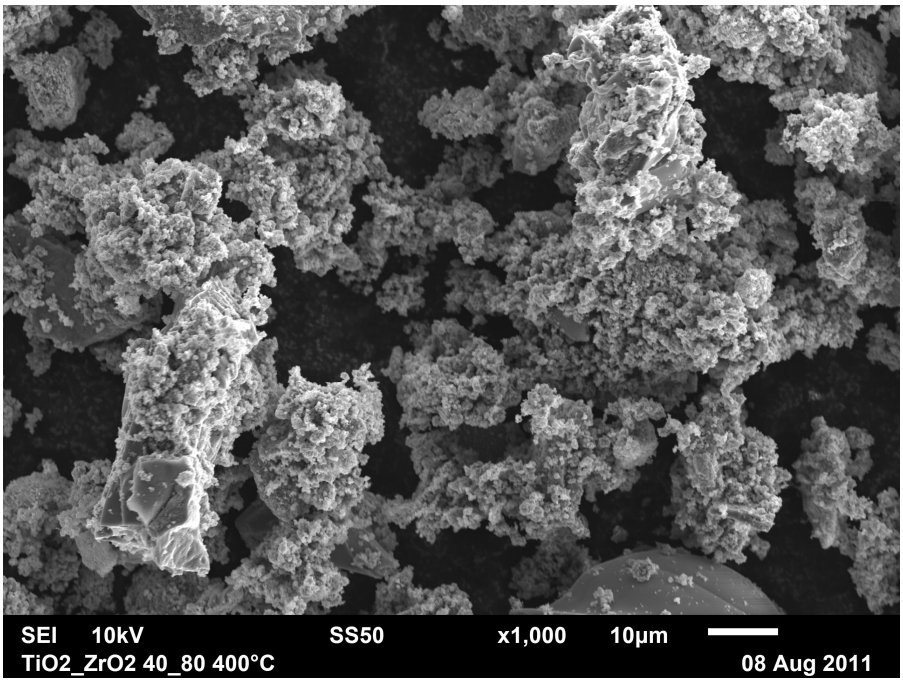

Figure 4.30: SEM image of a composite sample with TiO_2:ZrO_2=20:1 synthesized with a water to alkoxide ratio of 2:1 and annealed at T=400°C.

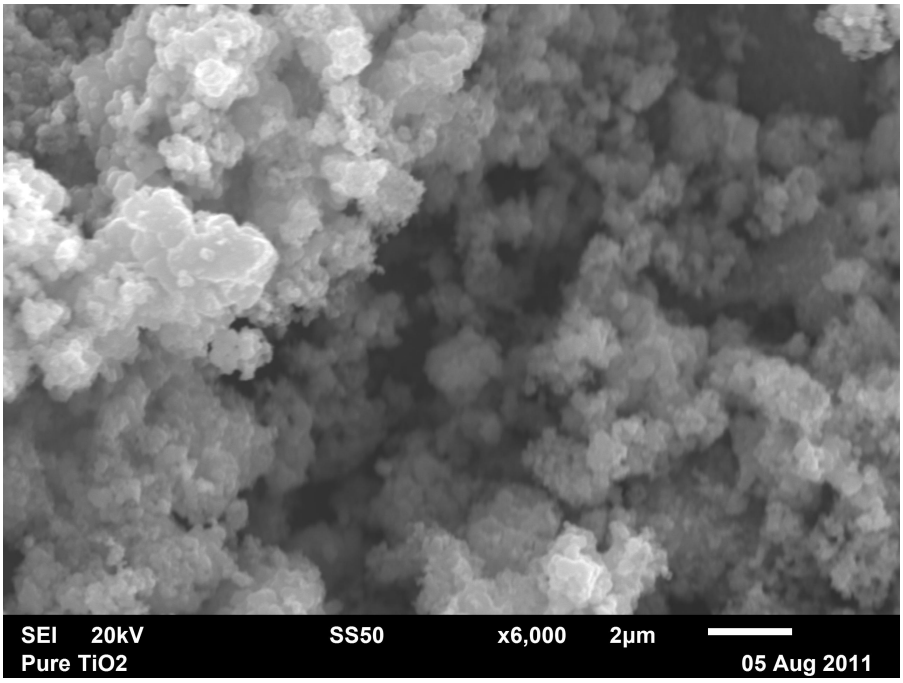

Figure 4.31: SEM image of a pure titania sample prepared with TTIP:water=1:4 at a higher contrast than the picture in Fig. 4.30.

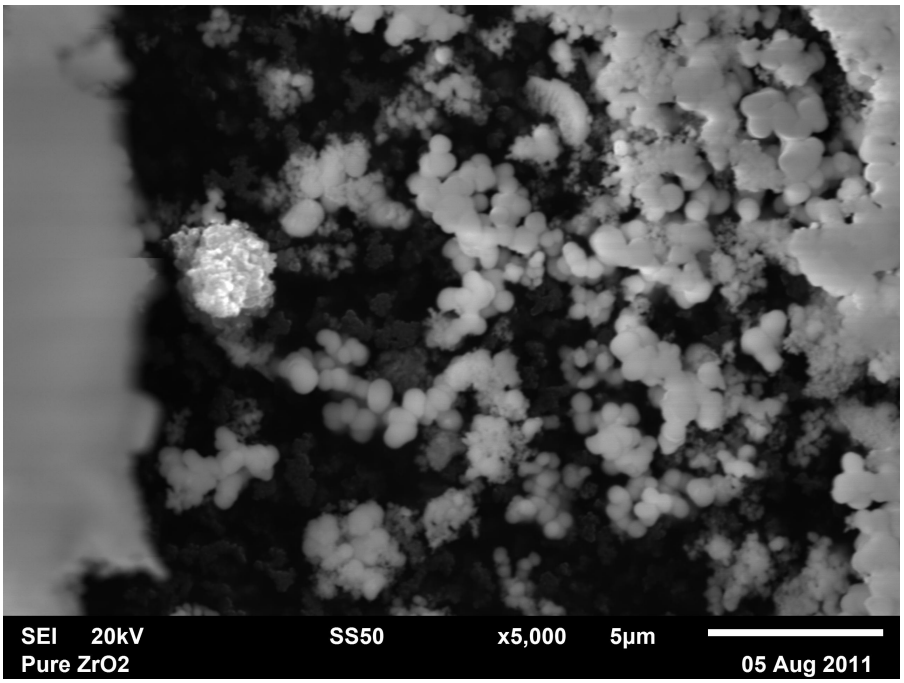

Figure 4.32: SEM image of a pure zirconia sample prepared with ZNP:water ratio of 1:4.

An SEM image presenting the strongly agglomerated structure of a sample with TiO_2:ZrO_2=20:1 synthesized with water to alkoxide ratio of 2:1 and annealed at T=400°C for four hours is presented in Fig. 4.30. The agglomeration is not only important for the specific surface area, but also influences the crystallite size and phase. Shannon and Pask [132] investigated the anatase to rutile transformation kinetics and found that the phase transition to rutile was favored in agglomerated samples, while in samples which were peptized and showed no or only weak agglomeration, large amounts of anatase without rutile formation occurred. Generally, the samples prepared form hydrolysis of TTIP and ZNP are strongly agglomerated if no treatment is performed to avoid. Also pure TiO_2 and ZrO_2 samples show highly agglomerated structures [54], as it shows up in Fig. 4.31 and Fig. 4.32. In contrast to the pure titania and the composite powders, the structure of the zirconia agglomerates shows spherical shapes with much smoother surfaces.

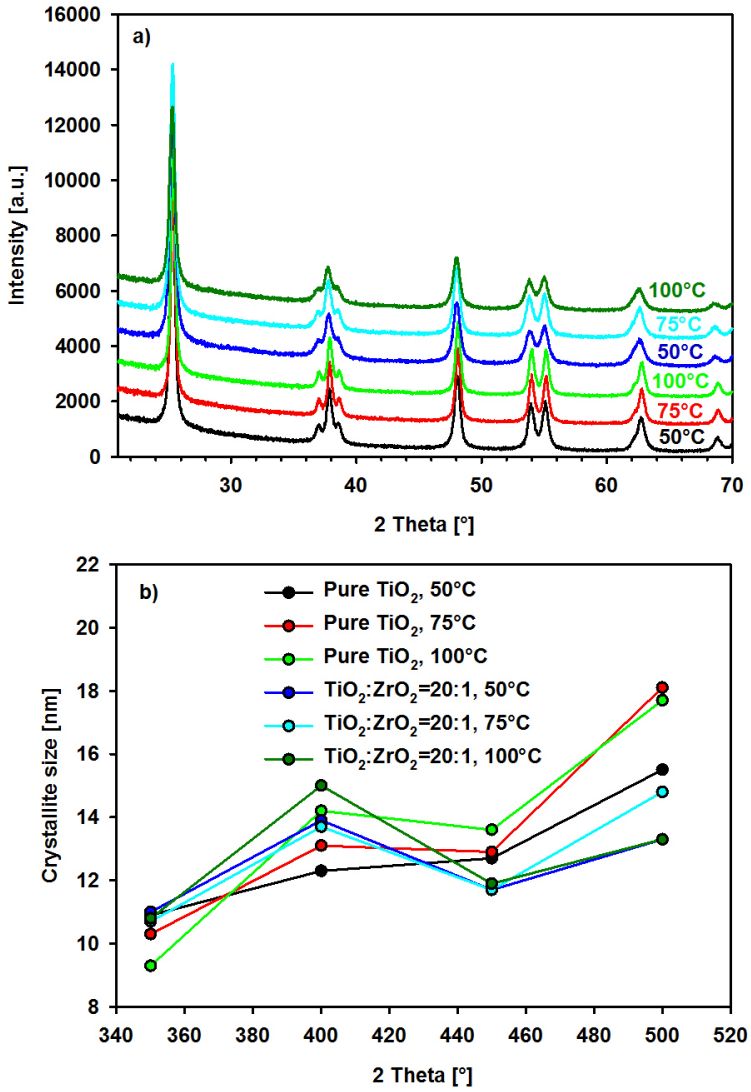

Figure 4.33: XRD patterns of pure titania samples and TiO_2:ZrO_2=20:1 composite samples prepared at different reaction temperatures (part a). Samples were annealed at 500°C for four hours. The diffraction patterns are shifted with respect to each other by 1000 units. The development of the crystallite size with increasing reaction temperature is presented in part b.

In addition to the already presented preparation paths, samples were also prepared at different reaction temperatures. The XRD patterns are presented in Fig. 4.33 a. As can be observed, all samples are only made up of the anatase crystalline phase. The decrease of the background with increasing diffraction angle at angles between 20° and about 40° shows that there are also amorphous fractions remaining in the samples. Due to the fact that the background is parallel between 20° and about 30°, it can be assumed that the amorphous concentrations do not differ largely. The anatase peaks in the three samples of pure TiO_2 are a bit sharper than those ones of TiO_2:ZrO_2=20:1 composite samples, indicating a larger crystallite size in the pure samples, as can be expected with

respect to literature and the results presented above. Part b of Fig. 4.33 presents the development of the crystallite sizes of the pure TiO_2 and composite samples. Crystallite sizes vary between about 9 and 18 nm. In pure titania samples, the crystallites become a bit larger than in the composite samples.

This is a strange result with respect to a former work of the author [54], where it was found that the reaction temperature has a strong influence on the formation of brookite. Namely, in samples prepared at T_{react}=50°C and 75°C, significant brookite formation were found, while this was not the case in samples prepared at room temperature and T_{react}=100°C. At higher annealing temperatures, the brookite leads to the formation of rutile phase, like it is predicted from the theory (compare section 2.4). Also in the case of samples prepared with electrolytes, much more influence of the reaction path on the titania sample structure of pure titania and pure zirconia samples could be observed in [54]. In this work, the influence on the materials structure always has been very small to negligible. The only observed crystalline TiO_2 polymorph always has been anatase, only very small amounts of brookite could be observed in some samples. In the crystallite size, only small changes are observable with respect to the preparation path at a certain annealing temperature. In the case of the pure titania samples prepared with a higher amount of 1 M hydrochloric acid, significant structural changes with respect to other samples could be observed. Also in [54], the samples were prepared with higher water to alkoxide ratios than in the case of this work.

An example of results from this work is presented in Fig. 4.34. Thus, it can be assumed that the possibility to influence the chemical reaction product by the addition of electrolytes or dissolvers or different reaction temperatures is dependent on the amount of added water.

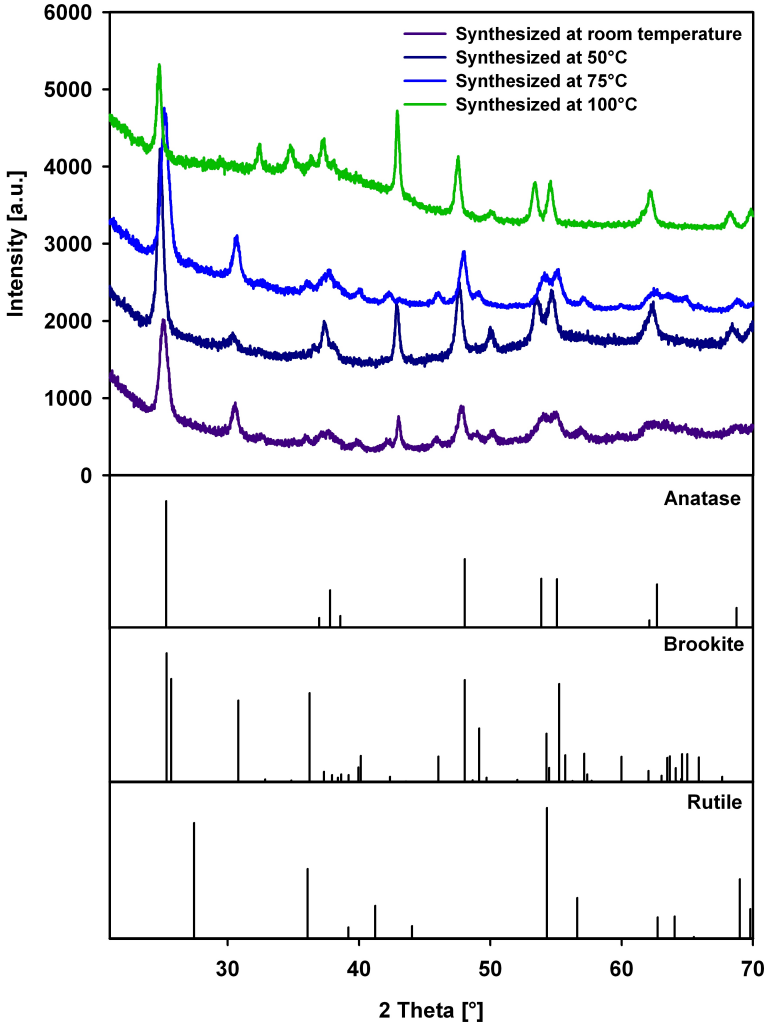

Figure 4.34: XRD patterns of samples prepared with 5 ml TTIP (17 mmol) and 10 ml water (555 mmol) at reaction temperatures between room temperature and 100°C after calcination at 500°C for four hours. The alkoxide to water ratio is about 1:33 in this case. Picture taken from [54]. The diffraction patterns are shifted for more clarity by 1000 units. The calculated reference patterns of anatase, brookite and rutile are presented at the bottom.

4.3.3 Ageing of titania and composite powders during room temperature storage

Powder samples, which were not annealed or otherwise heat treated also show crystallization. After some months of storage at room temperature and ambient conditions, small diffraction peaks show up in XRD patterns. Ageing effects are also observable in the case of crystalline samples after storage.

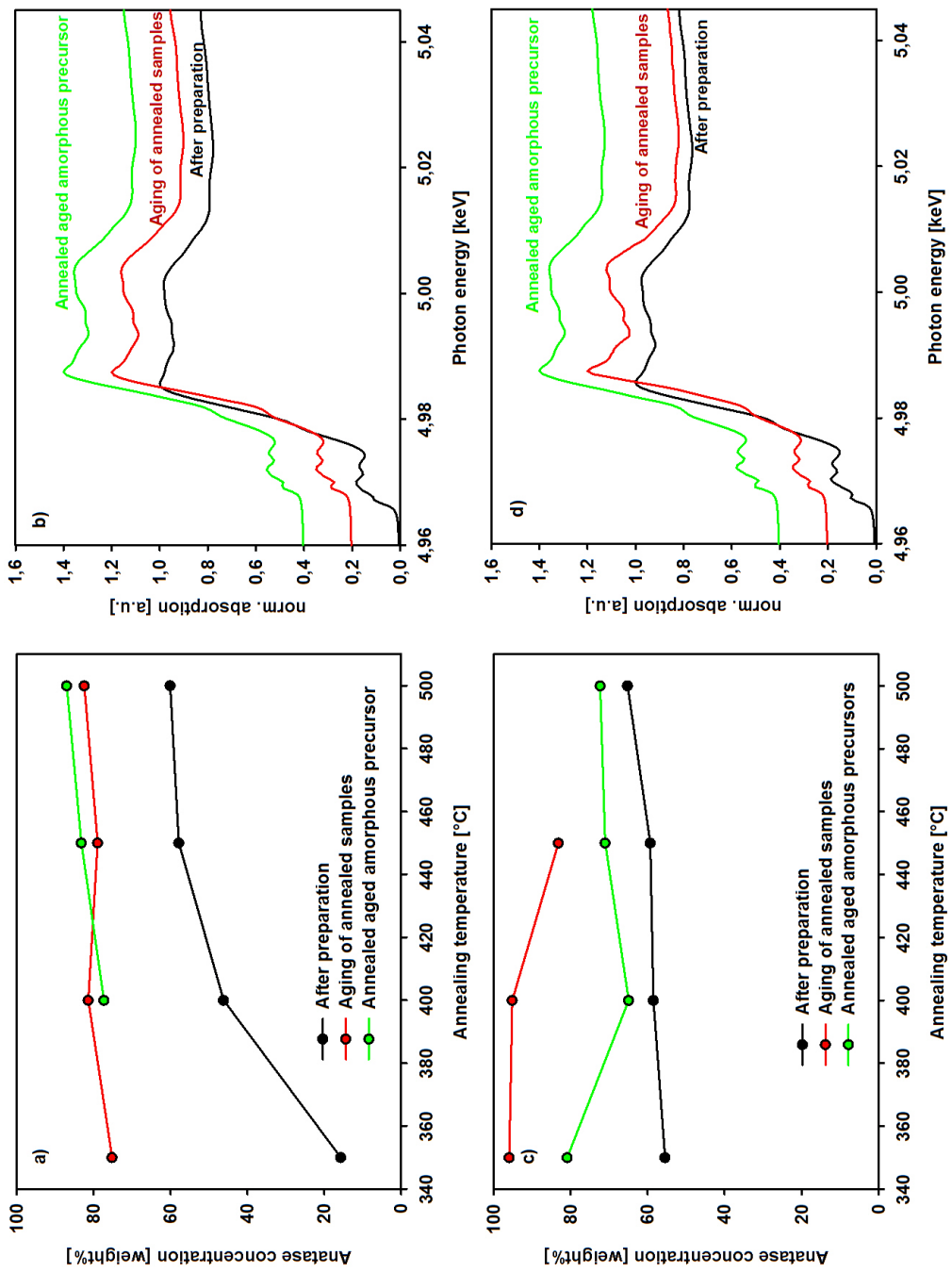

Figure 4.35: Fit results of LC-XANES investigations of TiO_2:ZrO_2=10:1 and pure titania shortly after preparation (black line), after ageing of the crystallized samples (red line) and of powders prepared by annealing of aged untreated precursors (light green line). All samples were annealed at 400°C for four hours. Figures a and b presents the results for pure titania, c and d those for the composite. The XANES spectra are shifted with respect to each other by 0.2 units.

The pure titania samples and the composite samples with TiO_2:ZrO_2=10:1 were measured shortly after preparation and again after about 13 months to examine the possible influence of ageing effect on the materials structure. The results of the LC-XANES fits of these measurements with the results of the same samples measured shortly after preparation are presented in Fig. 4.35. As it shows up, the spectra which were measured shortly after the sample preparation have less sharp anatase features than those ones which were measured after ageing in both pure titania and the composite samples. The sharpest and best pronounced anatase features can be observed for the powders annealed a short time after their preparation and stored for 13 months for both sample systems. The samples prepared from annealing of the aged amorphous powder precursors are more crystalline than those annealed shortly after preparation, and approximately as crystalline as the one aged after crystallization in the case of the composite. In the case of pure TiO_2, the crystallinity of the sample prepared from the aged amorphous precursor is smaller than that of the aged crystalline material. The crystallite sizes in the composite samples do not or only very slightly change during storage for six months in the composite as well as the pure titania samples at all annealing temperatures [133].

The XAS measurements of the powders shortly after the preparation process were measured at beamline C at the DORIS III storage ring. The aged samples were measured at beamline A1 at the same facility. The observable shift between the absorption edges might be due to the measurement at different build-ups. There is no reason to assume a shift due to changes in the chemical valence of the titanium absorbers.

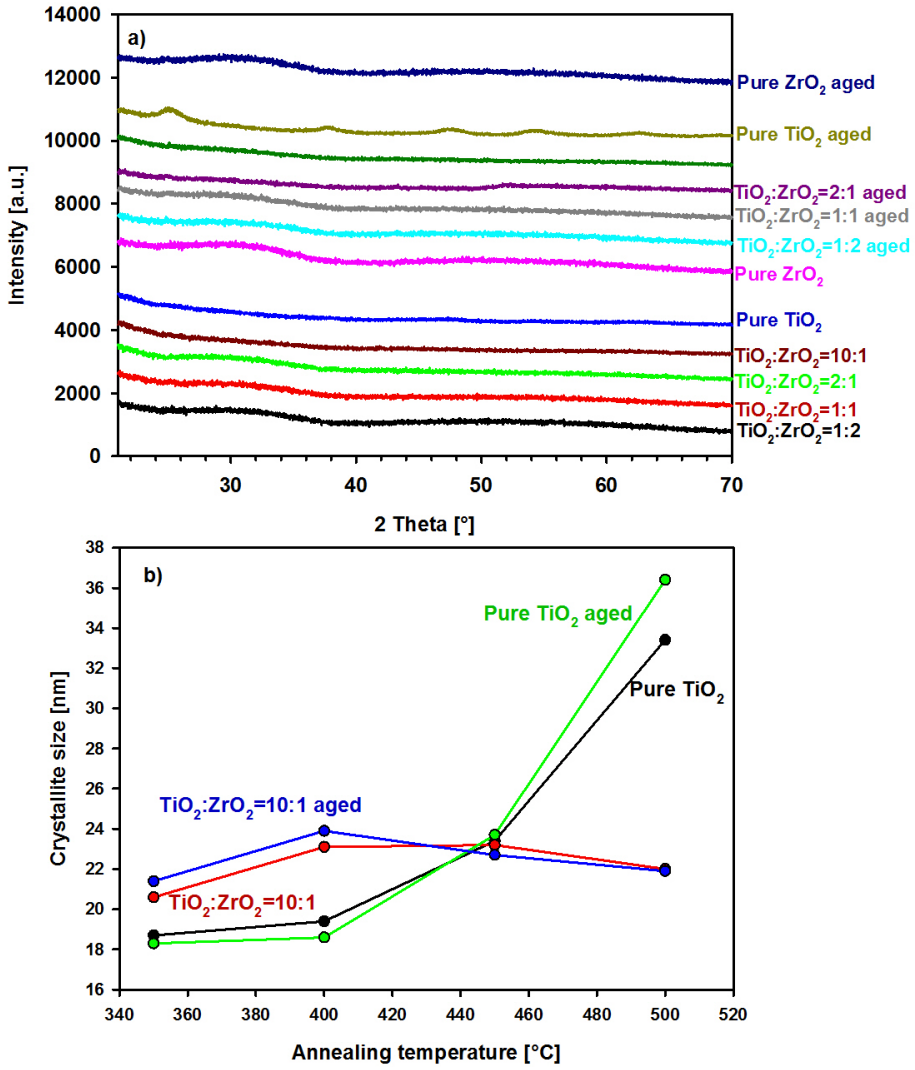

Figure 4.36: Diffraction patterns of powder samples of pure TiO_2 and ZrO_2 as well as composite samples with different TiO_2:ZrO_2 ratios (part a). None of the samples had been heat treated. Diffraction patterns of powders measured shortly after the synthesis are presented next to those ones aged for six months. Part b presents the results already presented in Fig. 4.9 for the particle sizes of the pure titania and TiO_2:ZrO_2=10:1 samples annealed after their preparation for four hours in comparison to those ones of samples stored six months after preparation and annealing. Storage took place at room temperature in ambient conditions.

XRD patterns of the untreated samples (no annealing), six months after their preparation, are presented in Fig. 4.36. As can be seen, all samples are amorphous shortly after their preparation, as was already presented at the beginning of this chapter. After six months of ageing at room temperature, the XRD pattern of the pure titania sample presents weak diffraction peaks assignable to the anatase phase. The zirconia addition thus not only suppresses the crystallization due to heat treatment, but also that one of

room temperature ageing. This is difficult to explain in the picture of encapsulation of the titania in the zirconia matrix because in a capsule, surrounding a titania domain, it should be possible for the titania to crystallize. It might be possible that the heat treatment allows the zirconia or O-Ti-O-Zr-O bond areas to diffuse, allowing the formation of larger titania domains, which then can undergo amorphous-anatase phase transition.

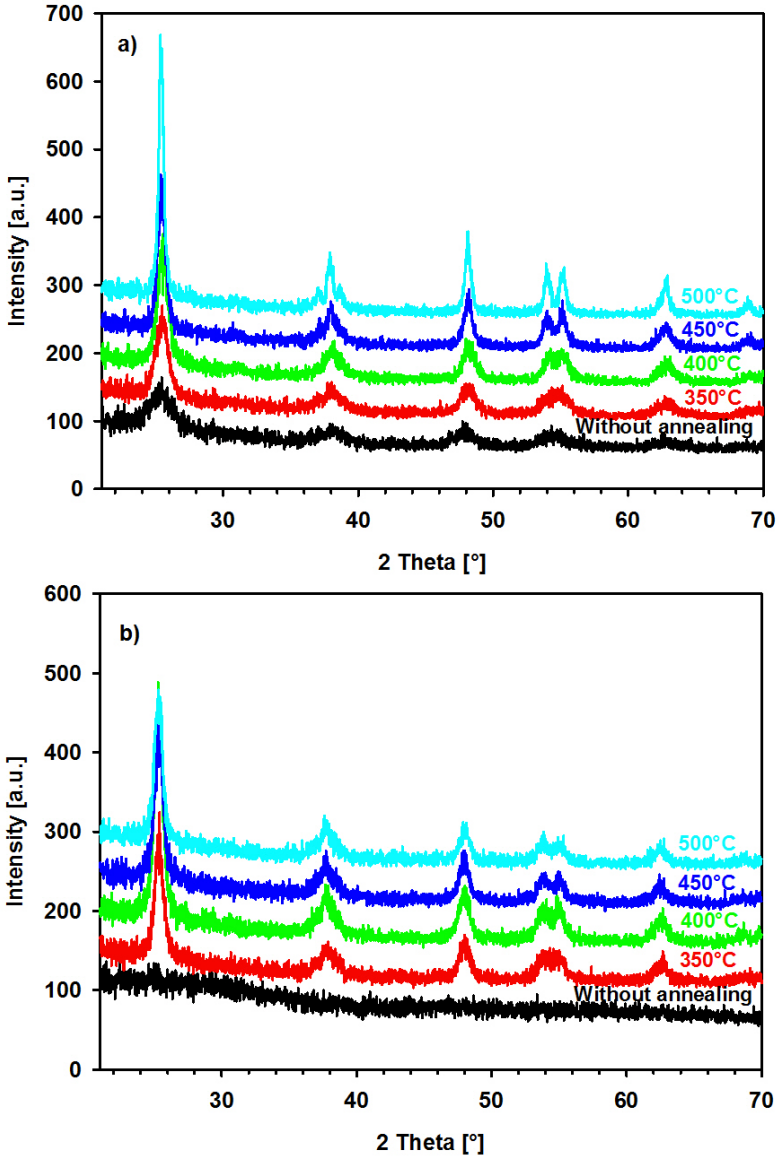

Figure 4.37: XRD patterns of pure titania (part a) and TiO_2:ZrO_2=10:1 (part b). The samples were obtained from ageing of the amorphous powders for 13 months and annealing of these aged powders for four hours at the stated temperatures.

Fig. 4.37 presents diffraction patterns of pure titania and TiO_2:ZrO_2=10:1 composite samples after ageing for about 13 months and annealing at temperatures between 350°C and 500°C for four hours. As can be seen, anatase diffraction lines are observable for

all diffraction patterns in the measurements of pure titania powders. In the case of the composites, only the measured patterns of the annealed samples show anatase diffraction lines. The peaks in the patterns of the pure titania samples are sharper than those ones of the composites, indicating larger crystallite sizes. In none of the diffraction patterns, other diffraction lines than those ones assignable to the anatase phase are observable.

As already mentioned, the amorphous fractions determined from the LC-XANES fits can be due to parts of the materials without long-range order as well as from the surfaces of the crystallites/agglomerates. Thus from these results it could be suggested that small particles in the samples might grow to larger ones during the storage, causing a reduction of the surface fractions of the samples or that small amorphous fractions of the samples crystallized during storage.

As can be seen till this point, the used characterization methods can provide a lot of the structural characteristics which are important for many nano-TiO_2 applications. XRD and LC-XANES measurements reveals information about the crystallinity and crystallite size of the samples. It shows up that samples in a certain class of samples are very similar to each other. A class of samples is all samples prepared in a certain reaction path (all samples prepared with alcohol dilution, all samples prepared with different water to alkoxide ratios, to give two examples).

4.4 Investigation of surface structures with GISAXS

In many applications, titania based nanomaterials are used as thin films/coatings, which is often better for the handling. For many applications like catalysis, the most important effects take place on the sample surface. In this section, GISAXS measurements and their results are presented for coatings made of the powders investigated in the sections before.

As can be seen from Fig. 4.38, the scattering curves consist of two peaks, the first one at about $0.06\,nm^{-1}$ belongs to the agglomerates, the second one at about $0.8\,nm^{-1}$ to the smallest particles [134]. The first minimum, necessary for the determination of the structure size, is very blurred and thus difficult to determine. The presented scattering curves of composite samples prepared with different amounts of propanol in the reaction step show a structure of two peaks for the sample prepared with 5 ml propanol. For the samples prepared with 15 ml and 25 ml propanol, the scattering curves show a comparably low intensity at high q values. Thus, only the peak belonging to the agglomerates is clearly visible. The first minimum at about q=$0.1\,nm^{-1}$ becomes more blurred with increasing amounts of alcohol added. Thus, the size distribution of the particles in the precipitate becomes broader with incrementing alcohol dilution.

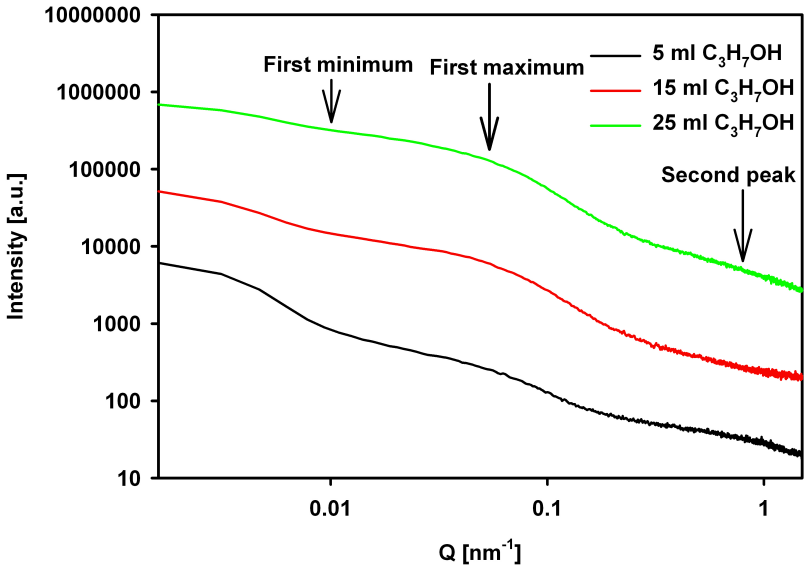

Figure 4.38: GISAXS scattering curves of composite samples with TiO_2:ZrO_2=20:1 without annealing.

Sample	Preparation	Peak width [10^{-2} nm^{-1}]	Structure size [nm]
TiO_2:ZrO_2=20:1	Alkoxide:H_2O=1:4	11.56, 2.41	280.81
TiO_2:ZrO_2=20:1	1 M KOH	8.36	449.30
TiO_2:ZrO_2=20:1	1 M HCl	5.43	408.46
TiO_2	5 ml C_3H_7OH	9.68	561.63
TiO_2:ZrO_2=20:1	5 ml C_3H_7OH	1.34	345.62
TiO_2:ZrO_2=20:1	15 ml C_3H_7OH	10.20	561.63
TiO_2:ZrO_2=20:1	25 ml C_3H_7OH	9.81	499.22

Table 4.1: Results of the analysis of the GISAXS scattering curves of the powder samples without annealing treatment. In most cases, the second peak could not be fitted due to the large width and the hardly pronounced peak structure.

In Table 4.1, the results of the GISAXS experiments are presented for samples which had not been annealed after preparation with respect to the structure size and the polydispersity. The structure sizes determined from the positions of the first minimum of the scattering curves are only very rough approximations, due to the difficult determination of the first minimum in the scattering curves, which are strongly influenced by the peak broadening due to the high polydispersity of the samples. Secondly, Eq. 2.33 is only an approximation for the structure size. Due to the rough determination of the minimum, small differences in the positions of the minima could not be distinguished. Thus, the minima position seems equal, which is why some structure sizes occur more often.

As can be seen from a comparison of the samples of pure titania and the composites prepared with 5 ml propanol, the composite has a much broader peak than the pure titania sample, indicating that the composite has a broader particle size distribution.

The size of the agglomerates is much larger for the pure titania sample. The preparation of the composite sample with KOH leads to broader particle size distribution than in the sample prepared with HCl. Also the structure size is a bit larger. This might be due to a peptization of the formed agglomerates in the preparation step due to the added acid. It is also known that the addition of bases in the sol-gel process leads to crosslinked structures, while the addition of acids leads to chain like structures [44]. With different degrees of linkage, the base addition might in this way lead to more polydisperse structures. As could already be seen visibly in the scattering curves of composite samples prepared with different amounts of added alcohol, the polydispersity increases with increasing amounts of alcohol. The addition of pure water leads to a very broad particle size distribution compared to those ones of the other samples. This might be due to the missing of reagents in the condensation step which slow down the fast agglomeration or adsorb on the particle surface, leading to repulsive forces that suppress fast coagulation. On the other side, the addition of alcohol should slow down the coagulation process, but the size distribution seems to become broader with increasing amount of added alcohol.

Table 4.2 presents an overview of the GISAXS results of the powder samples after annealing at an annealing temperature $T_{annealing}$. Again, the peak broadening is in most cases larger for the composites, if compared to pure titania samples prepared in the same manner. No trends of the particle size distribution are observable with respect to annealing temperatures or additives. It is obvious in the structure sizes of samples prepared under addition of electrolytes that they have comparably small structure sizes, which might be due to peptization processes occurring during preparation and drying of the samples. Peptization means that large agglomerates of particles are broken down to small agglomerates or isolated particles [135].

Sample	Preparation, T [°C]	Peak width[10^{-2} nm^{-1}]	Size[nm]
TiO_2:ZrO_2=20:1	15 ml C_3H_7OH, 500	1.15	641.86
TiO_2:ZrO_2=20:1	25 ml C_3H_7OH, 500	11.23, 2.34	408.46
TiO_2:ZrO_2=20:1	Alkoxide:H_2O=1:2, 500	1.43, 1.19	499.22
TiO_2:ZrO_2=20:1	Alkoxide:1 M HCl=1:2, 500	15.34, 16.30	449.30
TiO_2:ZrO_2=20:1	Alkoxide:1 M HCl=1:8, 500	1.85, 7.46	449.30
TiO_2:ZrO_2=20:1	Alkoxide:H_2O=1:2, 500	1.57	561.63
TiO_2:ZrO_2=20:1	Alkoxide:H_2O=1:8, 500	11.12, 8.61	641.86
TiO_2:ZrO_2=20:1	Alkoxide:H_2O=1:20, 500	1.45	449.30
TiO_2:ZrO_2=20:1	5 ml C_3H_7OH, 500	4.56	449.3
TiO_2:ZrO_2=20:1	1 M KOH, 500	5.22, 4.20	280.81
TiO_2:ZrO_2=20:1	1 M NaOH, 500	2.38	280.81
TiO_2:ZrO_2=20:1	1 M HCl, 500	4.70	320.93
TiO_2:ZrO_2=20:1	25 ml C_3H_7OH, 450	10.06	499.22
TiO_2:ZrO_2=20:1	25 ml C_3H_7OH, 400	11.26	499.22
TiO_2:ZrO_2=20:1	15 ml C_3H_7OH, 400	11.13	499.22
TiO_2:ZrO_2=20:1	Alkoxide:H_2O=1:8, 350	12.98	499.30
TiO_2:ZrO_2=20:1	Alkoxide:H_2O=1:8, 400	12.40	499.22
TiO_2:ZrO_2=20:1	Alkoxide:H_2O=1:8, 450	4.15	499.22
TiO_2:ZrO_2=20:1	Alkoxide:H_2O=1:20, 350	2.80	499.30
TiO_2:ZrO_2=20:1	Alkoxide:H_2O=1:20, 400	11.35	408.46
TiO_2:ZrO_2=20:1	1 M HCl, 450	82.29	249.61
TiO_2:ZrO_2=20:1	1 M NaOH, 450	1.76	195.35
TiO_2:ZrO_2=20:1	1 M KOH, 450	8.64	374.42
TiO_2	1 M HCl, 450	3.56	179.72
TiO_2	Alkoxide:H_2O=1:2, 500	1.13, 1.54	236.474
TiO_2	Alkoxide:H_2O=1:8, 500	2.65, 2.97	408.46
TiO_2	Alkoxide:1 M HCl=1:2, 500	5.25, 7.80	374.42
TiO_2	5 ml C_3H_7OH, 500	9.57, 11.31	561.63
TiO_2	15 ml C_3H_7OH, 500	4.99, 5.61	299.53
TiO_2	1 M KOH, 500	4.13	280.81
TiO_2	1 M NaOH, 500	8.10	320.93
TiO_2	1 M HCl, 500	1.67	320.93

Table 4.2: GISAXS results of the annealed titania and composite samples. For some measurements, only one peak could be fitted.

Sample	Preparation	Width [10^{-2} nm^{-1}]	Size[nm]	Width powder	Size powder
TiO_2	15 ml C_3H_7OH	12.04	561.63	4.99, 5.61	299.53
TiO_2	5 ml C_3H_7OH	3.18, 5.45	345.62	9.57, 11.31	561.63
TiO_2-ZrO_2	5 ml C_3H_7OH	2.80	408.46	4.56	449.3

Table 4.3: GISAXS results of samples grown as thin films. The results of powders prepared in the same way are presented for comparison. All samples had been annealed for four hours at T=500°C.

In Table 4.3, the GISAXS results of samples annealed as coatings on float glass substrates are presented. The results for the powder samples prepared in the same manner are presented for comparison. In this case, the particle size distribution of the three samples seems to be smallest for the composite sample. In the special case of the presented preparation methods, this is also true for the powder samples. Again, there seems to be no trend of the particle size distribution or the structure size with the preparation method, or a general difference between film and powder preparation. The surface structures of the samples may be influenced by other factors like drying, the dilution of the samples in propanol, ect. Also, the sample surface may be influenced by statistical factors like alignment of the samples on the substrates.

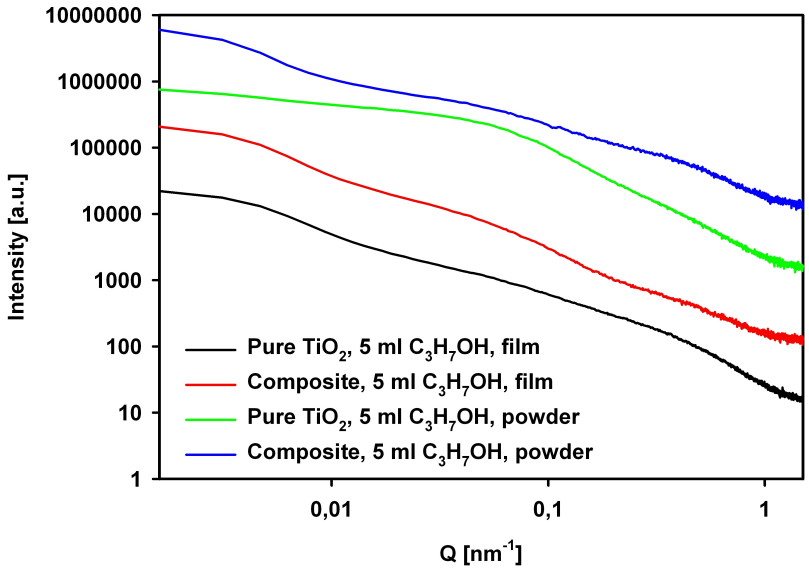

Figure 4.39: GISAXS patterns of the pure titania and composite samples prepared with 5 ml propanol and annealed at 500°C for four hours grown in film structure and samples prepared in the same manner as powders.

From the scattering curves in Fig. 4.39, it can be seen that there is a difference in the surface structure for samples crystallized in powders and those ones crystallized as thin films. In the pure titania samples, the first peak is more pronounced in the powder sample, the second one in the film. In the composite sample, the effect is opposite, the first peak is more pronounced in the film.

The differences might be due to different agglomeration of the structures, but it may also be due to the differences in the preparation of the coatings of powder and film samples, compare section 3.1.

Up to this point, it could be seen that the used investigation methods provided much information about the prepared samples. Composite samples tend to have large differences in their crystallinity in dependence on the amount of zirconia with respect to the titania content. Also the reaction chemistry has an influence on the materials structure. For example, it could be observed that the samples prepared in water had another degree of crystallinity and another crystallite size than the ones prepared with alcohol dilution. Especially the amount of added hydrochloric acid has a strong influence on the material structure of pure titania samples. The formation of the rutile phase could be observed in pure titania samples prepared with TTIP:HCl ratio of 1:8. In contrast, a

composite sample with TiO_2:ZrO_2=20:1 prepared in the same way and annealed at the same temperatures do not show any features assignable to the rutile phase in XANES as well as XRD. The addition of zirconia to the materials has a small influence on the polydispersity of the particles.

4.5 Photocatalytic activity of the titania and composite samples for methylene blue degradation

Photocatalysis is one of the most important applications for titania based nanomaterials. In the following investigations, the degradation of methylene blue is presented as an example of a possible application. The methylene blue solution is mixed with the prepared powder samples in cuvettes. For the decomposition, the mixture of the powders and the solution is irradiated with UV radiation under an exposure unit. A pure methylene blue solution without a catalyst was irradiated and examined to investigate possible reactions occurring independent from the catalyst. For the examination of the reaction, optical absorption spectroscopy was used. The decomposition of methylene blue leads to clear aqueous solutions including different mineral acids. Thus, the decolorization can be followed to investigate the reaction. The photocatalytic activity is connected to the structural parameters presented in the former chapters.

4.5.1 The methylene blue reagent

Methylene blue is used in many chemical and biological applications. The international union of pure and applied chemistry (IUPAC) name of methylene blue is 3,7-bis (dimethylamino)-phenothiazin-5-ium chloride and it has the chemical formula $C_{16}H_{18}N_3SCl$.

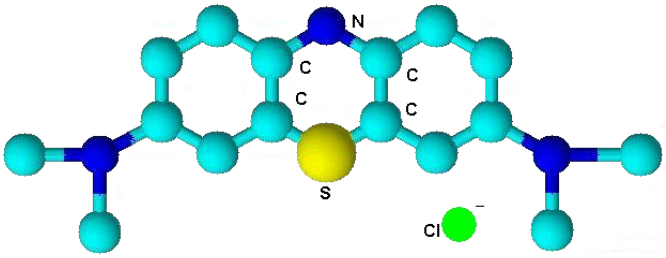

Figure 4.40: Molecular structure of the methylene blue molecule.

The methylene blue molecule is presented in Fig. 4.40. It is used in the industry as a dye for the colorization of fibers [136], and in chemical laboratories as indicator reagents [137], in biology as an in vitro coloring and also in medicine and veterinary [136]. Methylene blue is harmful to human health and toxic for inshore waters.

4.5.2 Decomposition of methylene blue over pure TiO_2 and TiO_2-ZrO_2 composite nanopowders

For the investigation of the catalysis of methylene blue decomposition over different pure titania and composite catalysts, cuvettes with methylene blue solution are prepared as explained in section 3.6. The cuvettes are irradiated with UV radiation under a turned UV exposure unit. Optical absorption is measured after 10 minute intervals.

Methylene blue can be oxidized photocatalytically over TiO_2 catalysts. In the concrete form of Eq. 2.1 the decomposition of methylene blue is given by [7]

$$2 \cdot C_{16}H_{18}N_3SCl + 51 \cdot O_2 \rightarrow 32 \cdot CO_2 + 12 \cdot H_2O + 2 \cdot HCl + 6 \cdot HNO_3 + 2 \cdot H_2SO_4. \quad (4.1)$$

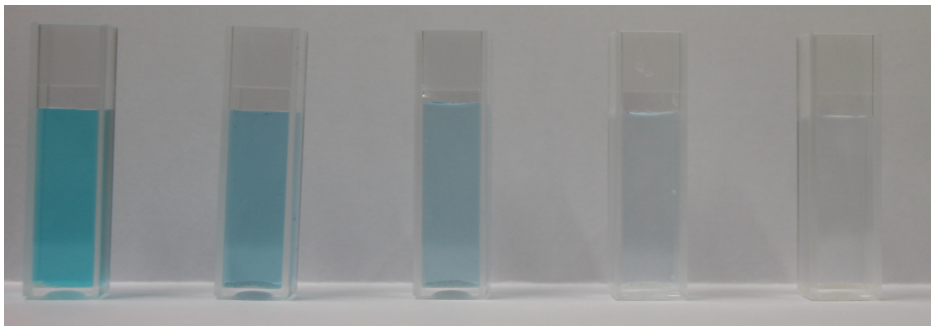

Figure 4.41: Cuvettes including aqueous methylene blue solutions with the titania catalyst prepared with a water to alkoxide ratio of 4:1, annealed at 500°C for four hours. The first cuvette was not irradiated, the following ones with time differences of 30 minutes. A significant de-colorization is observable.

Fig. 4.41 presents cuvettes filled with aqueous methylene blue solutions and a pure titania precursor annealed at T=500°C for four hours. The first cuvette was not irradiated, the other ones are irradiated with UV radiation for 30-120 minutes, with time differences of 30 minutes. As can be seen, the solution decolorizes with increasing irradiation time due to the formation of the transparent, colorless reaction products. For the used catalyst, the solution is totally colorless after 120 minutes.

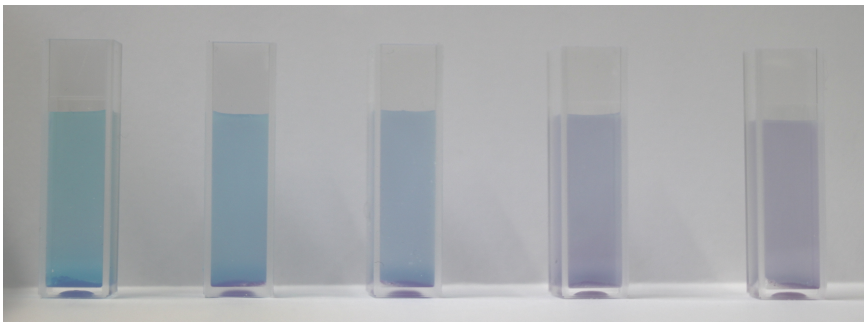

Figure 4.42: Cuvettes with aqueous methylene blue solutions and a pure titania catalyst prepared with 1 M potassium hydroxide. Instead of the de-colorization observed for other catalysts, there is a color change of the solution from blue to violet. The time difference between the presented cuvettes is 5 minutes, the first cuvette was not irradiated.

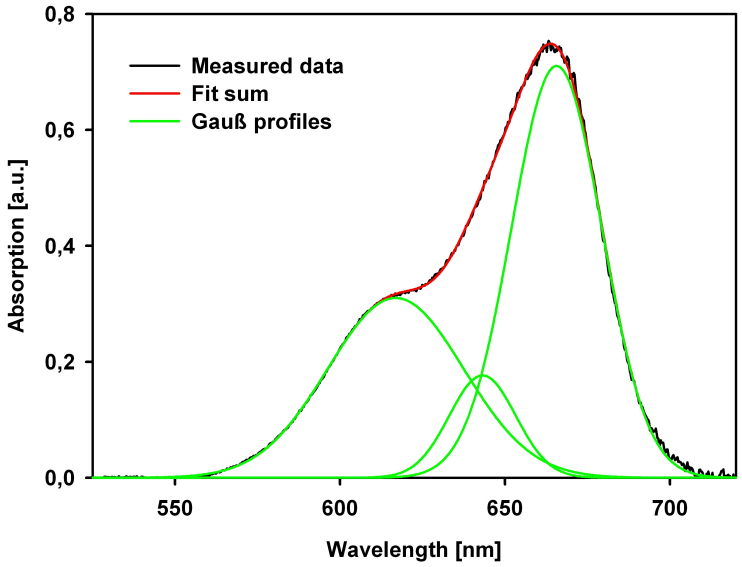

Figure 4.43: Example of a data fit of a methylene blue absorption spectrum with three Gauß profiles.

For the determination of the peak intensities, the absorption data are fitted with Gauß-shaped peaks. Three peaks were found to be necessary for the fit sum to describe the data properly. A fit example is presented in Fig. 4.43.

The samples prepared with basic electrolytes showed up to be a special case. After the addition of the catalyst powder to the methylene blue solution, a color change to a slightly violet blue is observable. After UV irradiation of these solutions, the solutions became violet. This is presented in Fig. 4.42 for a pure titania catalyst. Another important point is that the decomposition reaction is much faster with these catalysts. Due to that reason, the irradiation time difference is chosen much smaller. In Fig. 4.42, the time difference is five minutes.

For a good time resolution, the time difference of irradiation and measurement is set to two minutes for the samples prepared in a basic reaction environment. The decomposition times are much smaller than all decomposition times of samples with pure titania or composite catalysts prepared without basic electrolytes. As presented in section 4.3.2, these samples consisted of anatase with residual amorphous titania, with particle sizes comparable to many other samples presented in this work. Thus, the strong increase in catalytic activity cannot be explained with respect to structural parameters, but must have chemical reasons due to residual base atoms in the samples. Evidence for these residues were presented in section 4.3.2 in XPS measurements. In this context, it must be mentioned that it is already known that the addition of bases to aqueous solutions of methylene blue and titania catalyst leads to a better adsorption of the methylene blue molecules on the titania catalyst due to changes of the electrochemical double layer of the titania [138]. The remaining base anions from the catalyst preparation step might cause a thin film of liquid hydroxide on the catalyst. This would fit to the observation, that the catalysts prepared with basic reaction environments show a thin, intense violet layer on the catalyst surface of the titania powder on the floor of the cuvette, see Fig. 4.42. On the other side, it has to be mentioned that the samples still had a slightly violet color, even after the methylene blue peaks in the optical absorption

spectra have vanished. Thus, the samples were not decomposed to carbon dioxide, water and the mineral acids completely. The violet color might have two possible reasons. Methylene blue is used as an indicator for acids and bases. Thus, the violet color might be due to residual alkaline contaminations in the catalysts or due to acids built in the catalysis reaction. As can be seen in Fig. 4.41, no color change from blue to violet can be observed for samples prepared without bases, thus the color change should not be due to the acid molecules but to the bases.

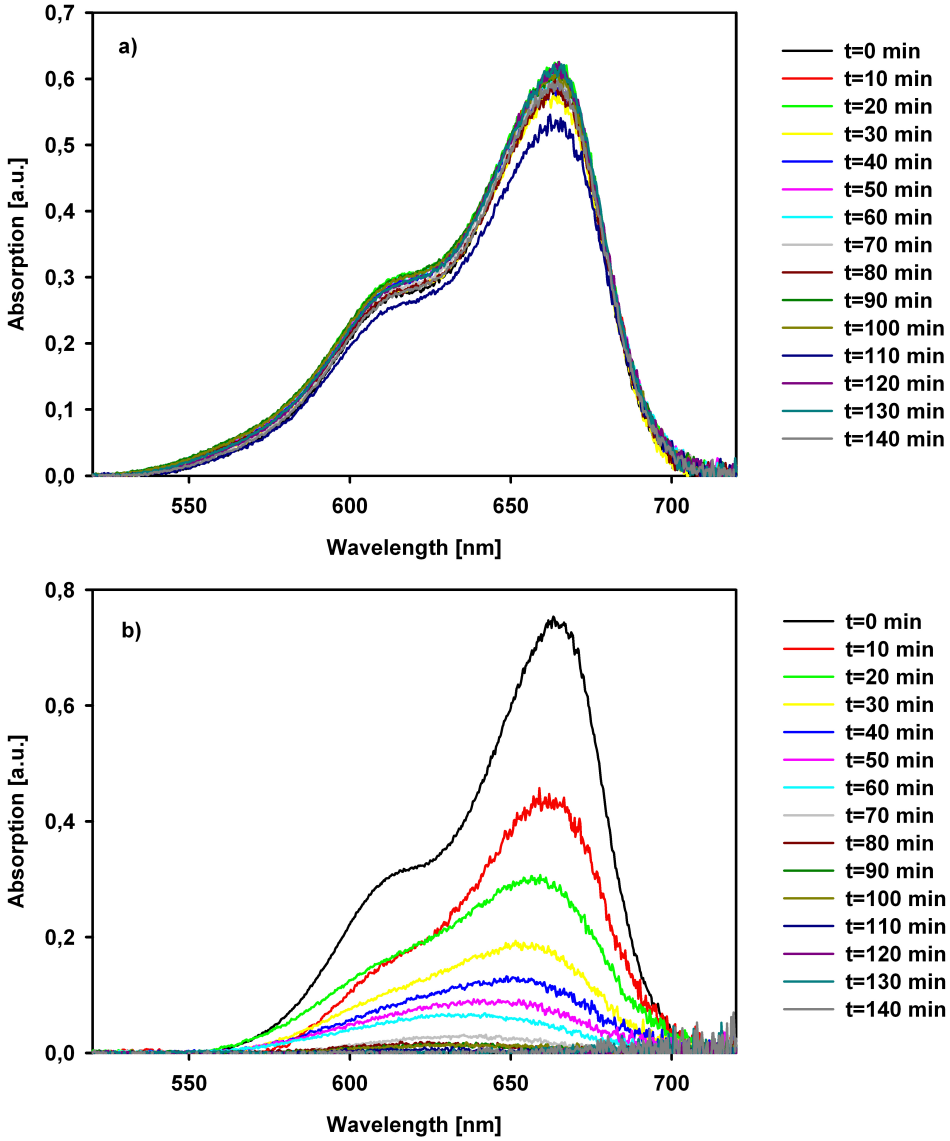

Figure 4.44: Optical absorption spectrum of methylene blue without (part a) and with (part b) a titania catalyst. The titania catalyst was the same as in Fig. 4.41. As can be seen, methylene blue itself is stable to UV radiation. In part b, it shows up that the methylene blue is decomposed after UV irradiation.

To ensure that the observed decrease of the methylene blue concentration is due to the photocatalysis over the powder samples and not to an effect of methylene blue decomposition without a catalyst, a cuvette with a solution without catalyst powder was irradiated parallel to those ones with catalyst powder. The result is presented in Fig. 4.44 a. As can be seen, there is no trend to an intensity decrease with increasing irradiation time. In part b, the absorption signals are presented for a solution with a catalyst. It shows up that the signal clearly decreases with increasing irradiation time.

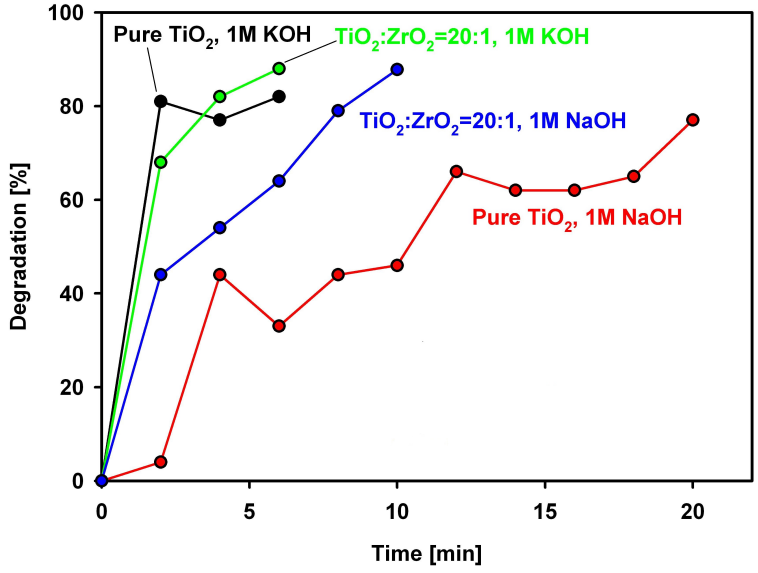

Figure 4.45: Degradation of methylene blue in dependence of the irradiation time. The degradation is faster for the samples prepared with potassium hydroxide. The used base is more important for the activity than the zirconium addition.

The degradation was calculated from equation 3.1. The time dependent degradation of methylene blue over the four catalysts reaction media is presented in Fig. 4.45. As it shows up, the catalysts prepared with potassium hydroxide lead to faster degradation than those ones prepared with sodium hydroxide. In the case of the samples prepared with sodium hydroxide, the composite catalyst leads to the faster degradation rate. In case of the catalysts prepared with potassium hydroxide, there is no significant difference between the degradation for the pure titania catalyst and the composite one.

In the data, there are some fluctuations of the degradation in dependence of the irradiation time. These might be due to background subtraction and additionally to fluctuations in the intensity of the torchlight used as light source in the absorption measurements.

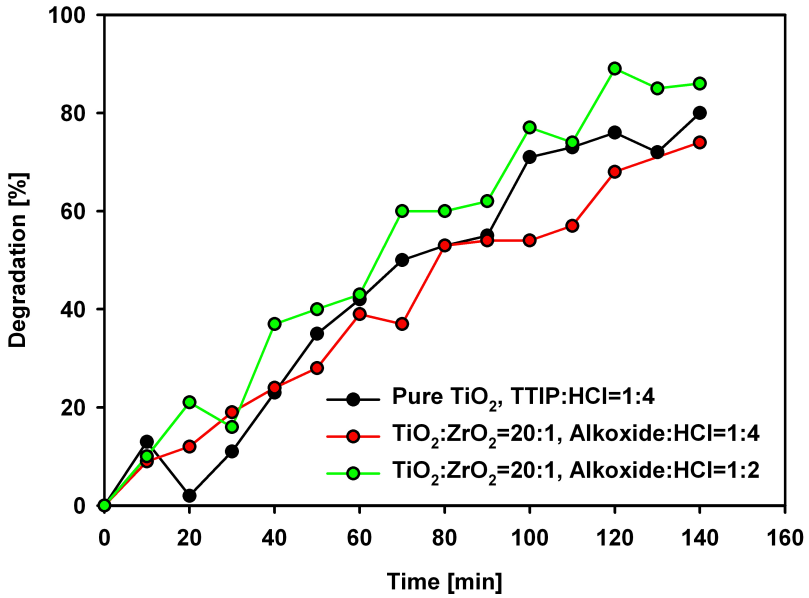

Figure 4.46: Development of the degradation of methylene blue with time for three samples prepared with hydrochloric acid. All catalysts were annealed at 500°C.

The catalysts prepared with hydrochloric acid medium do not show the great enhancement in catalytic activity observed for those ones prepared with basic reaction media. The degradation of the methylene blue with increasing irradiation time over the catalysts prepared in hydrochloric acid is presented in Fig. 4.46. As can be seen, the catalytic activity is again higher for the pure titania catalyst, resulting in a higher degradation than that one observed for the composite sample. The highest activity of a catalyst in this picture is that one of the composite prepared with a smaller amount of acid. Thus, the addition of acid is detrimental for the preparation of a high activity titania catalyst. This point will be discussed in more detail in the next section.

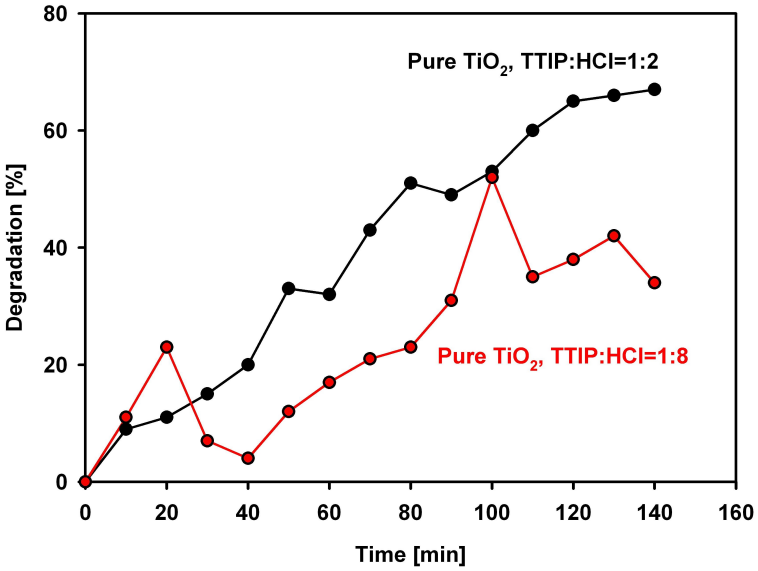

Figure 4.47: Development of methylene blue degradation over pure TiO_2 catalysts prepared with different amounts of hydrochloric acid. One catalyst was prepared with TTIP:HCl=1:2 (black line) and one with TTIP:HCl=1:8 (red line). Both catalysts have been annealed at 450°C for four hours.

Fig. 4.47 presents the degradation of methylene blue for two pure titania catalysts prepared with different amounts of hydrochloric acid and annealed at 450°C for four hours. Again, the catalyst prepared with the lower amount of hydrochloric acid has the higher photocatalytic activity. In the case of the second catalyst, hardly 50% of the methylene blue in the solution is decomposed in the regarded time range. The first catalyst decomposes more methylene blue, after 140 minutes, about 70% of the reagent was decomposed. The first catalyst (TTIP:HCl=1:2) has a phase mixture of 68.18% anatase and remaining amorphous TiO_2, while the second one (TTIP:HCl=1:8) consists of a phase mixture of 15% anatase, 66% rutile and remaining amorphous phase. The reduction of catalytic activity might be due to the high rutile concentration in the second sample. Thus, for the decomposition of methylene blue, the anatase phase is a more suitable catalyst than rutile.

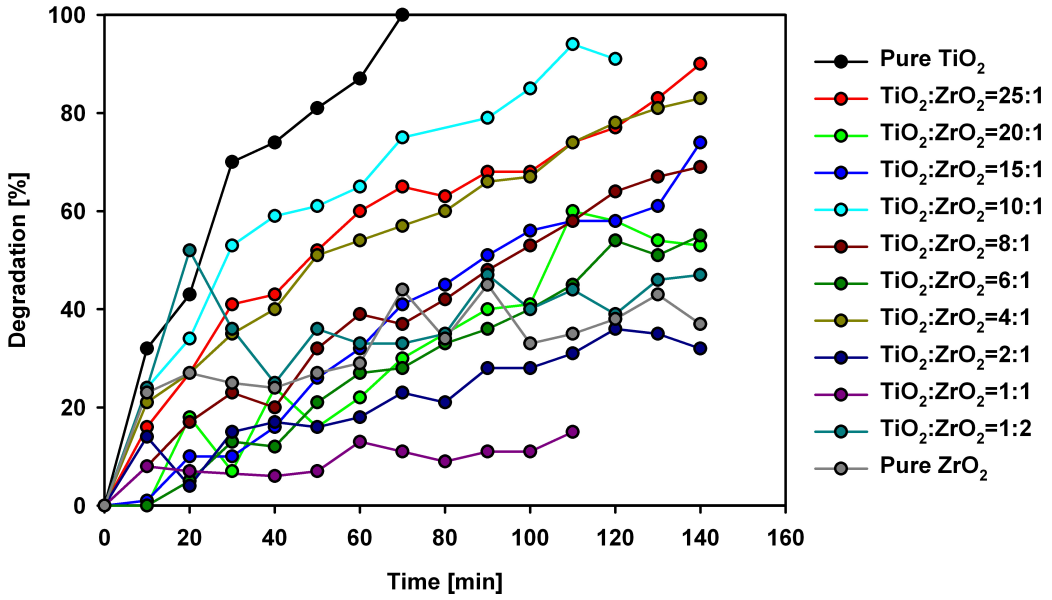

Figure 4.48: Degradation of methylene blue over catalysts with different titania to zirconia ratios. All catalysts were annealed at 500°C for four hours.

The degradation of methylene blue over catalysts with different TiO_2:ZrO_2 ratios is presented in Fig. 4.48. All catalysts were annealed at 500°C for four hours to achieve crystallization. As it shows up, the most active catalyst is that one made of pure titania. Also the other catalysts which have a comparably high activity are those ones which were found to crystallize partially in the anatase structure in section 4.2. The catalysts which present a low activity are those ones which did not undergo the phase transition to the anatase phase. Next to the zirconia concentration of the catalysts and the anatase concentration, other parameters are important, because there is no observable trend depending on the anatase concentration and the amount of added zirconia. None of the structural factors investigated in the former sections is able to explain this observation for the catalytic activity. The agglomeration of the powder particles might be the reason for this observation. Thus, it might be possible that the surface area of the samples plays a crucial role or that the shape of the particles differ and leads to different catalytic activities. In some references in the literature dealing with the surface of TiO_2-ZrO_2 samples, it is often mentioned that samples with equal amounts of titania and zirconia were found to have the highest surface area. This does not fit to the observation presented here, where the sample with TiO_2:ZrO_2=1:1 has the lowest observed activity. Thus, the differences in the catalytic activity might also be due to differences in the particle shape. The pure zirconia catalyst shows a catalytic activity in the middle to the lower field of the materials presented here. This sample crystallized in a mixture of cubic, tetragonal and monoclinic crystalline phase. As already described in the literature [12], titania is thus a much better catalyst than zirconia. To extend the study on the already known dependencies of the catalytic behavior with respect to the titania to zirconia ratio, systematical studies on the influence of the reaction path on the catalytic behavior are presented next.

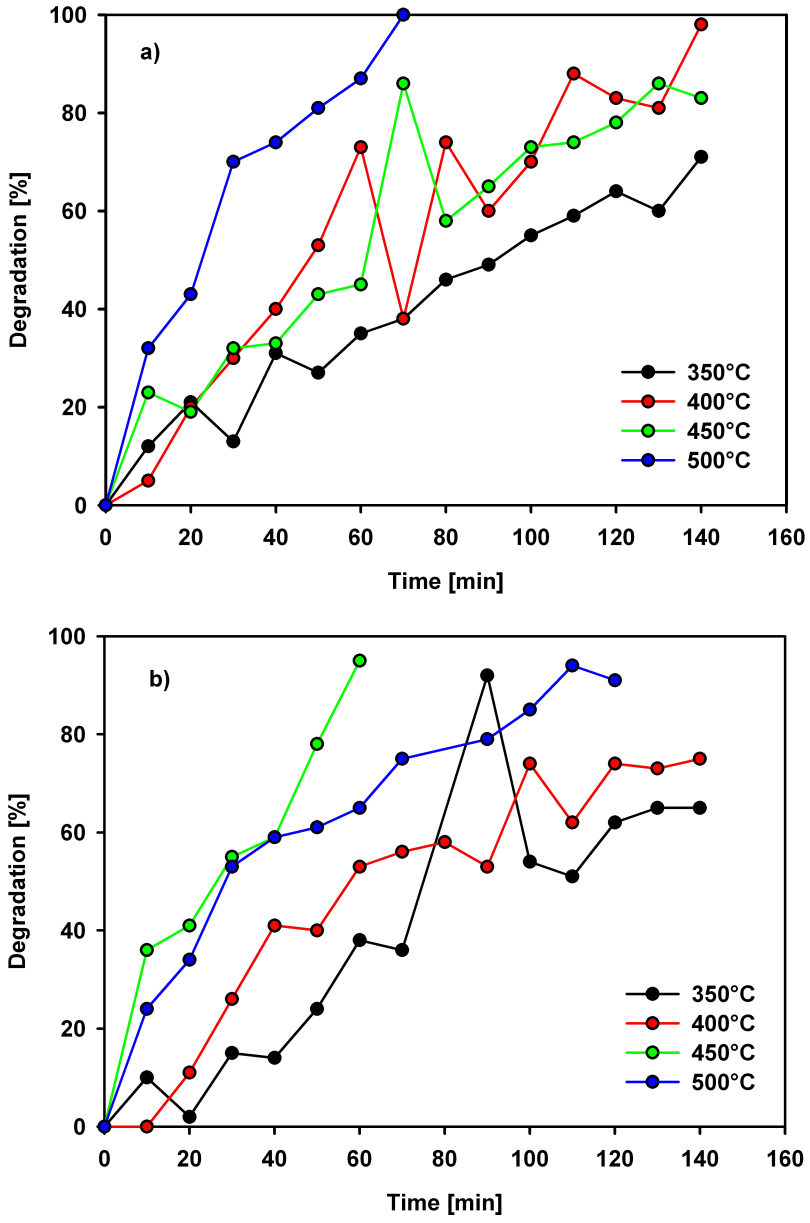

Figure 4.49: Development of the degradation of methylene blue over pure titania (part a) and TiO_2:ZrO_2=10:1 composite (part b) catalysts annealed at different temperatures for four hours.

The dependence of the time dependent methylene blue decomposition over catalysts crystallized at different annealing temperatures is presented in Fig. 4.49 a and b for pure titania and TiO_2:ZrO_2=10:1 catalysts, respectively. For the pure titania catalysts, the powder annealed at 500°C shows the fastest degradation of methylene blue. The lowest activity is observed for the sample annealed at T=350°C and in between these, the catalysts annealed at T=400°C and T=450°C can be found. These two powders do not show significant differences in their catalytic activity. Thus, it can be assumed that the higher degradation rates are due to the higher anatase concentration in the catalyst

material. A detailed view of the catalytic activity in dependence on the crystallinity, the crystallite size and the surface structure sizes will be presented in the next section.

In case of the composite samples, the powders annealed at comparably high annealing temperatures again lead to higher degradation rates. The difference is that the catalyst annealed at T=450°C is more active than that one annealed at T=500°C. In both cases, it can be concluded that the increase in the crystallinity is the reason for the higher catalytic activity.

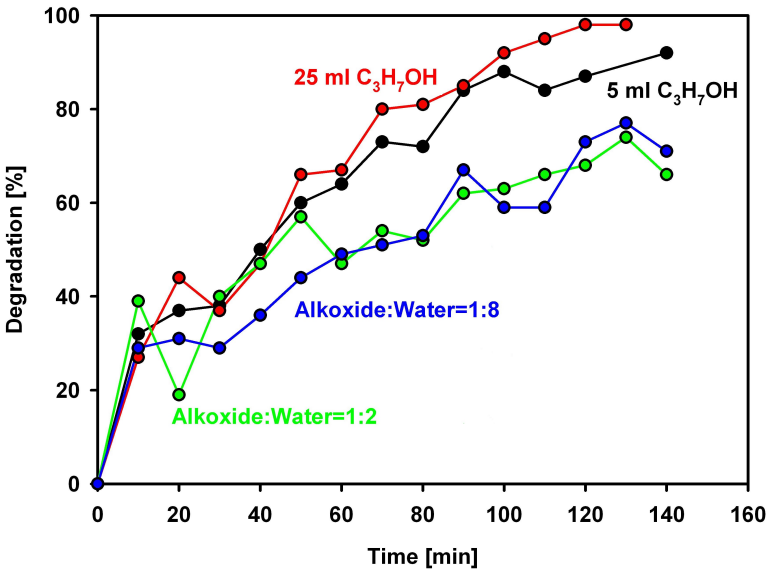

Figure 4.50: Degradation of methylene blue over TiO_2:ZrO_2=20:1 catalysts prepared with different amounts of alcohol and different alkoxide to water ratios. All catalysts were annealed at 500°C for four hours.

Fig. 4.50 presents the catalytic degradation for the TiO_2:ZrO_2=20:1 composite powders prepared with 5 and 25 ml propanol alcohol and those ones prepared with alkoxide to water ratios of 1:2 and 1:8, which were described with respect to their structure in section 4.3.2. As can be observed, the powders prepared under alcohol dilution show a higher catalytic dependency than those ones prepared with different alkoxide to water ratios. It might be assumed that the alcohol dilution during the reaction leads to a weaker degree of agglomeration and thus to a higher surface area. Smaller particles might not only be important for a larger surface area, but also for a better dispersion of the catalyst in the liquid pillar in the cuvette.

4.5.3 Connection between photocatalytic activity and structural parameters

It is known from many works that the photocatalytic efficiency of titania is strongly dependent on the materials structure (see section 2.2.1). In this section, the decomposition times of the methylene blue solutions should be discussed with respect to structural parameters like the anatase concentration of the samples, the crystallite sizes determined by XRD, and the structure size provided by GISAXS measurements.

To have a parameter which can be discussed as a function of crystalline properties, a

half life time for the decomposition is defined by the time after which the intensity of the methylene blue absorption lines is 50 % of the value before the first irradiation period. For this reason, functions for exponential rise to a maximum of the type

$$y = a \cdot \{1 - \exp(-bx)\} \tag{4.2}$$

are fitted to the degradation vs. time data. From the resulting mathematical description of the degradation data, the time when y=50 % is determined and regarded in dependence on the anatase concentration and the crystallite size of the related catalysts.

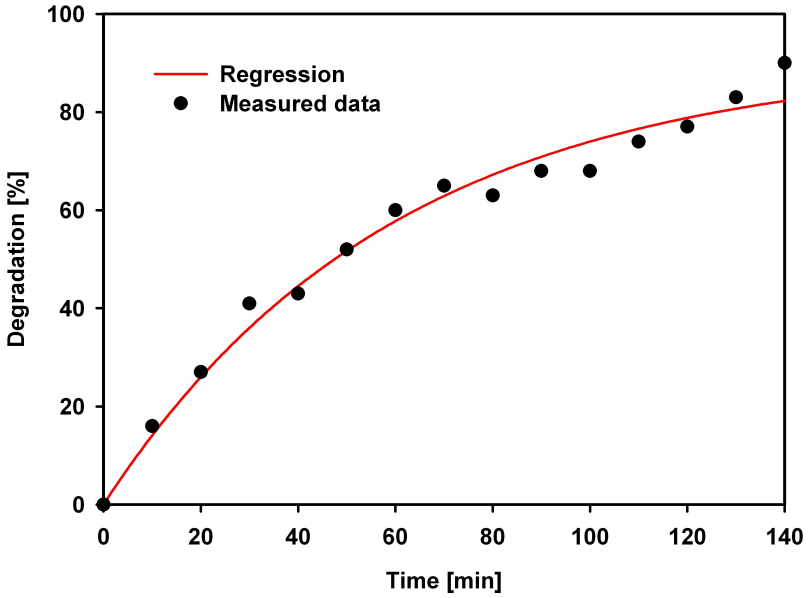

Figure 4.51: Example for the data regression made for the determination of the half life time.

Fig. 4.51 presents an example of such a data regression. As can be seen, the data can be described quite well with the fit, but due to the data range, the maximum value which is reached asymptotically is not 100% but a smaller value, in the presented example about 80%. Nevertheless, the data in the area around 50% degradation is described well by the fit, and the regression is only used to determine the time when 50% of the methylene blue is decomposed. In some cases, for example in the case of the TiO_2:ZrO_2=1:1 catalyst in Fig. 4.48, the maximum is lower than 50%. In these cases, no half life time is determined.

The catalysts ordered with respect to their photocatalytic activity are presented together with the half life times in decreasing activity order with respect to these times in Tab. 4.5.3. There is no tendency obvious with respect to the question if pure titania or composites are the better catalysts. Instead, the preparation history is very important. Catalysts prepared with hydrochloric acid occur in the middle and at the end of the order, and the more acid used, the lower the catalytic activity. The catalyst with the lowest activity was that one which contained large amounts of rutile, which were only able to form due to the acid addition, none of the other samples prepared in this work, prepared without hydrochloric acid, formed this polymorph. It is known from a former work [54], that if much hydrochloric acid is added in the preparation of pure titania, a transparent, strongly viscous gel is formed. Scanning electron microscopy investigations

Catalyst	Half life time [min]
TiO_2:ZrO_2=20:1, 1 M KOH, 500°C	1.15
TiO_2:ZrO_2=20:1, 1 M NaOH, 500°C	3.20
TiO_2, 1 M NaOH, 500°C	9.25
TiO_2, 500°C	20.89
TiO_2:ZrO_2=10:1, 450°C	25.62
TiO_2:ZrO_2=10:1, 500°C	32.87
TiO_2:ZrO_2=20:1, 25 ml C_3H_7OH, 500°C	35.35
TiO_2:ZrO_2=20:1, 5 ml C_3H_7OH, 500°C	36.64
TiO_2:ZrO_2=25:1, 500°C	47.54
TiO_2:ZrO_2=20:1, Alkoxide:water=1:2, 500°C	47.75
TiO_2:ZrO_2=4:1, 500°C	52.45
TiO_2, 450°C	54.28
TiO_2, 400°C	54.70
TiO_2:ZrO_2=20:1, Alkoxide:water=1:8, 500°C	59.38
TiO_2:ZrO_2=20:1, Alkoxide:HCl=1:2, 500°C	63.66
TiO_2:ZrO_2=10:1, 400°C	64.93
TiO_2, 1 M HCl, 500°C	77.08
TiO_2:ZrO_2=10:1, 350°C	83.44
TiO_2:ZrO_2=20:1, 1 M HCl, 500°C	86.68
TiO_2, TTIP:HCl=1:2, 450°C	90.23
TiO_2, 350°C	90.40
TiO_2:ZrO_2=8:1, 500°C	90.90
TiO_2:ZrO_2=15:1, 500°C	96.38
TiO_2:ZrO_2=20:1, 500°C	114.72
TiO_2:ZrO_2=6:1, 500°C	123.06
TiO_2, TTIP:water=1:8, 500°C	137.84
TiO_2, TTIP:HCl=1:8, 450°C	173.14

Table 4.4: Catalysts in order of decreasing activity and the belonging half life times.

of the dried gel showed that it was very dense and did not have the porosity and large surface area of the powder samples.

In the preparation of the samples synthesized in this work, it could be observed that the pure titania samples prepared with a large amount of hydrochloric acid were white and not transparent like gels, but that there was a kind of dense, glass-like film on the sample surface. Thus, there might be a partial gelation on the powder surface, which reduces the surface area and thus the catalytic activity. Thus, the addition of hydrochloric acid in the synthesis step of catalysts for the decomposition of methylene blue should be avoided. It was also found by Houas et al. [138] that the adsorption of methylene blue on the catalyst surface and the degradation of the reagent decreased with decreasing pH value.

In contrast, the addition of bases to the reaction environment in the synthesis step has a strongly enhancing effect on the catalytic activity. Nevertheless, it should be mentioned that there was still a slightly violet color of the methylene blue reaction solution after the irradiation, when it was not longer able to follow the reaction with optical absorption spectroscopy, due to the nearly vanishing absorption peaks. A solution of methylene blue was also prepared without titania catalyst, just with the addition of a drop of 1 M potassium hydroxide solution. No violet color change could be observed and no decomposition occurred after irradiation of the solution. Thus, the effect of the color change and the fast decomposition rates is due to an interplay of the titania, the remaining base contaminations measured with XPS (see section 3.1) and the methylene blue solution.

The half life times were also investigated with respect to a possible dependence on the crystallite size determined from XRD measurements, but no dependence could be observed. The amount of anatase phase seems to be an important factor, which can be seen from the decrease of the catalytic activity with decreasing annealing temperature for the pure TiO_2 catalysts and TiO_2:ZrO_2=10:1 catalysts, investigated after annealing at different annealing temperatures. In section 4.3.2, it was presented that an increase in the annealing temperature leads to an increase in the crystallinity, which means an increase in anatase phase concentration of the presented samples.

It can be seen that the samples prepared with alcohol dilution are better catalysts than those ones prepared with different amounts of added water. This can be due to the higher anatase concentrations observed in the samples prepared with alcohols, which were about 10% larger than those ones observed in the samples prepared with different amounts of water, compare 4.3.2. There was also a change in the crystallite sizes determined from XRD, but due to the fact that the investigated catalysts of pure titania annealed at different temperatures has an increasing activity with increasing annealing temperature although the fast growth of the crystallite size, and that the search for a dependence of the catalytic activity on the crystallite size failed as stated above, it is assumed that the crystallinity has the dominant influence on the catalytic activity with respect to the crystalline parameters.

During the mixture of the methylene blue solution and the powder catalyst, it could be observed in some cases that the solution became slightly opaque due to the dispersion of the catalyst in the reaction medium. This of course leads to a higher surface available for the adsorption of the reactant and the photon absorption during the irradiation. Next to this, reaction can take place everywhere in the liquid pillar and not only in a small layer over the catalyst on the ground of the cuvette. In case of strongly agglomerated powders, where particles are large and heavy, only very small amounts of the powders

were dispersed in the solutions. Light, small agglomerates can disperse in the solutions and in some cases, small amounts of powders were observable on the solution surface. The powders were not mixed during the irradiation and measurement times. For example, in the case of the catalysts prepared with hydrochloric acid, the liquid was still very clear after the mixture with the catalyst powder, maybe because the agglomerates in these powders were larger and thus the powder sank to the ground of the cuvette. Thus, not only the crystallite size and the crystallinity are important, but also the particle size and the agglomeration, of course influencing the surface area, but also influencing the dispersion of the particles in the solution. In industrial applications, the powders would be used bound in coatings, where the dispersion argument would vanish and agglomeration only has an influence on the surface area.

Some of the observed differences in the photocatalytic activity of the prepared powder samples can be explained by the observations made in the structural investigations. Thus, the used investigation methods to determine the structural characteristics can help to understand the activity as a function of the materials structure. Additives can lead to much better catalytic activity, but there is a small uncertainty in this because there is still a slight color of the solution observable with the eye, although there is no significant signal in the absorption spectra which can be fitted with Gauß peaks to determine the degradation. It was observed that rutile is not helpful in the catalyst with respect to the degradation of methylene blue. The addition of zirconia in the materials does not necessarily lead to better catalysts. A better activity with respect to the surface area could not be determined due to the missing of nitrogen sorption isotherms to determine the surface area, but it is possible that the addition of zirconia increases this activity. The preparation history (used additives in the reaction step and annealing treatment) has a very important influence on the activity.

5 Summary and outlook

This work comprised the preparation and characterization of nanostructured pure titania and titania-zirconia composite powders as well as an application study of some of the samples for the photocatalytic decomposition of methylene blue dye. Nanopowders were prepared with sol-gel chemistry, which is a standard tool in chemical preparation of nanostructures. This is the first study which not only investigates TiO_2-ZrO_2 composite powders with systematic changes in the oxide composition ratio, but also with systematic changes in the chemical reaction parameters and compares the results with those ones of pure titania samples. Systematic studies on the influence of the reaction parameters on the structure of sol-gel derived titania samples are already available in the literature and were used for discussion of the experimental results.

The samples were characterized with x-ray absorption fine structure (XAFS), x-ray diffraction (XRD), x-ray photoelectron spectroscopy (XPS), grazing incidence small angle x-ray scattering (GISAXS) and scanning electron microscopy (SEM). The crystallization of titania follows routes very similar to chemical reactions, thus linear combination XANES as a possible tool to follow chemical reactions is used to investigate the phase composition of the powders after annealing at different temperatures. Systematical investigation of the dependence of the crystallinity of titania based nanostructures with respect to the reaction path and annealing temperature with LC-XANES fits are presented here for the first time. The fit of the XANES pre-edge allows for qualitative statements on the first small crystalline clusters built during the chemical reaction. XRD allows for the determination of crystalline phases and the determination of the crystallite size via Scherrer formula. Contaminations in the powders were detected with XPS. The size and size distribution of larger structures was investigated with GISAXS. The presented combination of investigation methods allows the characterization of the prepared samples with respect to nearly all structural characteristics which are important for many applications.

The investigations showed that titania in TiO_2-ZrO_2 composite samples is only able to crystallize at the applied annealing temperatures if the zirconia content of the powders is low enough. The remaining amorphous phase at a certain temperature decreases with increasing titania content of the samples. The addition of zirconia in the composite materials also has a strong influence on the crystallite size. The most important point with respect to the crystallite size is that the size is constant with respect to increasing annealing temperatures or only increase very slightly in the composite samples, while it substantially increases with increasing annealing temperature for the pure titania samples. For some of the composite samples, small amounts of brookite phase were observed, but all other samples, also pure titania sample prepared for comparison to the composites, only showed the anatase phase and remaining amorphous titania. The agglomerated structures become more polydisperse by the addition of zirconia.

An oxide ratio of TiO_2:ZrO_2=20:1 was identified to allow good crystallization as well as crystallite size stabilization. With this ratio, different powders were prepared with different alkoxide:water ratios, different amounts of alcohols added to solute the reac-

tants, different electrolytes and different reaction temperatures. Pure titania samples were prepared for a comparison of the possibility to influence the reaction structure with the synthesis chemistry. The influence of the reaction path on the structure is very small in a certain set of samples prepared with a certain reaction additive. In the studies of the sample set prepared by alcohol addition to the reaction medium, it showed up that the amount of alcohol does not seem to be important for the resulting structure from pure structure investigations. Differences in the powder structure are only observable between certain sample sets prepared with a certain additive. There are differences in the samples prepared with different alkoxide:water ratios and those ones prepared with different degrees of alcohol dilution. In case of the samples prepared with hydrochloric acid, the amount of added electrolyte was found to be very important for the structure of the pure titania powders, but do not have a significant influence on the structure of the composite samples. Thus, the structure of these samples is mainly influenced by the titania to zirconia ratio, while the influence of the chemical reaction path is much smaller. Electrolyte reaction media contaminate the material with their ions, as can be proved by XPS measurements.

The efficiency of the materials in photocatalytic application was studied by investigations of the decomposition of methylene blue with different titania and composite powders. The decomposition was followed by optical absorption spectroscopy. It was found that remaining electrolyte ions from basic solutions used as reaction media in the synthesis step have a strong influence on the photocatalytic reaction. If the catalysts are classified with respect to the half life time of the methylene blue in the solution, the composite and the pure titania samples were strongly mixed with respect to the preparation and the type of the catalyst. Thus, the main impact was not only due to the question if zirconia addition was used or not, but also strongly dependent on the synthesis history.

The assumption that the amount of added water might lead to a stronger influence of the reaction conditions on the materials structure should be tested in the future. Doping with other metal ions can enhance the catalytic activity. The addition of the metal ions might also have an effect on the crystallinity, which should be investigated with XANES. Other factors than crystallinity, crystallite size and crystalline phase seem to have an influence on the catalytic activity, like the particle shape and the surface area. These can be investigated with transmission electron microscopy and the measurement of nitrogen sorption isotherms.

To explain the results of the photocatalysis measurements, it is necessary to regard all aspects like crystallinity, particle size and contaminations, which were investigated with the used analysis methods. Thus, a detailed analysis of the prepared catalysts with the presented methods is necessary to understand the impact on catalysis reactions. Due to the dependence of other applications on structural properties, compare for example section 2.2.2, the characterization of materials with these methods can also help gain further understanding in these cases. Also a detailed look on the preparation history is necessary. This was already done in the literature in the case of pure titania, but much less systematic information of the dependence of the composite structures on the preparation path is available in the literature.

Acknowledgements

I would like to thank Prof. Dr. R. Frahm for the possibility to make the presented studies in his group and for the helpful discussions.

The work was continuously attended by Dr. Dirk Lützenkirchen-Hecht. I thank him for many discussions and helpful ideas.

My thanks also extend to Prof. Dr. M. Tolan who was the second referee of this work.

The investigations presented in this work often required technical help, especially those ones made at synchrotron radiation facilities. My thanks go to all group members, who accompanied this work with help in office and laboratory and by many discussions and of course also with many funny moments. Daniel Krämer, Benjamin Bornmann, Jan Gasse, Ralph Wagner, Oliver Müller, Justus Just, Pascal Becker, Oliver von Pohlheim and Stefan Balk gave indispensable help and created a good human climate in the group.

The XAS and GISAXS measurements were performed at DELTA (TU Dortmund) and HASYLAB (DESY, Hamburg). I would like to thank the staffs of these two facilities for providing the beamtime and the beam. Special thanks go to the beamline scientist who supported this work with technical help. These were Ralph Wagner and Stefan Balk (DELTA) and Edmund Welter, Roman Chernikov and Jan Perlich. Jan Perlich also supported the work with help in the GISAXS measurements and data analysis, which was very important due to the difficulties in context with this measurement technique, which was an uncharted water for me.

I would like to thank my partner Christian Müller for being at my side, listening and helping with software problems.

This work was financially supported by the "NRW Forschungsschule Forschung mit Synchrotronstrahlung in den Nano- und Biowissenschaften".

Last but not least, my thanks go to my friends. They helped me during my work with their humor, with listening to my problems and cheering me up in difficult times.

Bibliography

[1] S. H. Elder, Y. Gao, X. Li, J. Liu, D. E. McCready, and Jr. C. F. Windisch. *Chem. Mater.*, **10**: 3140–3145, (1998).

[2] R. Rossmanith, C. K. Weiss, J. Geserick, N. Hüsing, U. Hörmann, U. Kaiser, and K. Landfester. *Chem. Mater.*, **20**: 5768–5780, (2008).

[3] L. Cademartiri and A. Ozin. *An Introduction to nanochemistry concepts.* Wiley-VHC, Weinheim, (2009).

[4] N. Serpone, D. Lawless, R. Khairutdinov, and E. Pelizzetti. *J. Phys. Chem.*, **99**: 16655–16661, (1995).

[5] U. Hartmann. *Nanostrukturforschung und Nanotechnologie-Band 1: Grundlagen.* Oldenbourg Verlag, München, (2012).

[6] A. G. Agrios and P. Pichat. *J. Appl. Electrochem.*, **35**: 655–663, (2005).

[7] A. Mills, R. H. Davies, and D. Worsley. *Chem. Soc. Rev.*, **22**: 417–425, (1993).

[8] S.-J. Kim, E. G. Lee, S. D. Park, C. J. Jeon, Y. H. Cho, C. K. Rhee, and W. W. Kim. *J. Sol-Gel Sci. Technol.*, **22**: 63–74, (2001).

[9] L. X. Chen, T. Rajh, Z. Wang, and M. C. Thurnauer. *J. Phys. Chem. B*, **101**: 10688–10697, (1997).

[10] Y. Li, T. J. White, and S. H. Lim. *J. Solid State Chem.*, **177**: 1372–1381, (2004).

[11] K. L. Yeung, A. J. Maira, J. Stolz, E. Hung, N. Ka-Chun Ho, A. C. Wei, J. Soria, K. J. Chao, and P. L. Yue. *J. Phys. Chem. B*, **106**: 4608–4616, (2002).

[12] J. A. Navio, G. Colón, and J. M. Herrmann. *J. Photochem. Photobiol. A: Chem.*, **108**: 179–185, (1997).

[13] R. Schiller, C. K. Weiss, and K. Landfester. *Nanotechnology*, **21**: 405603–405613, (2010).

[14] S. Ito, S. Inoue, H. Kawada, M. Hara, M. Iwasaki, and H. Tada. *J. Colloid Interf. Sci.*, **216**: 59–64, (1999).

[15] D. T. Tompkins, W. A. Zeltner, B. J. Lawnicki, and M. A. Anderson. *American Society of Heating and Air-conditioning Engineers (ASHRAE) Trans.*, **111**: 60–84, (2005).

[16] T. Rajh, A. E. Ostafin, O. I. Micic, D. M. Tiede, and M. C. Thurnauer. *J. Phys. Chem.*, **100**: 4538–4545, (1996).

[17] S. Sakulkhaemaruethai, A. Kitiyanan, and S. Yoshikawa. *J. Ceram. Proc. Res.*, **7**: 10–13, (2006).

[18] X.-P. Wang, Y. Yu, X.-F. Hu, and L. Gao. *Thin Solid Films*, **371**: 148–152, (2000).

[19] Z. Zhang, C.-C. Wang, R. Zakaria, and J. Y. Ying. *J. Phys. Chem. B*, **102**: 10871–10878, (1998).

[20] V. Luca, S. Djajanti, and R. F. Howe. *J. Phys. Chem. B*, **102**: 10650–10657, (1998).

[21] X. Z. Ding and X. H. Liu. *Mater. Sci. Eng.*, **A224**: 210–215, (1997).

[22] B. Ohtani, J. Handa, S. Nishimoto, and T. Kagiya. *Chem. Phys. Lett.*, **120**: 292–294, (1985).

[23] H. Zhang and J. Banfield. *J. Phys. Chem. B*, **104**: 3481–3487, (2000).

[24] H. Kominami, J. Kato, S. Murakami, Y. Kera, M. Inoue, T. Inui, and B. Ohtani. *J. Mol. Catal. A: Chem.*, **144**: 165–171, (1999).

[25] S. Isley and R. L. Penn. *J. Phys. Chem. B*, **110**: 15134–15139, (2006).

[26] K. Mogyorósi, É. Karácsonyi, Zs. Cegléd, A. Dombi, V. Danciu, L. Baia, and Zs. Pap. *J. Sol-Gel Sci. Technol.*, **65**: 277–282, (2013).

[27] Y. Zhang, G. Xiong, N. Yao, W. Yang, and X. Fu. *Catal. Today*, **68**: 89–95, (2001).

[28] S. K. Poznyak, D. V. Talapin, and A. I. Kulak. *J. Phys. Chem. B*, **105**: 4816–4823, (2001).

[29] J. Fung and I. Wang. *Appl. Catal. A: General*, **166**: 327–334, (1998).

[30] D. G. Shchukin and R. A. Caruso. *Adv. Funct. Mater.*, **13**: 789–794, (2003).

[31] P. G. Bruce, B. Scrosati, and J.-M. Tarascon. *Angew. Chem. Int. Ed.*, **47**: 2930–2946, (2008).

[32] V. Luca, T. L. Hanley, N. K. Roberts, and R. F. Howe. *Chem. Mater.*, **11**: 2089–2102, (1999).

[33] G. Nuspl, K. Yoshizawa, and T. Yamabe. *J. Mater. Chem.*, **7**: 2529–2536, (1997).

[34] G. J. Wilson, G. D. Will, R. L. Frost, and S. A. Montgomery. *J. Mater. Chem.*, **12**: 1787–1791, (2002).

[35] M. Wagemaker, W. J. H. Borghols, and F. M. Mulder. *J. Am. Chem. Soc.*, **129**: 4323–4327, (2007).

[36] M. Grätzel. *Inorg. Chem.*, **44**: 6841–6851, (2005).

[37] V. Vishwanathan, H.-S. Roh, J.-W. Kim, and K.-W. Jun. *Catal. Lett.*, **96**: 23–28, (2004).

[38] M. Momirlan and T. N. Veziroglu. *Renewable and Sustainable Energy Reviews*, **6**: 141–179, (2002).

[39] H.-M. Lin, C.-H. Keng, and C.-Y. Tung. *Nanostruct. Mater.*, **9**: 747–750, (1997).

[40] J. Arbiol, J. Cerdà, G. Dezanneau, A. Cirera, F. Peiró, A. Cornet, and J. R. Morante. *J. Appl. Phys.*, **92**: 853–861, (2002).

[41] B. Grzmil, M. Glen, B. Kic, and K. Lubkowski. *Ind. Eng. Chem. Res.*, **50**: 6535–6542, (2011).

[42] M. Gopal, W. J. Moberly Chan, and L. C. DeLonghe. *J. Mater. Sci.*, **32**: 6001–6008, (1997).

[43] E. L. Prociow, K. Sierazka, J. Domaradzki, D. Kaczmarek, and M. Mazur. *Acta Phys. Pol. A*, **116**: 72–74, (2009).

[44] C. J. Brinker and G. W. Scherer. *Sol-Gel Science: The Physics and Chemistry of Sol-Gel Processing*. Academic Press, San Diego, (1990).

[45] B. Ohtani, Y. Ogawa, and S. Nishimoto. *J. Phys. Chem. B*, **101**: 3746–3752, (1997).

[46] K. C. Song and S. E. Paratsinis. *J. Colloid Interface Sci.*, **231**: 289–298, (2000).

[47] C. C. Wang and J. Y. Ying. *Chem. Mater.*, **11**: 3113–3120, (1999).

[48] Y. Dimitriev and Y. Ivanova. *J. of the University of Chem. Technol. and Metallurgy*, **43**: 181–192, (2008).

[49] L. Hu, T. Yoko, H. Kozuka, and S. Sakka. *Thin Solid Films*, **219**: 18–23, (1992).

[50] A. Soloviev, R. Tufeu, C. Sanchez, and A. V. Kanaev. *J. Phys. Chem. B*, **105**: 4175–4180, (2001).

[51] K. C. Song and S. E. Paratsinis. *J. Colloid Interface Sci.*, **231**: 289–298, (2000).

[52] A. Rammal, F. Brisach, and M. Henry. *Comptes Rendus Chimie*, **5**: 59–66, (2002).

[53] J. Yang, S. Mei, and J. M. F. Ferreira. *J. Am. Ceram. Soc.*, **83**: 1361–1368, (2000).

[54] S. J. Pfleiderer. Preparation of oxide nanoparticles by hydroysis. Diplomarbeit, Bergische Universität Wuppertal, Wuppertal, (2009).

[55] J. Livage. *Catal. Today*, **41**: 3–19, (1998).

[56] Y. Li, T. White, and S. H. Lim. *Rev. Adv. Mater.*, **5**: 211–215, (2003).

[57] J. Livage, C. Sanchez, M. Henry, and S. Doeuff. *Solid State Ionics*, **32/33**: 633–638, (1989).

[58] R. L. Penn and J. Banfield. *Geochim. Cosmochim. Acta*, **63**: 1549–1557, (1999).

[59] B. M. Reddy and A. Khan. *Catalysis Reviews*, **47**: 257–296, (2005).

[60] K. Maver, U. Lavrencic Stangar, U. Cernigoj, S. Gross, and R. Cerc Korosec. *Photochem. Photobiol. Sci.*, **8**: 657–662, (2009).

[61] D. Lützenkirchen-Hecht and H.-H. Streblow. *Synchrotron methods for corrosion research. In: Analytical Methods in Corrosion Science and Engineering.* Taylor & Francis (CRC Press), Boca Raton, (2006).

[62] W. D. Kingery, H. K. Bowen, and D. R. Uhlmann. *Introduction to Ceramics.* John Wiley&Sons, New York, (1976).

[63] H. Ibach and H. Lüth. *Festkörperphysik.* Springer, Berlin, Heidelberg, (2002).

[64] E. S. Holbig. *The effect of Zr-Doping and Crystallite Size on the Mechanical Properties of TiO_2 Rutile and Anatase.* PhD thesis, Universität Bayreuth, Bayreuth, (2008).

[65] L. X. Chen, T. Rajh, W. Jäger, J. Nedeljkovic, and M. C. Thurnauer. *J. Synchrotron Rad.*, **6**: 445–447, (1999).

[66] http://www.mineralienatlas.de/lexikon/.

[67] H. Zhang and J. F. Banfield. *Chem. Mater.*, **14**: 4145–4154, (2002).

[68] B. L. Bischoff and M. A. Anderson. *Chem. Mater.*, **7**: 1772–1778, (1995).

[69] S. Mahshid, M. Askari, and M. Sasani Ghamsari. *J. Mater. Proc. Technol.*, **189**: 296–300, (2007).

[70] K. Terabe, K. Kato, H. Miyazaki, S. Yamaguchi, A. Imai, and Y. Iguchi. *J. Mater. Sci.*, **29**: 1617–1622, (1994).

[71] J. G. Choi and K. Y. Park. *J. Nanopart. Res.*, **8**: 269–278, (2006).

[72] R. L. Penn and J. F. Banfield. *Am. Mineral.*, **83**: 1077–1082, (1998).

[73] P. I. Gouma, P.K. Dutta, and M. J. Mills. *Nanostruct. Mater.*, **11**: 1231–1237, (1999).

[74] H. Zhang and J. F. Banfield. *J. Mater. Res.*, **15**: 437–448, (2000).

[75] P. W. Voorhees. *Annu. Rev. Mater. Sci.*, **22**: 197–215, (1992).

[76] M. R. Ranade, S. H. Elder, and A. Navrotsky. *Chem. Mater.*, **14**: 1107–1114, (2002).

[77] B. M. Reddy and A. Kahn. *Catalysis Reviews*, **47**: 257–296, (2005).

[78] Q. Xu and M. A. Anderson. *J. Am. Ceram. Soc.*, **76**: 2093–2097, (1993).

[79] J. A. Navio, F. J. Marchena, M. Macias, P. J. Sanchez-Soto, and P. Pichat. *J. Mater. Sci.*, **27**: 2463–2467, (1992).

[80] A. S. Banard, R. R. Yeredla, and H. Xu. *Nanotechnology*, **17**: 3039–3047, (2006).

[81] D. Nikolay. *Herstellung und Untersuchung von ZTA-Nanocompositkeramiken.* PhD thesis, Rheinische Friederich-Wilhelms Universität Bonn, Bonn, (2010).

[82] G. Bunker. *Introduction to XAFS.* Cambridge University Press, Cambridge, (2010).

[83] J. J. Rehr and R. C. Albers. *Rev. Mod. Phys.*, **72**: 621–654, (2000).

[84] J. G. Parsons, K. Dokken, J. R. Peralta-Videa, J. Romero-Gonzalez, and J. L. Gardea-Torresdey. *Appl. Spectrosc.*, **61**: 338–345, (2007).

[85] E. R. Malinowski. *Factor analysis in chemistry.* John Wiley and Sons, New York, (2002).

[86] J. Stötzel, D. Lützenkirchen-Hecht, R. Frahm, C. V. Santilli, S. H. Pulcinelli, R. Kaminski, E. Fonda, F. Villain, and V. Briois. *J. Phys. Chem. C*, **114**: 6228–6236, (2010).

[87] J. C. Parlebas, M. A. Khan, T. Uozumi, K. Okada, and A. Kotani. *J. Electron. Spectrosc. Relat. Phenom.*, **71**: 117–139, (1995).

[88] N. Jiang, D. Su, and J. C. H. Spence. *Phys. Rev. B*, **76**: 214117 1–9, (2007).

[89] Z. Y. Wu, G. Ouvrard, P. Gressier, and C. R. Natoli. *Phys. Rev. B*, **55**: 10382–10391, (1997).

[90] L. A. Grunes. *Phys. Rev. B*, **27**: 2111–2131, (1983).

[91] P. C. Angelome, L. Andrini, M. E. Calvo, F. G. Requejo, S. A. Bilmes, and G. J. A. A. Soler-Illia. *J. Phys. Chem. C*, **111**: 10886–10893, (2007).

[92] K. L. Yeung, A. J. Maira, J. Stolz, E. Hung, N. Ka-Chun Ho, A. C. Wei, J. Soria, K. J. Chao, and P. L. Yue. *J. Phys. Chem. B*, **106**: 4608–4616, (2002).

[93] F. Farges, G. E. Brown, and J. J. Rehr. *Geochim. Cosmochim. Acta*, **60**: 3023–3038, (1996).

[94] H. Zhang, B. Chen, J. F. Banfield, and G. A. Waychunas. *Phys. Rev. B*, **78**: 214106 1–12, (2008).

[95] B. E. Warren. *X-ray diffraction.* Dover Publications, New York, (1990).

[96] W. Kraus and G. Nolze. *J. Appl. Cryst.*, **29**: 301–303, (1996).

[97] J. I. Langford, D. Louër, and P. Scardi. *J. Appl. Cryst.*, **33**: 964–974, (2000).

[98] A. A. Gribb and J. F. Banfield. *Am. Mineral.*, 82:717–728, 1997.

[99] http://staff.chess.cornell.edu/ smilgies/gisaxs/GISAXS.php.

[100] P. Müller-Buschbaum. *Lect. Notes Phys.*, **776**: 61–89, (2009).

[101] P. Müller-Buschbaum, E. Bauer, E. Maurer, S. V. Roth, R. Gehrke, M. Burghammer, and C. Riekel. *J. Appl. Cryst.*, **40**: 341–345, (2007).

[102] J. Als-Nielsen and D. McMorrow. *Elements of Modern X-ray Physics.* John Wiley and Sons, New York, 2nd edition, (2011).

[103] J. R. Levine, J. B. Cohen, Y. W. Chung, and P. Georgopoulos. *J. Appl. Cryst.*, **22**: 528–532, (1989).

[104] J. Perlich, J. Rubeck, S. Botta, R. Gehrke, S. V. Roth, M. A. Ruderer, S. M. Prams, M. Rawolle, Q. Zhong, V. Körstgens, and P. Müller-Buschbaum. *Rev. Sci. Instrum.*, **81**: 105105, (2010).

[105] P. Müller-Buschbaum. *Anal. Bioanal. Chem.*, **376**: 3–10, (2003).

[106] P. Willmott. *Introduction to Synchrotron Radiation.* John Wiley and Sons, West Sussex, (2011).

[107] https://dpdak.desy.de/index.php/Hauptseite.

[108] H.-H. Perkampus. *UV-Vis Spektroskopie und ihre Anwendungen*, volume 21. Springer-Verlag, Berlin, (1986).

[109] J. F. Watts. *X-ray photoelectron spectroscopy. In:Surface science techniques.* Pergamon, Oxford, (1994).

[110] H. J. Butt, K. Graf, and M. Kappl. *Physics and chemistry of interfaces*, volume 2. Wiley-VHC, Weinheim, (2006).

[111] J. H. Scofield. *J. Electron. Spectrosc. Relat. Phenom.*, **8**: 129–137, (1976).

[112] C. Linsmeier. *Auger electron spectroscopy. In: Surface Science Techniques.* Pergamon, Oxford, (1994).

[113] D. Briggs. *X-ray photoelectron spectroscopy as an analytical technique. In: Handbook of x-ray and ultraviolet photoelectron spectroscopy.* Heyden & Son, London, (1977).

[114] S. L. Flegler, J. W. Heckman, and K. L. Klomparens. *Elektronenmikroskopie.* Spektrum Akademischer Verlag, Heidelberg, (1995).

[115] K. Wille. *Physik der Teilchenbeschleuniger und Synchrotronstrahlungsquellen.* B. G. Teubner, Stuttgart, (1996).

[116] http://www.delta.tu dortmund.de.

[117] http://hasylab.desy.de/facilities.

[118] O. Kaul. *Synchrotronstrahlung: Erzeugung, Eigenschaften und Instrumentierung. In: Forschung mit Synchrotronstrahlung.* Vieweg+Teubner, Wiesbaden, (2010).

[119] K. Rickers, W. Drube, H. Schulte-Schrepping, E. Welter, U. Brüggmann, M. Herrmann, J. Heuer, and H. Schulz-Ritter. *AIP Conf. Proc.*, **882**: 905–907, (2007).

[120] D. Lützenkirchen-Hecht, R. Wagner, U. Haake, A. Watenphul, and R. Frahm. *J. Synchrotron Rad.*, **16**: 264, (2009).

[121] T. Ressler. *J. Synchrotron Rad.*, **5**: 118–122, (1998).

[122] J. A. Victoreen. *J. Appl. Phys.*, **19**: 855–860, (1948).

[123] M. Newville. *J. Synchrotron Rad.*, **8**: 96–100, (2001).

[124] M. Wojdyr. *J. Appl. Crys.*, **43**: 1126–1128, (2010).

[125] N. Thammajak. SAXS and GISAXS Techniques at beamline BW4: Beamline Set up, Measurement and Analysis of Colloidal Crystals, DESY Summer Student Program, DESY, Hamburg, (2007).

[126] S. V. Roth, R. Döhrmann, M. Dommach, M. Kuhlmann, I. Kröger, R. Gehrke, H. Walter, C. Schroer, B. Lengeler, and P. Müller-Buschbaum. *Rev. Sci. Instrum.*, **77**: 085106 1–8, (2006).

[127] http://www.oceanoptics.eu/html/index.php.

[128] J. Yao and C. Wang. *International Journal of Photoenergy*, **2010**: 1–6, (2010).

[129] J. A. Navio, F. J. Marchena, M. Macias, P. J. Sanchez-Soto, and P. Pichat. *J. Mater. Sci.*, **27**: 2463–2467, (1992).

[130] R. W. G. Wyckhoff. *Crystal Structures*, volume 1. Robert E. Krieger Publishing, Malabar, 2nd edition, 1963.

[131] X. Wu, Z. Chen, G. Qing (Max) Lu, and L. Wang. *Adv. Funct. Mater.*, **20**: 1–6, (2011).

[132] R. D. Shannon and J. A. Pask. *J. Am. Ceram. Soc.*, **48**: 391–398, (1965).

[133] S. J. Pfleiderer, D. Lützenkirchen-Hecht, and R. Frahm. *J. Sol-Gel Sci. Technol.*, **64**: 27–35, (2012).

[134] B. Pattier, M. Henderson, G. Brotons, and A. Gibaud. *J. Phys. Chem. B*, **114**: 5227–5232, (2010).

[135] K.-N. Kumar, J. Kumar, and K. Keizer. *J. Am. Ceram. Soc.*, **77**: 1396–1400, (1994).

[136] http://www.chemikalienlexikon.de/cheminfo/0379 lex.htm.

[137] C. E. Mortimer. *Chemie*, volume 10. Thieme Verlag, Stuttgart, (2010).

[138] A. Houas, H. Lachheb, M. Ksibi, E. Elaloui, C. Guillard, and J.-M. Herrmann. *Appl. Catal. B: Environmental*, **31**: 145–157, (2001).